SIRIUS-M: A Symmetric-Illumination, Inertially Confined Direct Drive Materials Test Facility

B. Badger, S.I. Abdel-Khalik, H. Attaya, R.L. Engelstad, G.L. Kulcinski, J.H. Liang, E.G. Lovell, G.A. Moses, R.R. Peterson, M.E. Sawan, I.N. Sviatoslavsky, L. Wittenberg, S. Skupsky, R. McCrory, P. McKenty, C. Verdon, A.J. Schmitt, R.H. Lehmberg, J.H. Gardner, S.E. Bodner

September 30, 1985

UWFDM-651

FUSION TECHNOLOGY INSTITUTE

UNIVERSITY OF WISCONSIN

MADISON WISCONSIN

SIRIUS-M: A Symmetric-Illumination, Inertially Confined Direct Drive Materials Test Facility

B. Badger, S.I. Abdel-Khalik, H. Attaya, R.L. Engelstad, G.L. Kulcinski, J.H. Liang, E.G. Lovell, G.A. Moses, R.R. Peterson, M.E. Sawan, I.N. Sviatoslavsky, L. Wittenberg, S. Skupsky, R. McCrory, P. McKenty, C. Verdon (University of Rochester), A.J. Schmitt, R.H. Lehmberg, J.H. Gardner, S.E. Bodner (Naval Research Laboratory)

Fusion Technology Institute
University of Wisconsin
1500 Engineering Drive
Madison, WI 53706

http://fti.neep.wisc.edu

September 30, 1985

UWFDM-651

SIRIUS-M: A SYMMETRIC-ILLUMINATION, INERTIALLY CONFINED DIRECT DRIVE MATERIALS TEST FACILITY

B. Badger, S.I. Abdel-Khalik, H. Attaya, R.L. Engelstad, G.L. Kulcinski, J.H. Liang, E.G. Lovell, G.A. Moses, R.R. Peterson, M.E. Sawan, I.N. Sviatoslavsky, L. Wittenberg

Fusion Technology Institute, 1500 Johnson Drive
University of Wisconsin-Madison, Madison, Wisconsin 53706

Stan Skupsky, Robert McCrory, Pat McKenty, Charles Verdon

Laboratory for Laser Energetics
University of Rochester, Rochester, NY 14627

A.J. Schmitt, R.H. Lehmberg, J.H. Gardner, S.E. Bodner

Naval Research Laboratory
4555 Overlook Avenue, S.W., Washington, D.C. 20375

September 30, 1985

UWFDM-651

TABLE OF CONTENTS

EXECUTIVE SUMMARY

The Fusion Technology Institute of the University of Wisconsin (FTI) and the University of Rochester's Laboratory for Laser Energetics (LLE), in cooperation with the Naval Research Laboratory (NRL), have conducted a study of the critical issues related to the design of an ICF materials test facility, SIRIUS-M. This report summarizes the results obtained by the FTI and LLE team related to the SIRIUS-M design during 1985.

The SIRIUS-M facility is designed to duplicate the time-dependent radiation damage structure unique to ICF systems in order to provide the technology base necessary for an ICF demonstration facility. While it is commonly assumed by the ICF community that the MCF materials program will provide the data needed for designing ICF reactors, the large differences between the damage conditions in ICF and MCF environments illustrated in Fig. ES.1 make it imperative to develop a dedicated ICF materials test facility such as SIRIUS-M.

The SIRIUS-M test facility uses symmetrically-illuminated targets. Critical issues unique to symmetrically-illuminated direct-drive ICF reactors were previously examined by the FTI and LLE team in a preliminary conceptual reactor design, SIRIUS.[1] Several features of the reactor design were studied in some detail including: target performance, first wall thermal response, reflector performance, mechanical design, and radiation damage to both the structure and final optics. The SIRIUS-M study described in this report builds on the knowledge gained in these areas.

In selecting the technical specifications and design parameters for the SIRIUS-M facility, we have attempted to limit the initial capital and operat-

ing costs by limiting the "mission" of the facility to only materials testing; tritium breeding and high-temperature recovery of thermonuclear energy are not included. The "desired" neutron wall loading has been set at $\gtrsim$ 2 MW/m^2; this corresponds to an irradiation of ~ 1 MW-yr/m^2 per calendar year of operation so that the necessary cumulative damage can be achieved in a few years of operation.

Table ES.1 lists the main design parameters for the SIRIUS-M facility. Attention has been focused on several areas unique to an ICF materials test facility including: test module design and damage rate estimation; cavity design and first wall protection; target design; and placement of the final mirror. The target and driver design requirements for SIRIUS-M have been relaxed from the SIRIUS reactor values. A 1 MJ KrF laser energy (versus 2.1 MJ) and a single-shell target with a low gain of 13.4 (versus 64) have been used.

In order to achieve a neutron wall loading of 2 MW/m^2 at a reasonable repetition rate (10 Hz) and target yield (13.4 MJ), it is necessary to protect the first wall by placing 1 torr of xenon in the cavity. Gas protection is based on the principle that the soft x-rays and ionic debris produced by the explosions will be stopped in the gas which reradiates that energy to the wall over a relatively "long" period of time (~ 10^{-4} s) and thus limit the wall surface temperature rise and evaporation. Actively-cooled, graphite-faced tiles are used to cover the SIRIUS-M cavity as shown in Figs. ES.2 and ES.3. Analysis of unprotected dry graphite walls has shown that the maximum wall loading corresponding to an evaporation limit of 1 mm/yr is ~ 0.75 MW/m^2; an even lower wall loading of ~ 0.3 MW/m^2 is necessary to keep the maximum thermal stress at the surface from exceeding the compressive strength of the

Table ES.1. Design Parameters for SIRIUS-M

	Value	Unit
Fusion power	134	MW
Tritium consumption rate	3.4	kg/CY
Target yield	13.4	MJ
Target gain	13.4	---
Repetition rate	10	Hz
Laser energy (KrF)	1	MJ
Number of laser beams	32	---
Neutron wall loading	2	MW/m^2
Chamber inner radius	2	m
Cavity gas	xenon	---
Gas pressure	1	torr
Xenon inventory	800	liters (STP)
Number of tiles	20	---
Tile area	2.5	m^2/tile
Face material	graphite	---
Tile thickness	1.0	cm
Back material	HT-9	---
Coolant	water	---
Module diameter	1.14	m
Module depth	0.2	m
Capsule diameter	5	cm
Capsule length	20	cm
Capsule volume	0.39	liters
Number of capsules	434	---
Active test volume	171	liters
Maximum dpa/FPY (Fe)	24	dpa/FPY
Maximum appm He/FPY (Fe)	145	appm/FPY

graphite (see Fig. ES.4). The use of gas protection in SIRIUS-M with a wall loading of 2 MW/m^2 results in negligible surface evaporation and acceptable maximum thermal stress (~ 60 MPa).

Two circular test modules are used in SIRIUS-M. Each module has a front surface area of 1 m^2 and fits between three beam ports. No significant radial and azimuthal damage variation in the module results from these penetrations. The peak dpa rate is 24 dpa/FPY yielding a peak accumulated damage of 120 dpa at the end of life of the SIRIUS-M facility. A total volume integrated damage figure of merit of 2,840 dpa-ℓ per full power year can be achieved in SIRIUS-M; considerably lower values are expected in other test facilities as shown in Table ES.2.

The work performed so far has shown that an ICF materials test facility, such as SIRIUS-M, which uses symmetrically-illuminated targets can provide the necessary critical data and technology base for an ICF demonstration facility. However, several critical issues remain to be solved before a complete, self-

Table ES.2. Dpa-ℓ Values per FPY of Operating in Different Facilities

Neutron Production Mode	Device	
Accelerator	RTNS-II	0.0003
Accelerator	FMIT	5
Tokamak-Magnetic	INTOR	182
Mirror-Magnetic	TASKA-M	530
Mirror-Magnetic	TASKA	1510
Laser-Inertial	SIRIUS-M	2840

consistent design can be initiated. These include: laser driver design; costing estimate; materials testing schedule; development of a reflector module to address problems unique to ICF systems; stress analysis; cavity design optimization; shield design; radioactivity; and two-dimensional target design calculations. Some of these issues will be addressed in the upcoming year.

References for Executive Summary

1. B. Badger et al., "Preliminary Conceptual Design of SIRIUS, A Symmetric Illumination, Direct Drive Laser Fusion Reactor," University of Wisconsin Fusion Technology Institute Report UWFDM-568 (March 1984).

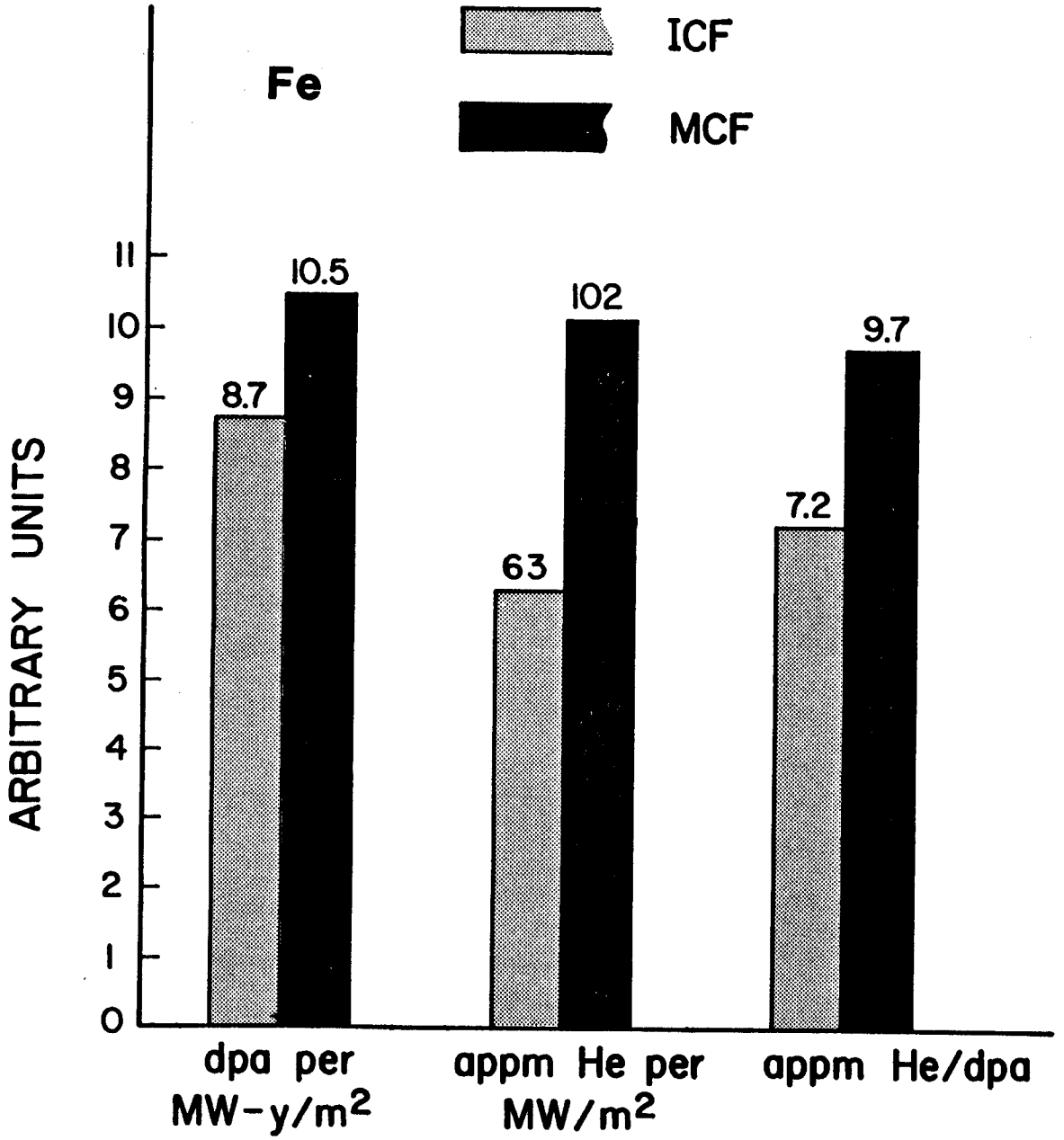

Fig. ES.1. Comparison between damage rates in ICF and MCF reactors.

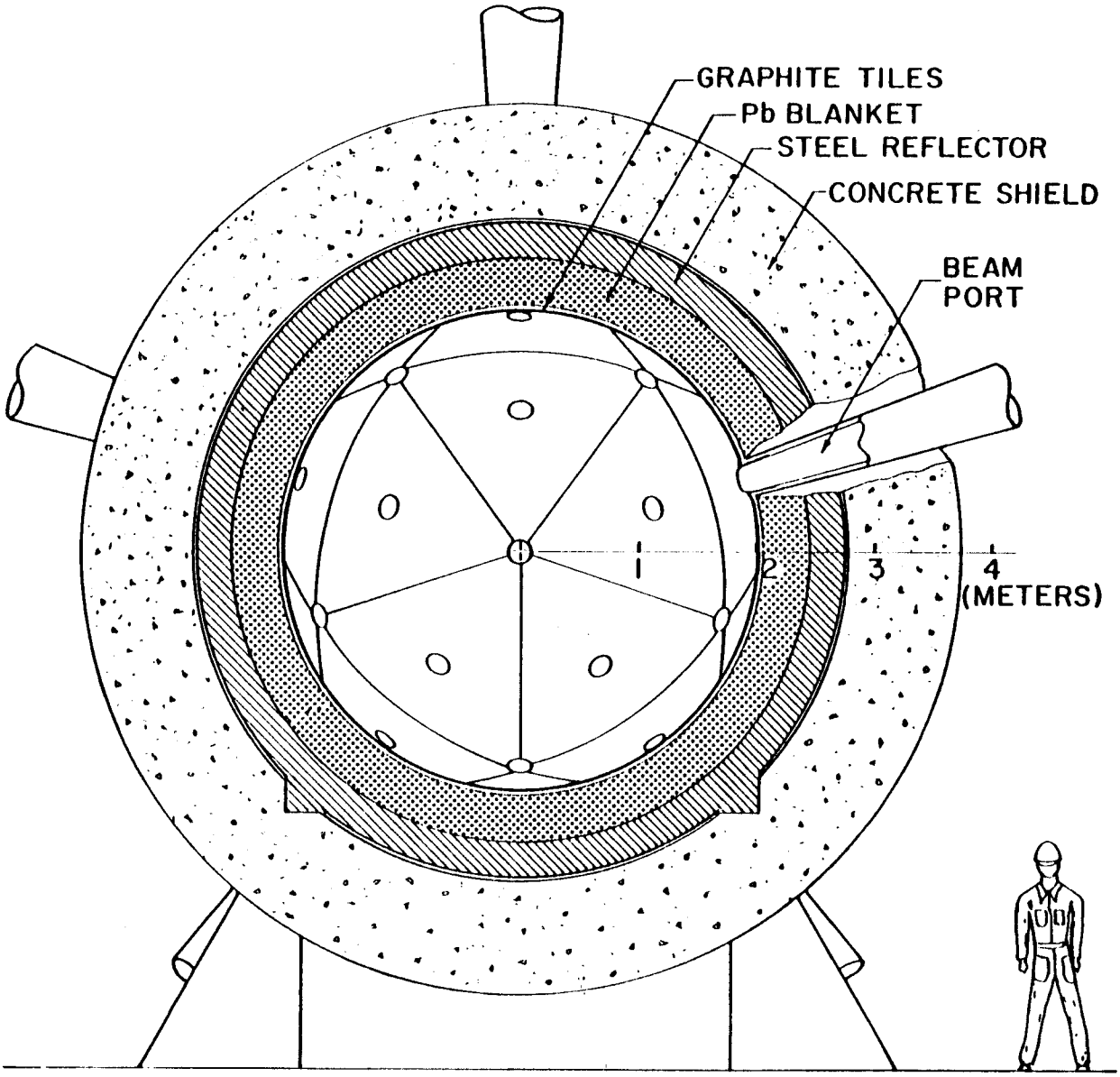

Fig. ES.2. SIRIUS-M test facility.

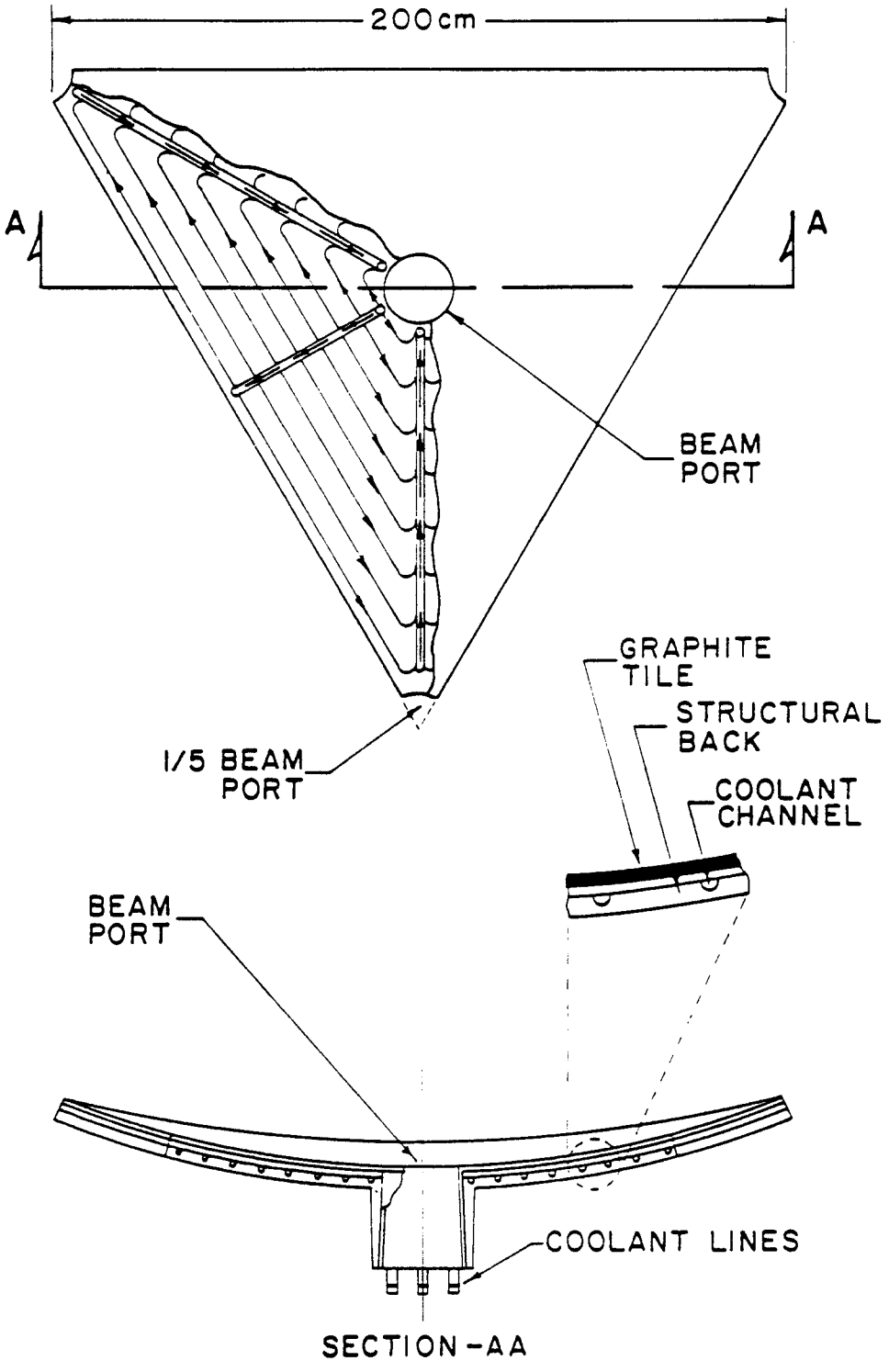

Fig. ES.3. Actively cooled graphite-faced tile.

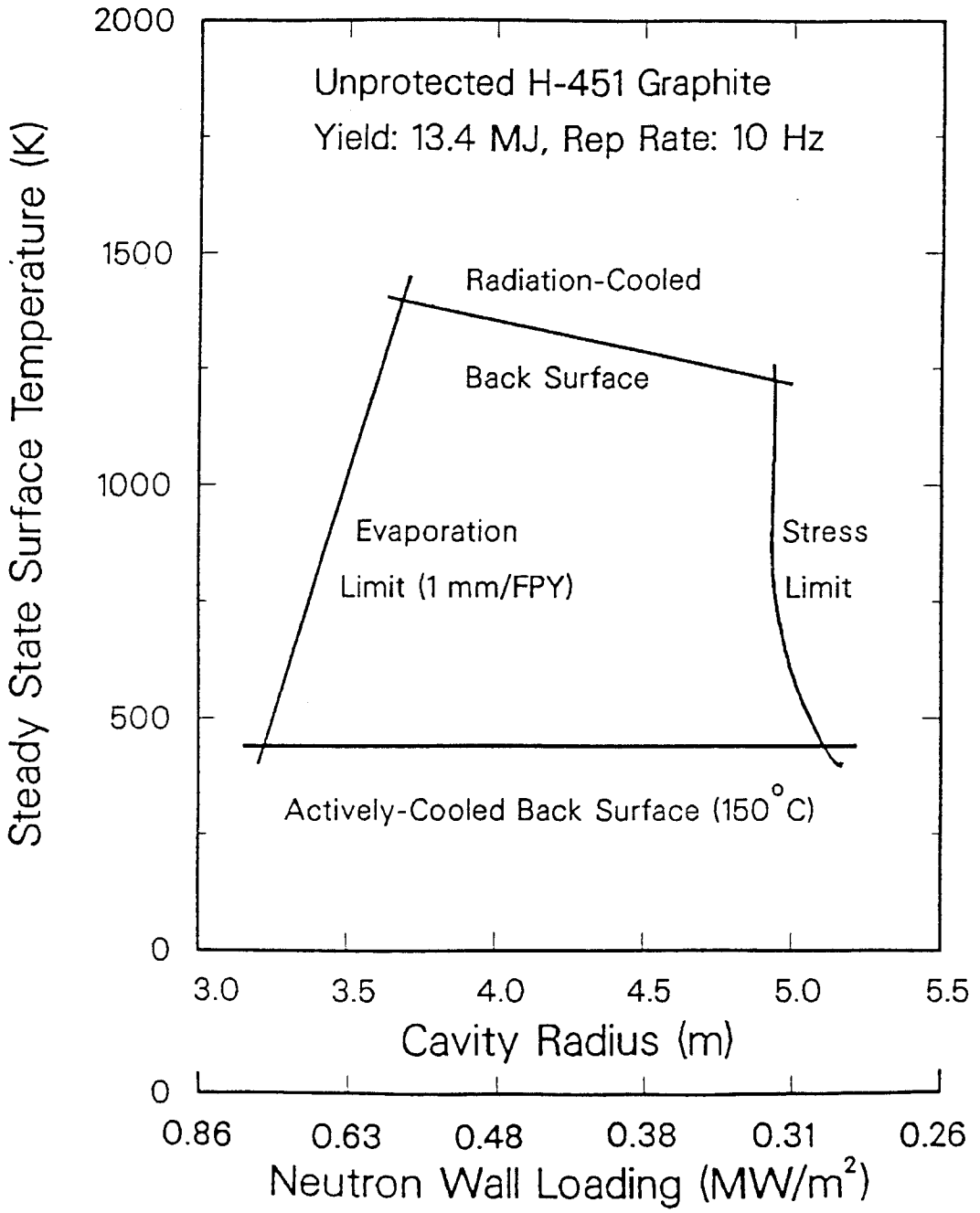

Fig. ES.4. Evaporation and stress limits for dry wall cavities.

I. INTRODUCTION

The need to test structural materials under realistic fusion reactor conditions has been discussed in both the magnetic confinement fusion (MCF) and inertial confinement fusion (ICF) communities for over a decade. Irradiating small size materials samples in a neutron flux can be accomplished in fission reactors or small DT neutron source facilities. However, the restricted temperature range and small individual test volumes, along with serious neutron energy spectral differences, make complete testing of materials in these facilities impossible. The MCF program has taken the lead in attempting to solve this problem by sponsoring several test reactor studies such as FERF,[1] TETR,[2] INTOR,[3] TASKA,[4] TASKA-M,[5] TDF[6] and FEF.[7] Most of these studies have concentrated on providing a nuclear and thermal environment which would closely simulate that to be expected in the first demonstration reactor or the first commercial magnetic fusion reactor.

In contrast to the MCF technology program, the efforts of the ICF technology program have been on conceptual design of commercial power plants and there has been a curious lack of near term test facility designs. The singular exception is a brief scoping study of a device called LA FERF[8] in 1975 at LLNL. It is commonly assumed by the ICF community that the MCF materials program will provide the data needed for designing inertial confinement reactors. However, the large differences between the damage conditions in ICF and MCF environments arising from geometrical, spectral, and temporal effects make it necessary to develop a dedicated ICF materials test facility. To this end, the Fusion Technology Institute of the University of Wisconsin (FTI) and the University of Rochester's Laboratory for Laser Energetics (LLE), in co-

operation with the Naval Research Laboratory (NRL), have conducted a study of the critical issues related to the design of an ICF materials test facility, SIRIUS-M. The facility is designed to duplicate the time-dependent radiation damage structure unique to ICF systems, in order to provide the technology base necessary for an ICF demonstration facility. This report summarizes the results obtained by the FTI and LLE team related to the SIRIUS-M design effort during 1985.

The SIRIUS-M test facility uses symmetrically-illuminated targets. Critical issues unique to symmetrically-illuminated, direct-drive ICF reactors were previously examined by the FTI and LLE team in a preliminary conceptual reactor design, SIRIUS.[9] Several features of the reactor design were studied in some detail including: target performance, first wall thermal response, reflector performance, mechanical design, and radiation damage to both the structure and final optics. The SIRIUS-M study described in this report builds on the knowledge gained in these areas.

In selecting the technical specifications and design parameters for the SIRIUS-M facility, we have attempted to limit the initial capital and operating costs by limiting the "mission" of the facility to only materials testing; tritium breeding and high-temperature recovery of thermonuclear energy are not included. The "desired" neutron wall loading has been set at $\gtrsim 2$ MW/m^2; this corresponds to an irradiation of ~ 1 $MW\text{-}yr/m^2$ per calendar year of operation so that the necessary cumulative damage can be achieved in a few years of operation. Attention has been focused on several areas unique to an ICF materials test facility including: test module design and damage rates estimation; cavity design and first wall protection; target design; and placement of the final mirrors.

The remainder of this report is organized as follows. Chapter II deals with cavity design considerations. An overall description of the facility is given in Section II.1. Thermal design analyses of the first wall are given in Section II.2 where it is shown that the high neutron wall loading specified in the SIRIUS-M design (2 MW/m^2) cannot be achieved in unprotected dry wall cavities. The SIRIUS-M first wall is protected by placing 1 torr of xenon in the cavity; analysis of the gas-protection scheme is given in Section II.2. Section II.3 deals with mechanical design considerations, namely, estimation of mechanical and thermal stresses in the first wall. Cavity gas handling and processing system is discussed in Section II.4. Chapter III deals with analyses related to materials test module design and damage rate estimation. Section III.2 gives a detailed comparison between damage conditions in ICF and MCF reactors. Parametric studies related to the test module design are given in Section III.3 while the final SIRIUS-M test module design and performance are presented in Section III.4. Chapter IV deals with target design and beam transport considerations. Tolerances for irradiation nonuniformity in direct-drive laser fusion reactors are analyzed in Section IV.1 while placement and support of the last mirrors is discussed in Section IV.2.

References for Chapter I

1. T.M. Batzer et al., "Conceptual Design of a Mirror Reactor for a Fusion Engineering Research Facility (FERF)," UCRL-51617, Aug. 1974.

2. B. Badger et al., "TETR - A Tokamak Engineering Test Reactor to Qualify Materials and Blanket Components for Early DT Fusion Power Reactors," University of Wisconsin Fusion Technology Institute Report UWFDM-191 (1977).

3. "INTOR - International Tokamak Fusion Reactor, Phase I Report," International Atomic Energy Agency, Vienna, 1982.

4. B. Badger et al., "TASKA - A Tandem Mirror Fusion Engineering Test Facility, KfK-3311/2, UWFDM-500, June 1982.

5. B. Badger et al., "TASKA-M, A Materials Test Reactor for the 1990's," KfK-3680, UWFDM-600, 1983.

6. J. Doggett et al., "A Fusion Technology Demonstration Facility (TDF)," UCRL-90824, 1984.

7. T. Kawabe, to be published.

8. J. Hovingh, "Analysis of a Laser-Initiated, Inertially-Confined Reactor for a Fusion Engineering Research Facility (LA FERF)," UCRL-76517, May 1975.

9. B. Badger et al. "Preliminary Conceptual Design of SIRIUS, A Symmetric Illumination, Direct Drive Laser Fusion Reactor," University of Wisconsin Fusion Technology Institute Report UWFDM-568 (March 1984).

II. CAVITY DESIGN CONSIDERATIONS

II.1 Cavity Description

The SIRIUS-M material test reactor cavity is of spherical configuration with an inner radius of 2 meters. The first wall consists of actively-cooled graphite faced tiles, followed by a Pb reflector, steel reflector and shield. The reactor will have two material test modules located diametrically opposite each other.

Illumination of the target within the cavity is accomplished by 32 laser beams equidistantly distributed around the sphere as shown in Figs. II.1.1 and II.1.2. Figure II.1.1 is a cross section through the center of the cavity showing the triangular first wall tiles, the lead reflector, steel reflector and concrete shield. Figure II.1.2 is an isometric view of the cavity with only the reflector showing, and includes a cutaway for one of the two material test module locations on opposite sides of the cavity. The beam distribution is based on a twenty sided icosahedron, where the sides are equilateral triangles superimposed on a spherical surface. The thirty-two equidistant points on the sphere come from the centers of each triangle (20) plus the points at which the vertices of the triangles converge (12).

The main effort related to cavity design considerations thus far has been in the area of first wall protection, whereas a detailed design of the cavity is part of future tasks. In the following sections, a brief description of the various cavity components will first be made followed by detailed analyses of protected and unprotected first walls.

II.1.1 Protective Tiles

The first wall is protected with twenty water cooled graphite faced tiles shaped as equilateral triangles which conform to a spherical surface. One beam port is located in the center of the triangle, and the vertices of each triangle subtend one fifth of the circumference of each of the beam ports at the vertices, as shown in Fig. II.1.3.

The tiles consist of a ferritic stainless steel (HT-9) base structure, of 2 cm nominal thickness which has cooling channels machined in it. The base structure has a collar in the center which is the primary support for the tile. Cooling line fittings are built into the support collar. A 1 cm thick graphite surface is brazed to the front of the tile. The graphite also has a collar which extends into the base structure collar.

Each tile is supported only on the central collar. The tiles are unrestrained at any other point and in this sense will not be subjected to high thermal stresses. Insertion of the tiles will be from the inside of the cavity. The outer side of the collars will have a reverse conical configuration from the beam tube to which it is attached, thus making insertion from inside of the cavity possible. A locking mechanism on the collar can be envisaged to anchor the tile to the beam port, along with guide slots for orienting the tile within the cavity. The coolant lines will terminate in fittings which will mate with corresponding fittings in the reflector structure. Sealing of the fittings can be accomplished with a brazing material, with heat supplied by the mounting fixture at the time of tile attachment. Routing of the cooling water is shown in Fig. II.1.3. Finally, four of the twenty tiles will have to be modified to accommodate the material test modules. The details of the modification are yet to be determined.

have to be modified to accommodate the material test modules. The details of the modification are yet to be determined.

II.1.2 Reflector and Shield

Figure II.1.1 shows the Pb reflector as a continuous spherical shell, 40 cm thick which is penetrated by the 32 beam ports. Further, the reflector will have two more penetrations for accommodating the material test modules, each located between three beam ports as shown in Fig. II.1.2.

Although the Pb reflector has not yet been designed in detail, as presently envisaged it consists of two concentric spherical HT-9 shells, with the inner shell supported on the outer by means of the beam tubes. The space between the shells is filled with molten lead which can be circulated for cooling, or separately cooled by tubes embedded in it. Pressurized water cooling as in the case of the tiles, or even steam or helium gas can be utilized. Since 40 cm of lead is a very heavy load, the primary support structure for the reflector will be the 30 cm thick steel reflector which is made of HT-9. In principle, there is no reason why the outer shell of the reflector cannot support itself. This will depend on where the vacuum boundary is located and on the cooling connections. Fabrication consideration may also preclude the possibility of combining the Pb reflector and steel reflector into a single structure. These decisions can only be made when a more detailed design is available.

Figure II.1.1 shows a concrete biological shield immediately following the reflector. This shield is needed to make the region behind the cavity accessible for maintenance a reasonable time after shutdown. The thickness depends on whether limited hands on maintenance is contemplated for this re-

gion. In the event hands on maintenance will be used, the beam tubes will have to be shielded as well. Once the requirements for the shield are established, the thickness and the degree of beam tube shielding can be determined.

II.1.3 Vacuum Considerations

During operation, the cavity will have an atmosphere of xenon gas at a pressure of one torr. As will be discussed later, the gas is used to protect the first wall from the target debris and soft x-rays produced by the micro-explosion. This gas atmosphere exists also in the beam tubes up to a point where some kind of window will separate it from the environment of the laser. Just where the vacuum boundary is located is very critical in the design of the cavity, since this boundary will experience one atmosphere of pressure.

In the past we have considered the reflector as the vacuum boundary. If this is the case, then the final mirrors will have to be sealed within the beam tubes and be supported on the beam tubes. The reflector and the beam tubes will then be the vacuum boundary for the cavity.

Another option is to put the vacuum boundary further back, beyond the final focusing mirrors. This would obviate the need for beam tubes between the cavity and the final mirrors, and the laser light would simply be focused into the holes through the cavity. An obvious advantage here is that the cavity can be isolated from the mirror support structure and mirror maintenance becomes easier. The disadvantage is that the vacuum chamber is much larger and more xenon gas will be needed. These options will be evaluated to determine the most cost effective way for locating the vacuum boundary.

Pumping requirements at this pressure are quite minimal and can be adapted to either of the options discussed. Several of the beam tubes can

have pumping ports attached to them in the case of the first option. In the second option a pump station will be located at the vacuum boundary and the gas simply exhausted through the beam port holes in the cavity.

II.1.4 Reactor Maintenance

There are three elements of the reactor which will require routine maintenance. They are:

1. Final mirrors.
2. Graphite tiles.
3. Coolant connection in back of the shield.

The final mirrors are directly exposed to neutrons, and will have to be replaced on a yet to be determined schedule. Support structures in the vicinity of the final mirrors will be activated and, therefore, this function will most likely require remote maintenance. Further, access to the final mirror will be impeded by beam tubes and other structures in the way. Replacement of the mirrors will have to be accomplished by a special purpose maintenance machine which can travel on guides to each mirror location. Final alignment of the mirror can be accomplished remotely from the control room.

Graphite faced tiles may need replacing sometime during the life of the reactor. Access to the inside of the reactor cavity will be needed for this purpose. The 1.14 m diameter penetrations for the material test modules can be used for insertion of a remote control special purpose device which can service the tiles. Some modification of one of the penetrations may have to be made to be able to insert a tile which is ~ 2 m at its widest point.

Finally, some provision must be made for servicing the coolant lines at the back of the cavity. A special purpose machine designed to maneuver in the

space behind the shield will be needed for this task. General purpose manipulators mounted on the machine should be able to fulfill the requirements of maintaining the coolant lines. Limited hands on maintenance will make this function much easier.

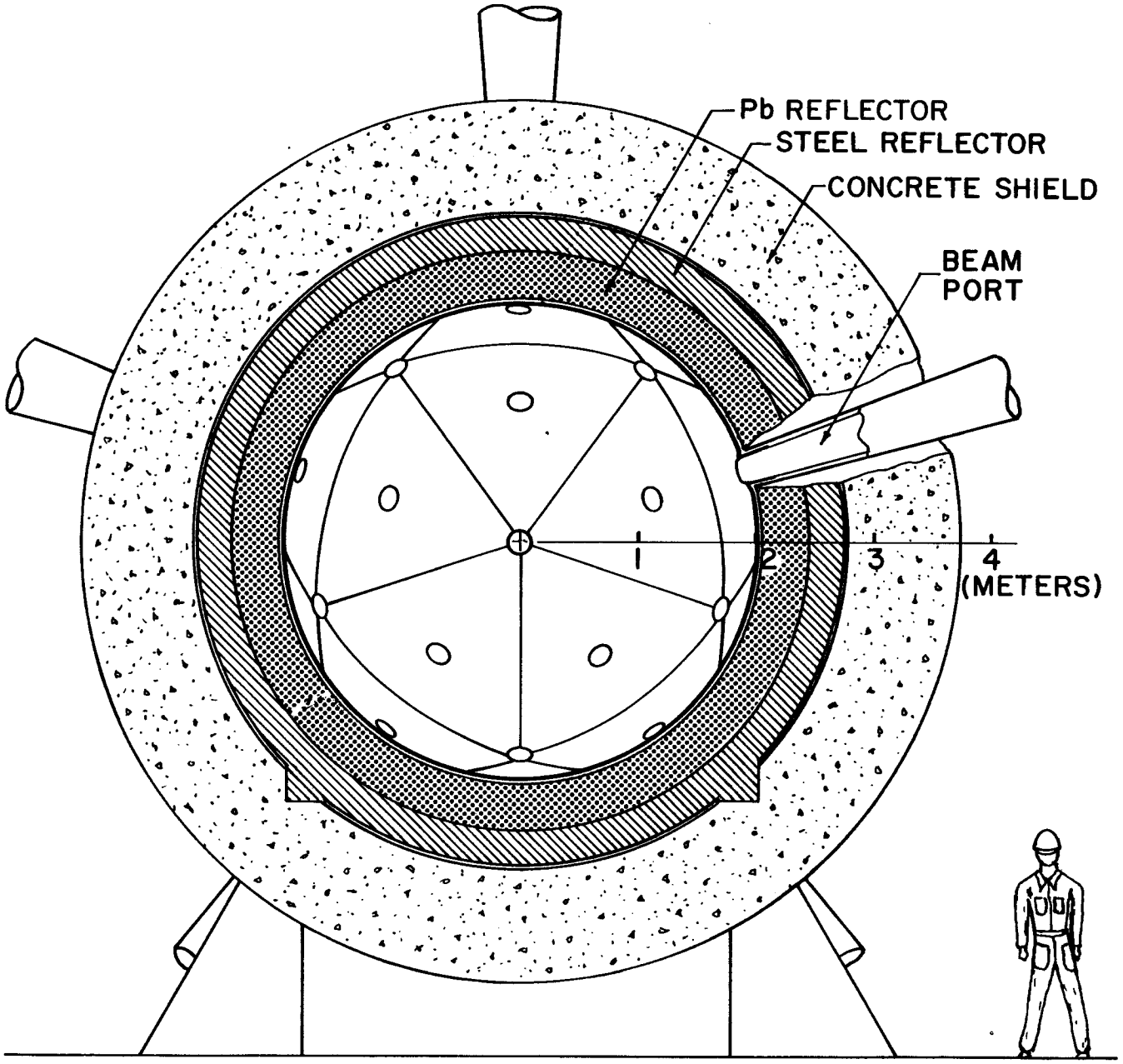

Fig. II.1.1 SIRIUS-M

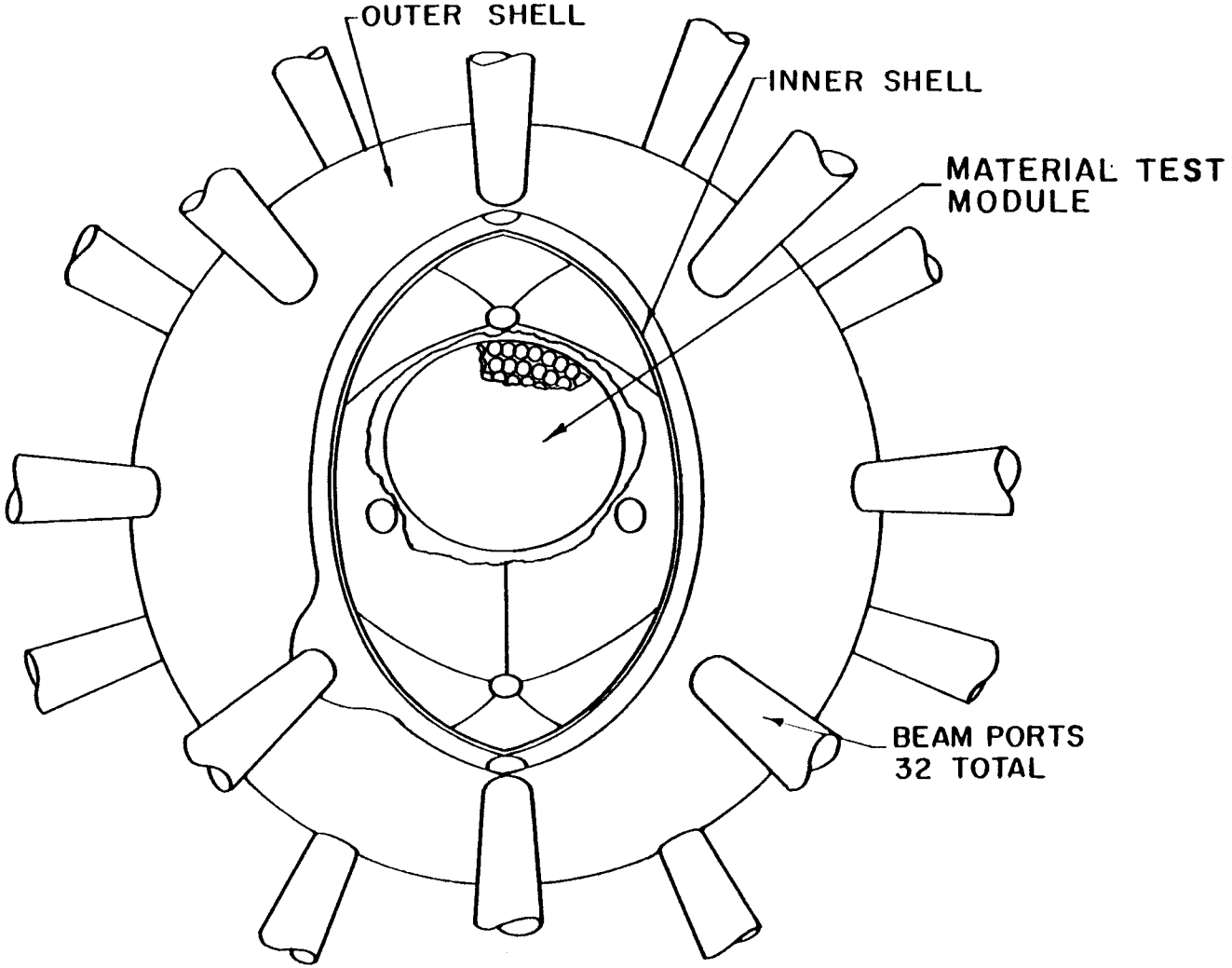

ISOMETRIC VIEW OF SIRIUS-M CHAMBER WITH CUTAWAY

Fig. II.1.2

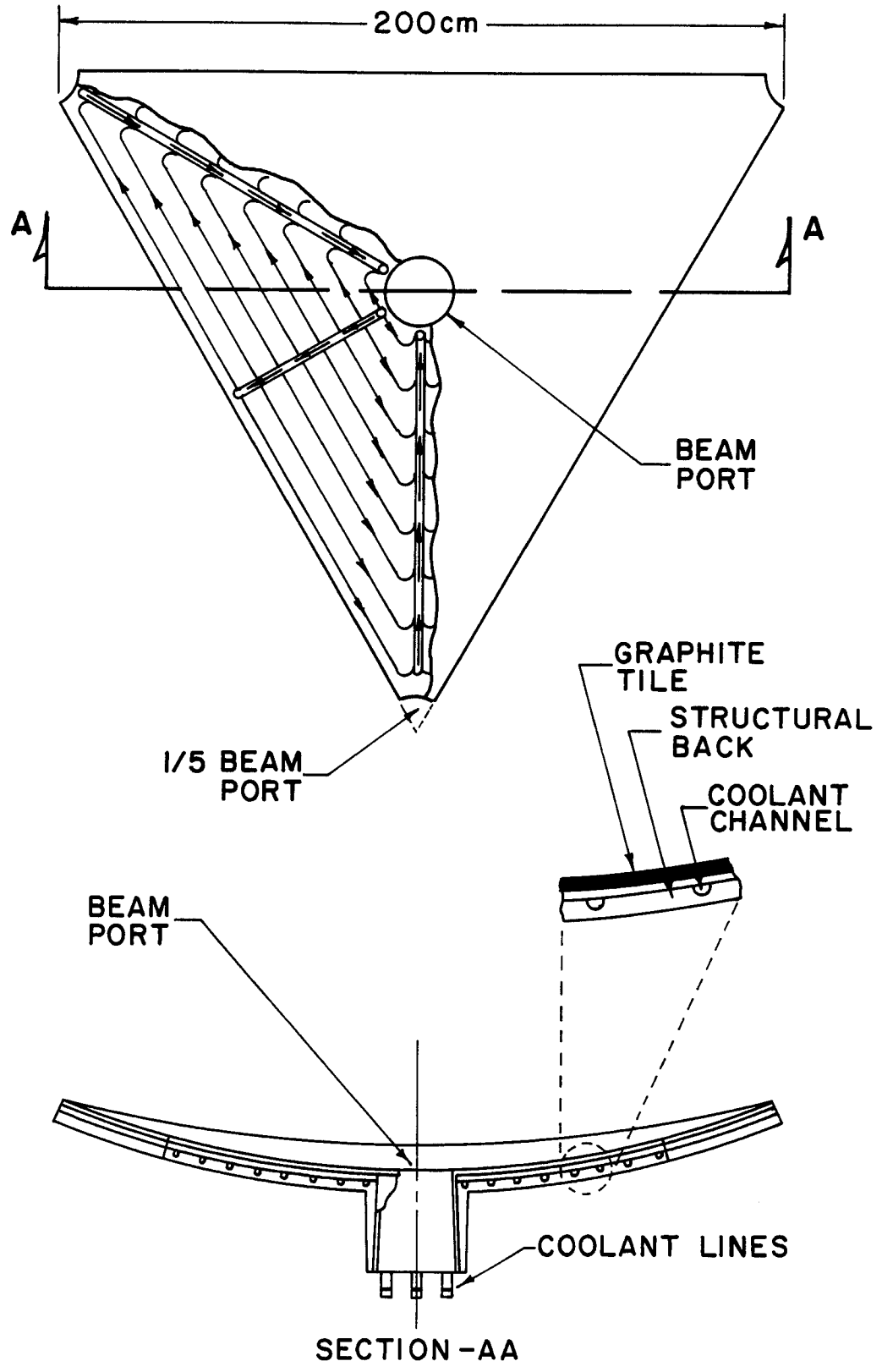

ACTIVELY COOLED GRAPHITE-FACED TILE

Fig. II.1.3

II.2 First Wall Thermal Response

The thermal response of the SIRIUS-M graphite-tiled first wall (FW) due to the different types of radiation released during the microexplosion of the target, has been analyzed for both unprotected and gas-protected walls. The final design utilizes Xe gas to protect the wall from the direct deposition of the energy associated with the ionic debris and soft x-rays. The temperatures and evaporation rates of the FW were calculated for different cavity radii. For an unprotected graphite-tiled first wall, the minimum cavity radius was calculated to be ~ 3.25 m without exceeding the evaporation rate of 1 mm/FPY (full power year). This evaporation rate was chosen as an acceptable limit for the design. However, the stresses in the unprotected graphite tiles impose a more severe limit on the wall loading resulting in a larger cavity (~ 5.1 m). This means that the maximum wall loading for an unprotected cavity will be considerably lower than the required design value of 2 MW/m^2. In the following, the thermal design of both the unprotected and the gas-protected first wall will be presented. Gas protection was judged necessary to obtain the high wall loading design value for this facility.

II.2.1 Radiation Spectra and Energy Deposition

The x-ray and ion spectra used in these calculations were scaled from the SIRIUS[1] spectra in order to correspond to the lower target yield used in SIRIUS-M with some adjustments. These adjustments were made mainly in the ion spectra. First, the number of ions was adjusted to yield a total ion energy of 2.6 MJ. Second, we have replaced the monoenergetic spectra of the ions by narrow Gaussian spectra. This establishes a time base or difference for the ion pulses which is necessary to carry out the calculations. The ion spectra

used are given in Table II.2.1. As shown in this table the carbon ions carry about 66% of the 2.6 MJ ionic debris energy.

Figure II.2.1 shows the ion spectra, with the neutron spectrum included. The energy deposition rates of all the ions as a function of time and depth of the first wall are mapped in Figs. II.2.2 through II.2.6. The summation of these rates is shown in Fig. II.2.7.

The amplitude of the x-ray spectrum was scaled down from the SIRIUS[1] target spectrum to yield a total x-ray energy of 0.8 MJ. The spectrum of the x-rays is shown in Fig. II.2.8 together with that of ions and neutrons. The attenuation coefficient of the graphite for the x-ray spectrum is shown in Fig. II.2.9; this has been used to calculate the deposited x-ray energy in the first wall, the distribution of which is shown in Fig. II.2.10 for a cavity radius of 5 m. The x-ray energy is assumed to be emitted in 20 ps.

In addition to x-rays, ions, and neutrons, the FW is irradiated by the portion of the laser light reflected from the target. The KrF laser (λ = 0.248 μ) used in SIRIUS-M uniformly delivers 1 MJ to the target, in about 11 ns. In this analysis we assume that 10% (i.e., 100 KJ) of the laser energy is reflected and refracted from the target[2] and is ultimately absorbed by the first wall. Depending on the reflectivity of the FW materials, part of this laser energy will be absorbed while the remainder will be reflected. In the spherical geometry of SIRIUS-M, and with the assumption of uniform and normal incidence of the light on the wall, the reflected portion from one location on the wall will strike the opposite side. In effect, a train of laser pulses with rapidly attenuated amplitudes will strike the FW. This situation is illustrated in Fig. II.2.11, where the powers of the incident laser pulses are shown for different reflectivities (ρ) of the FW material.

Table II.2.1. SIRIUS-M Ion Spectra

Ion	Energy (keV)		No. of Ions	Energy (MJ)
	Mean	Spread		
H	137.5	±1	1.31×10^{19}	0.2876
D	92.5	±1	1.21×10^{19}	0.1797
T	139	±1	1.21×10^{19}	0.2699
He	185	±1	4.67×10^{18}	0.1382
C	1649	±2	6.54×10^{18}	1.725

The reflectivity of any material depends on the angle of incidence, the incident wavelength, power density, and temperature. The optical properties of graphite as a function of these parameters are not available. A monochromatic hemispherical reflectivity of 50% has been assumed for the graphite tiles. This value is based on data for the total hemispherical absorptivity of graphite at the expected operating temperatures which varies between 40% and 60%.

For the short wavelength of the KrF laser, one can assume that the absorbed fraction of the incident laser light will be absorbed at the surface of the wall.[3] It could, therefore, be dealt with as a surface heat flux, which is the assumption used in these calculations. The temperature responses at the front surface of the graphite FW due to the laser pulses shown in Fig. II.2.11, are shown in Fig. II.2.12 for the base case of 2 m radius. As it turned out, the laser light produces the largest temperature rise at the front

surface for this case, as will be seen later. However, little material loss (evaporation) is caused by these pulses because of the small amount of energy involved in these very short pulses.

Figure II.2.13 shows the incident power on the first wall from the differing radiation mentioned above for the case of a 5 m cavity radius as a function of time. The time reference point (t = 0) corresponds to the instant when the laser pulse hits the target. No reflection of the laser from the wall is shown in this figure, i.e. only the reflected light from the target to the first wall is shown.

II.2.2 Thermal Response of Unprotected Graphite First Wall

Using the energy deposition described above together with the graphite thermal properties shown in Fig. II.2.14, the temperature in the first wall was calculated for different radii and different steady state temperatures. The steady state temperature is the front surface temperature reached before the following microexplosion debris reaches the wall. The value of the steady state temperature depends on the method used to cool the first wall. For the actively cooled tiles used in SIRIUS-M, the steady state surface temperature is ~ 500°K. The computer code used in these calculations is a greatly modified and enhanced version of the two computer codes T*DAMEN[4] and A*THERMAL.[5]

Figure II.2.15 shows the temperature rise at the front surface of the wall for different values of the cavity radius, as a function of time for a steady state temperature of 500°K. These results show that the surface temperature reaches its steady state value (i.e., temperature rise = zero) in approximately 1 ms, well before the following explosion which occurs 100 ms later (rep. rate = 10 Hz). Figure II.2.16 shows the maximum temperature at

the front surface of the FW for different steady state surface temperatures (T_b) and cavity radii. The evaporation rates for the different temperature histories shown in Fig. II.2.15 are shown in Fig. II.2.17. For an evaporation limit of 1 mm/FPY, the minimum cavity radius would be 3.25 m for T_b = 500°K. This radius corresponds to a 0.76 MW/m^2 neutron wall loading which is considerably less than the required goal of 2 MW/m^2 for SIRIUS-M. In addition, calculations of the FW thermal stresses (Section II.3) corresponding to the temperature histories in Fig. II.2.15 have shown that the minimum radius that gives acceptable stresses is about 5.1 m. Thus, it is evident that the use of a protective scheme, like the gas protection we are employing, is necessary to have high neutron wall loading and compact (small radii) design with reasonable temperatures and stresses.

References for Sections II.2.1 and II.2.2

1. B. Badger et al., "Preliminary Conceptual Design of SIRIUS, A Symmetric Illumination, Direct Drive Laser Fusion Reactor," University of Wisconsin Fusion Technology Institute Report UWFDM-568 (March 1984).

2. R.S. Craxton and R.L. McCrory, UR LLE, Report No. 108 (1980).

3. R.W. Conn et al., "SOLASE, A Laser Fusion Reactor Study," University of Wisconsin Fusion Technology Institute Report UWFDM-220 (1977).

4. T.O. Hunter and G.L. Kulcinski, "T*DAMEN, A Computer Code for Transient Radiation Damage Analysis," University of Wisconsin Fusion Technology Institute Report UWFDM-247 (1978).

5. A. Hassanein, "Thermal Effects and Erosion Rates Resulting from Intense Deposition of Energy in Fusion Reactor First Walls," University of Wisconsin Fusion Technology Institute Report UWFDM-465 (1982).

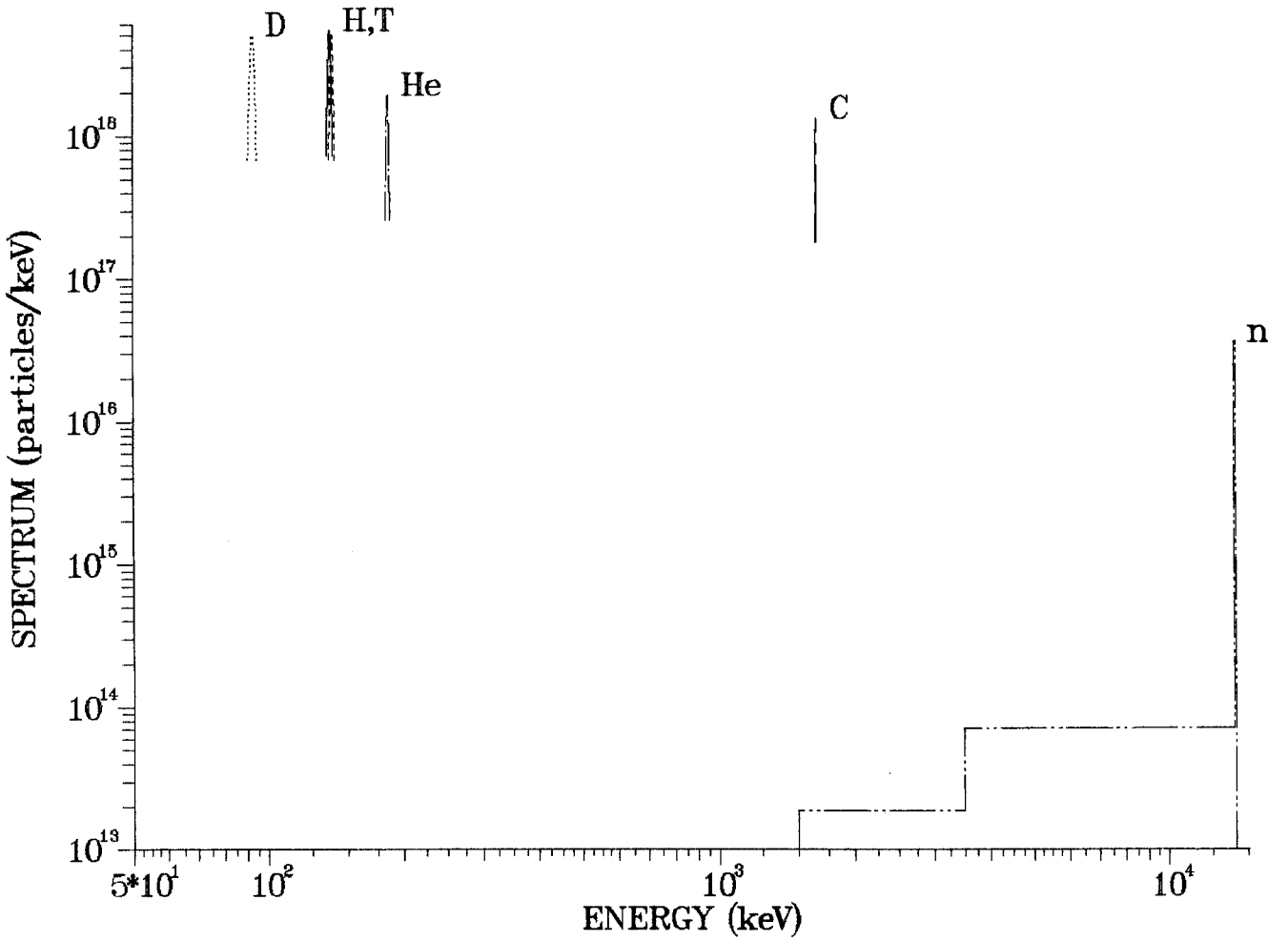

Fig. II.2.1. Ion and neutron spectra for SIRIUS-M target.

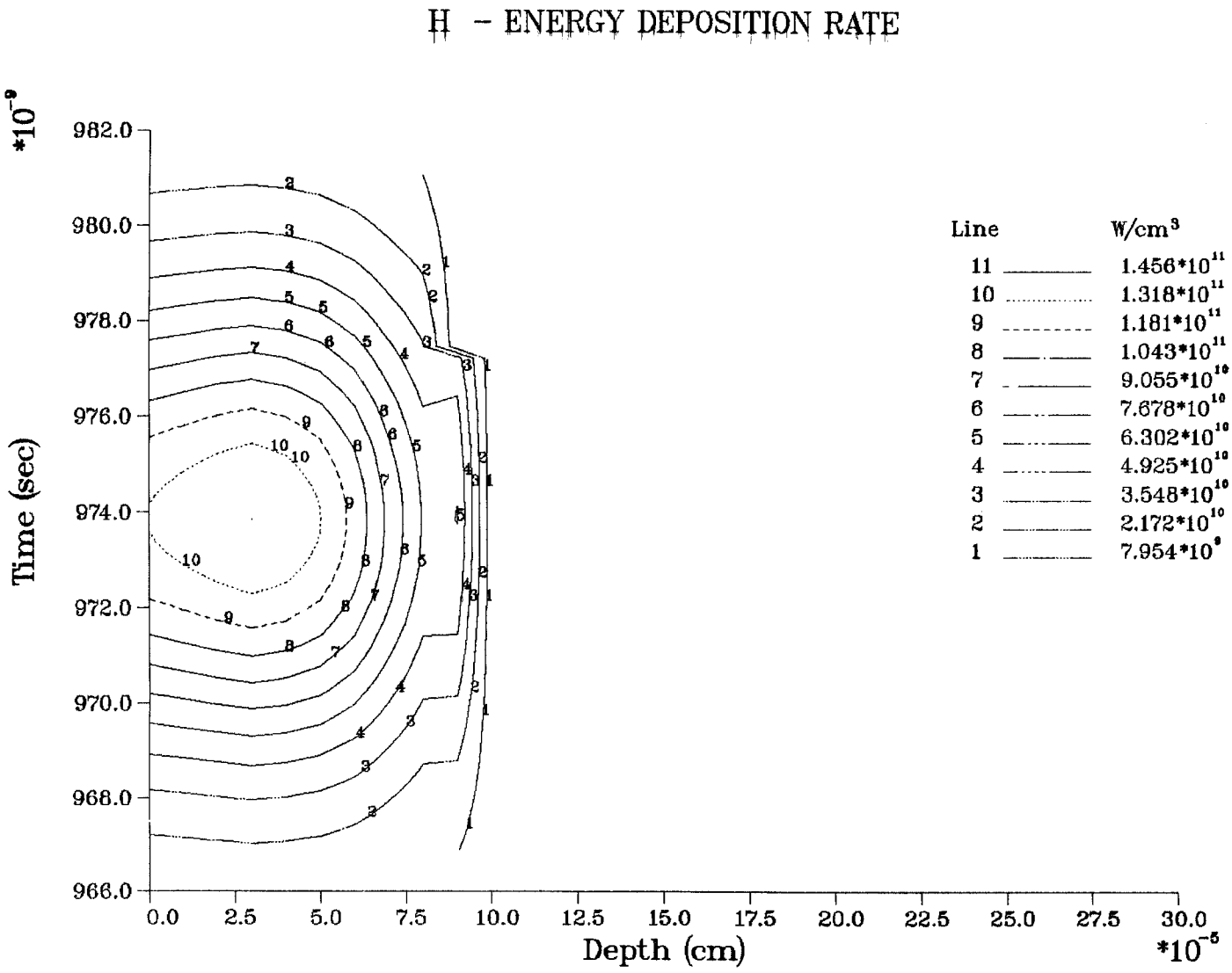

Fig. II.2.2. Energy deposition rate of hydrogen ions.

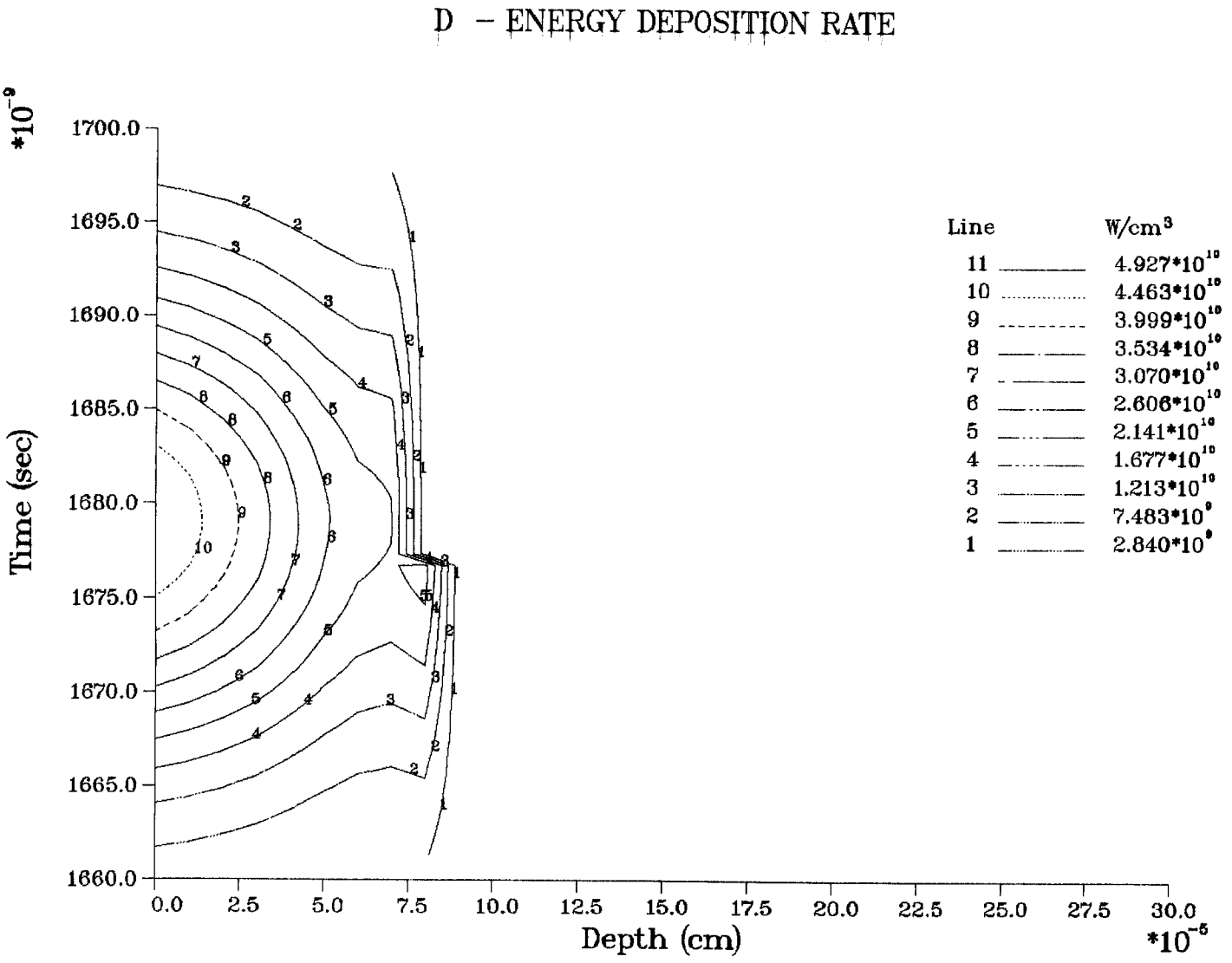

Fig. II.2.3. Energy deposition rate of deuterium ions.

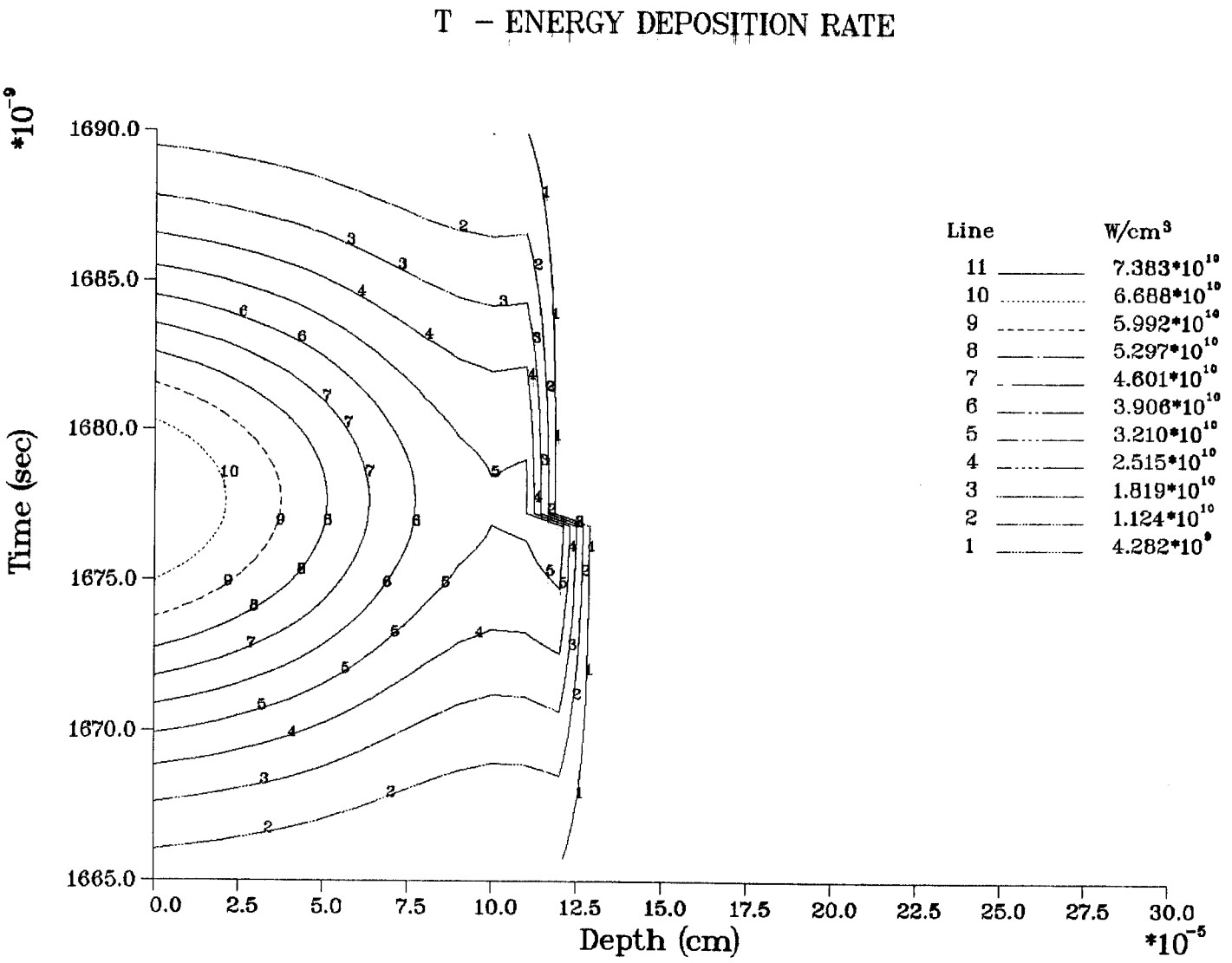

Fig. II.2.4. Energy deposition rate of tritium ions.

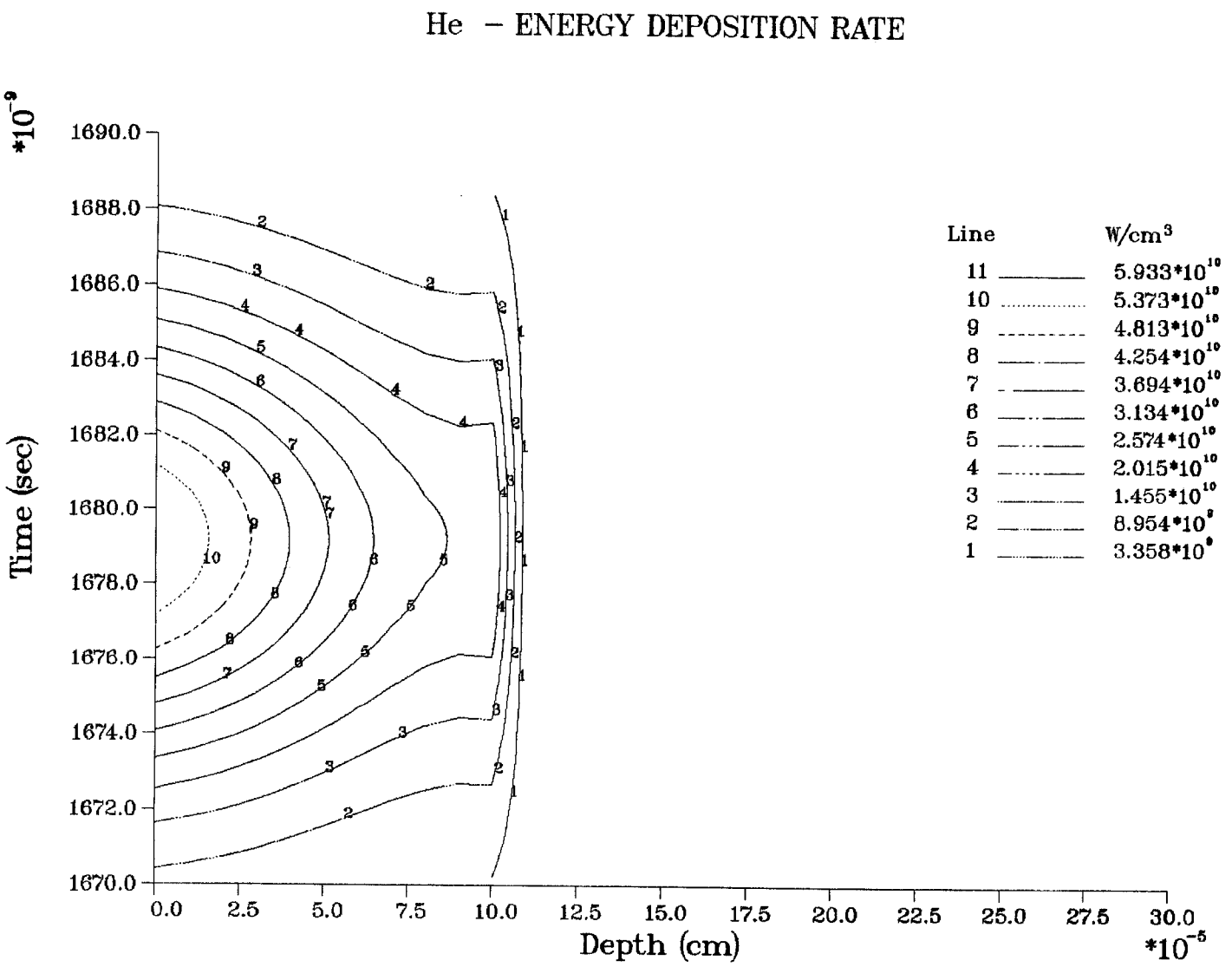

Fig. II.2.5. Energy deposition rate of helium ions.

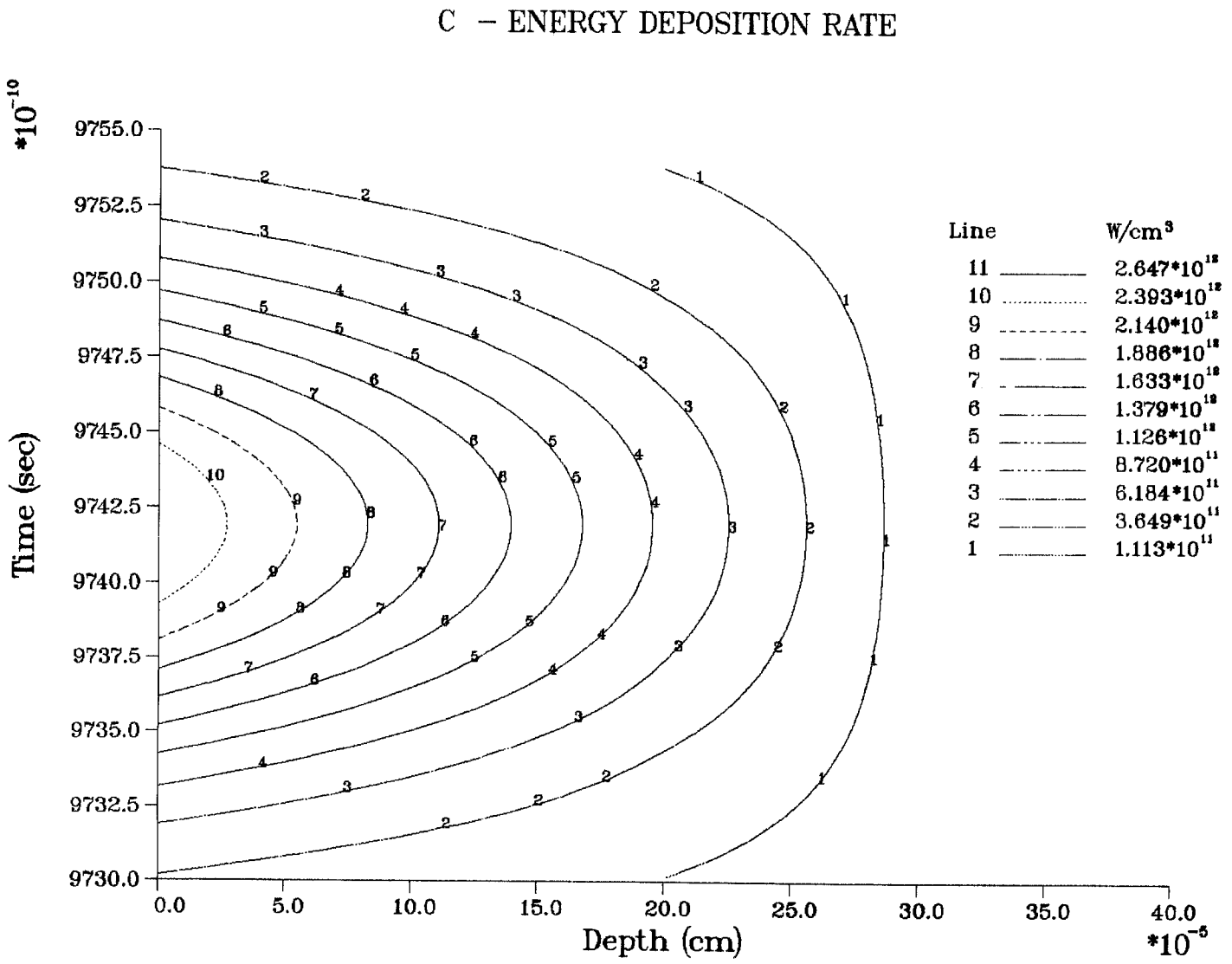

Fig. II.2.6. Energy deposition rate of carbon ions.

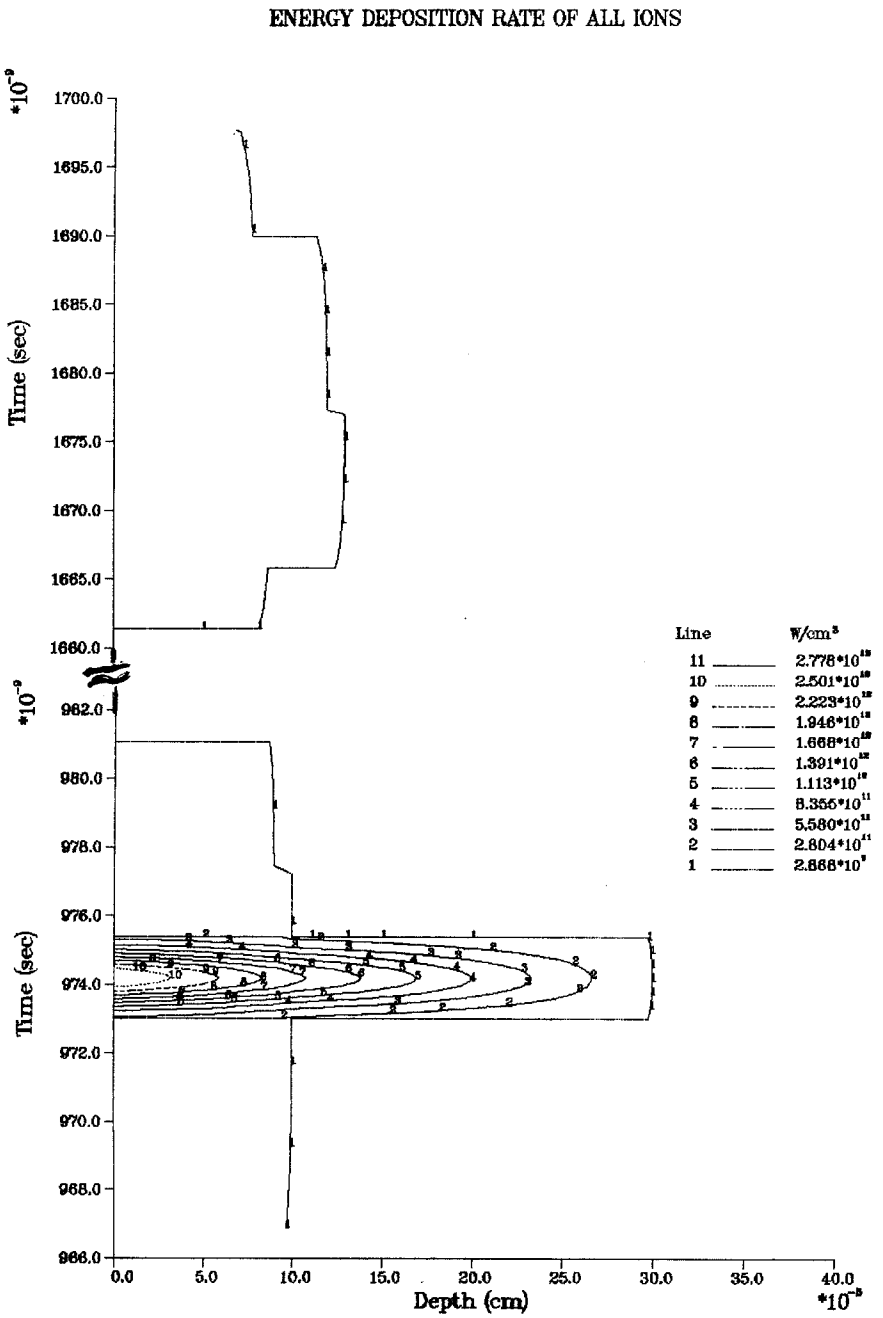

Fig. II.2.7. Total energy deposition rate of all ions.

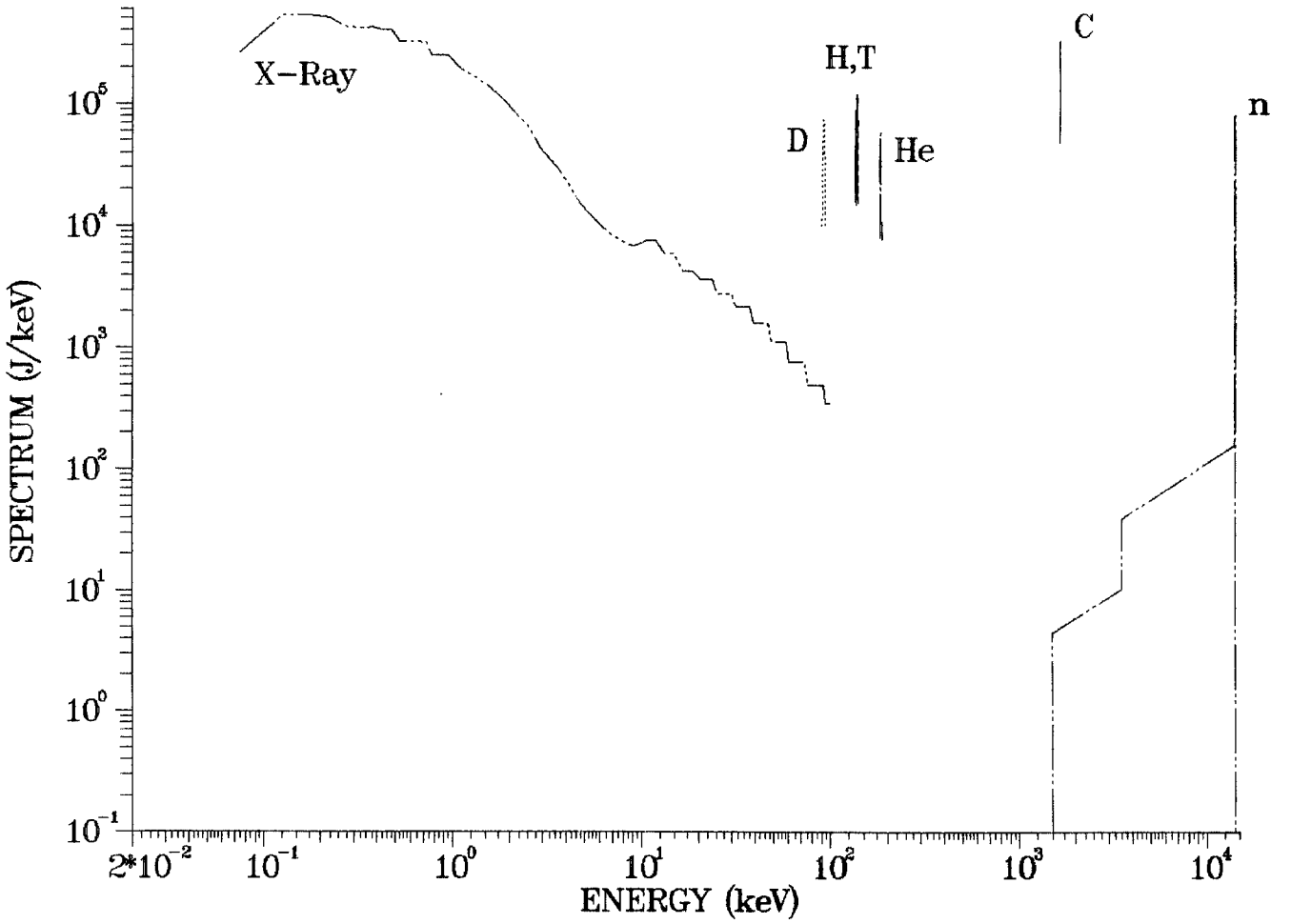

Fig. II.2.8. X-ray, ion, and neutron spectra.

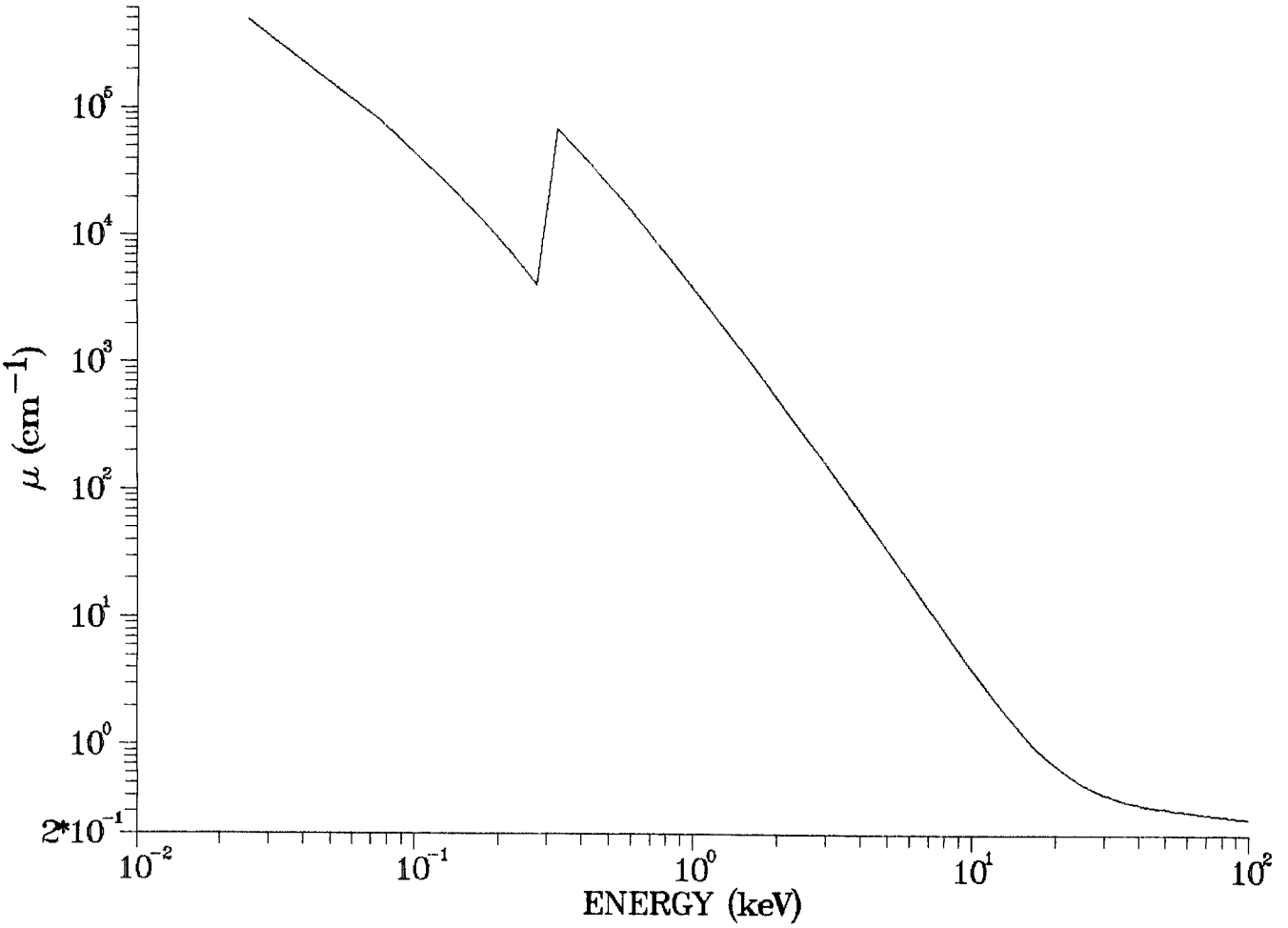

Fig. II.2.9. Graphite photon cross section.

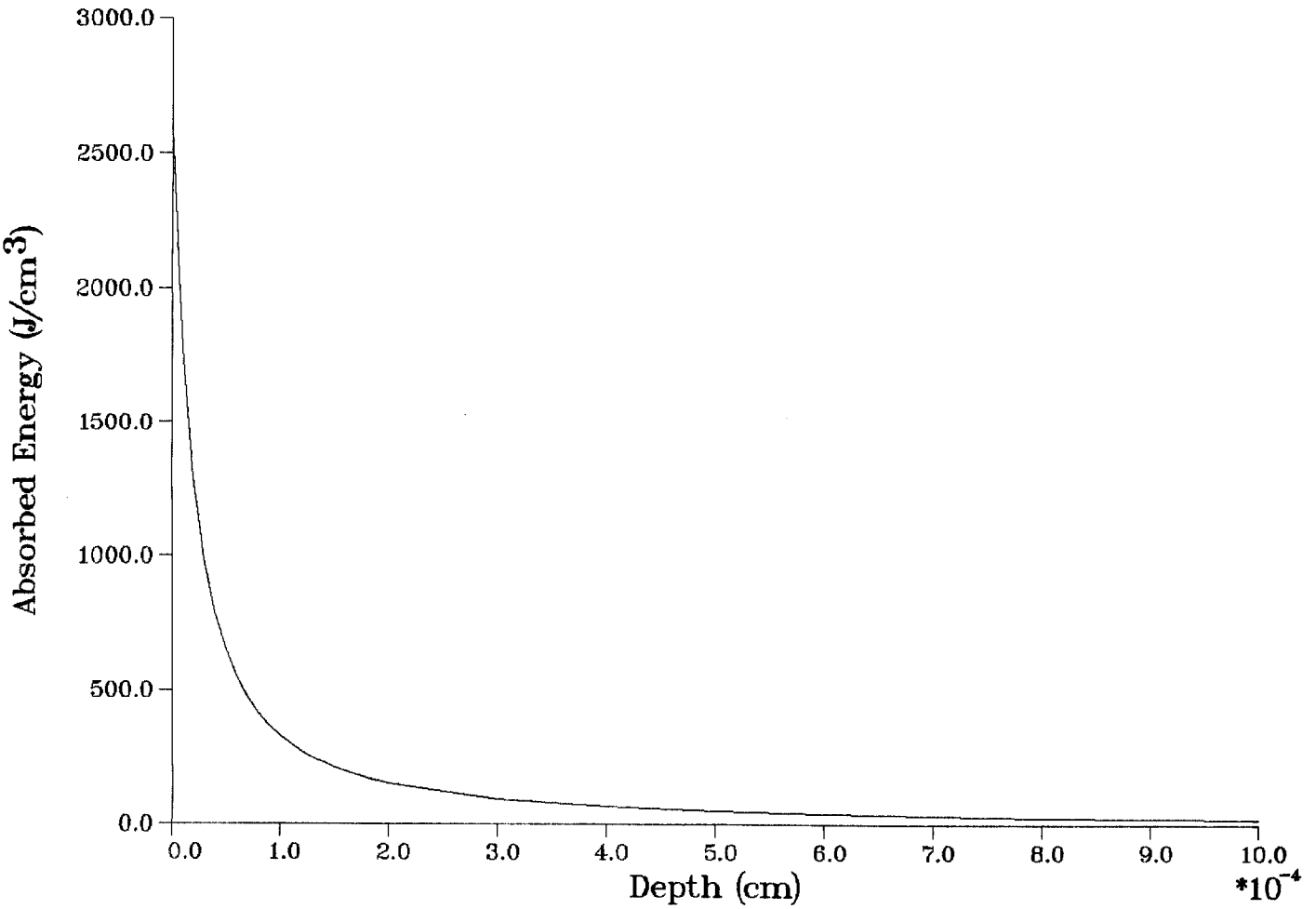

Fig. II.2.10. Absorbed x-ray energy distribution in graphite (R = 5).

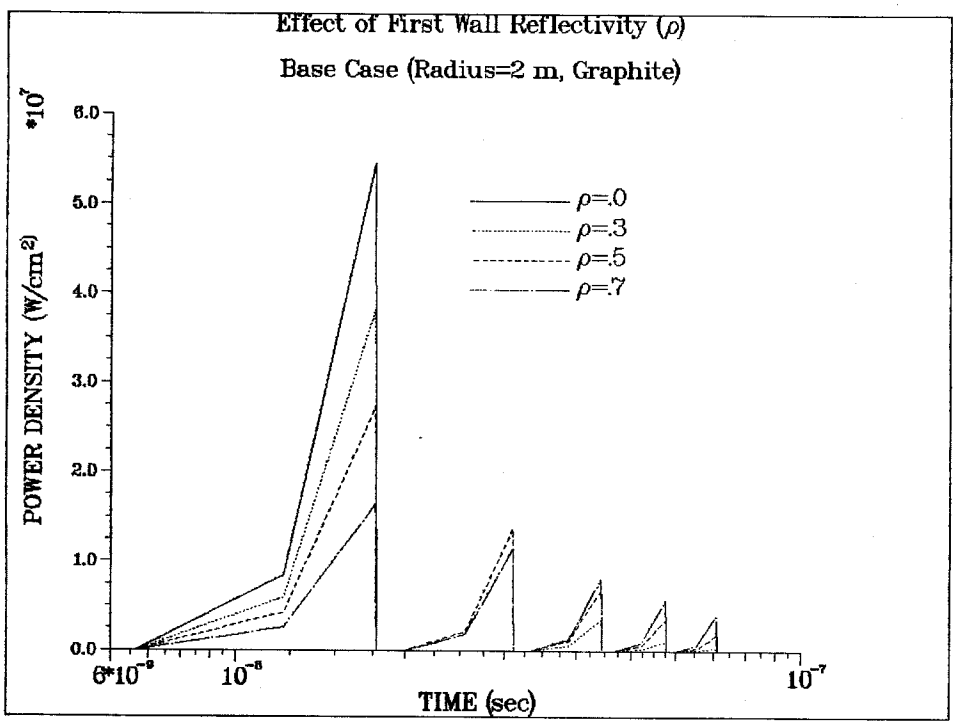

Fig. II.2.11. Incident laser pulses on the FW for different FW reflectivities.

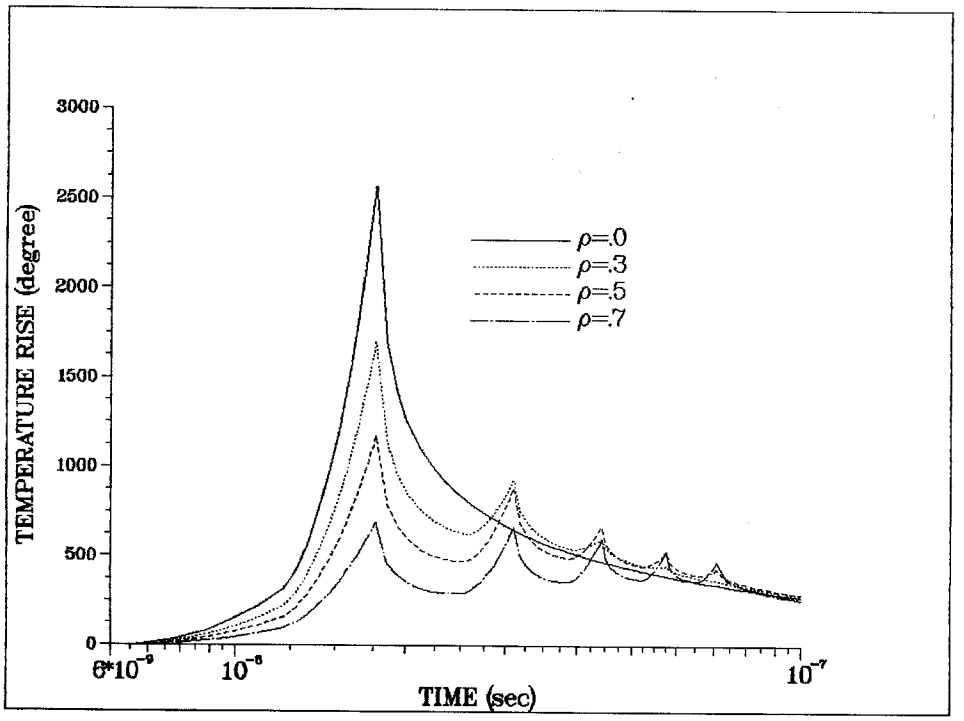

Fig. II.2.12. Temperature response of the FW for the laser pulses shown in Fig. II.2.11.

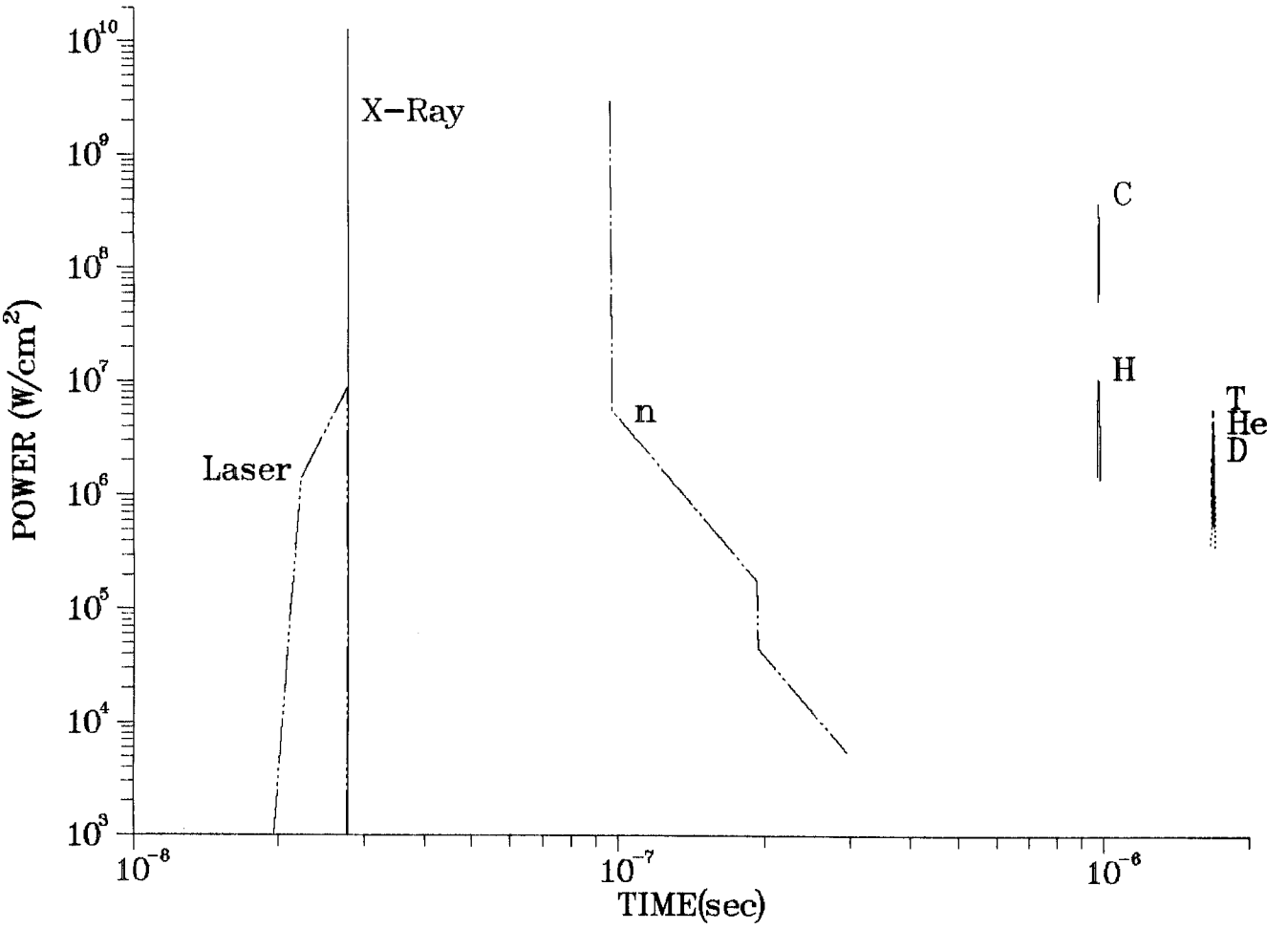

Fig. II.2.13. Incident power on an unprotected FW (R = 5 m) due to x-rays, ions, neutrons and laser reflected from the target.

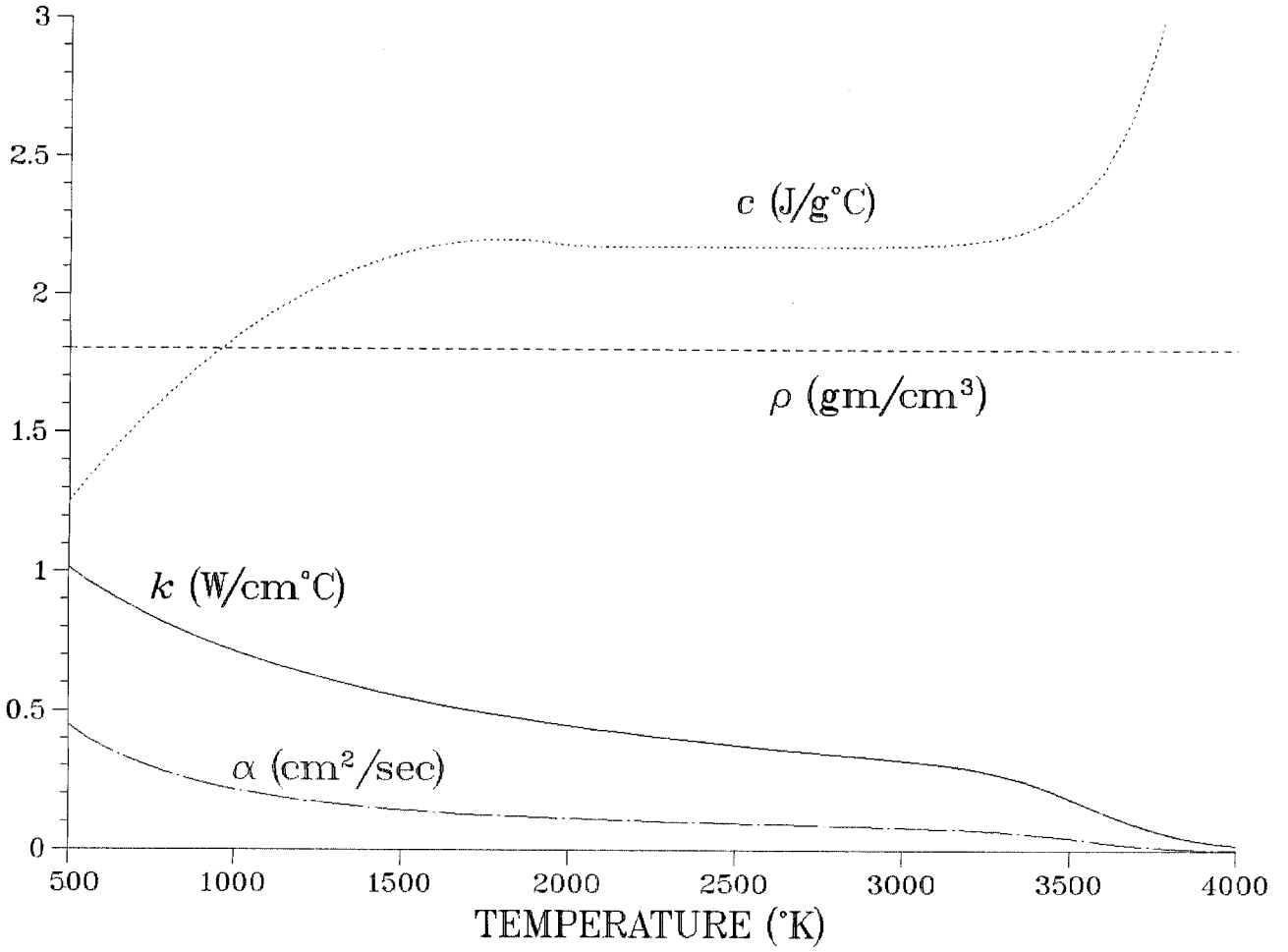

Fig. II.2.14. Graphite thermal properties as a function of temperature: density ρ, conductivity k, diffusivity α, specific heat c.

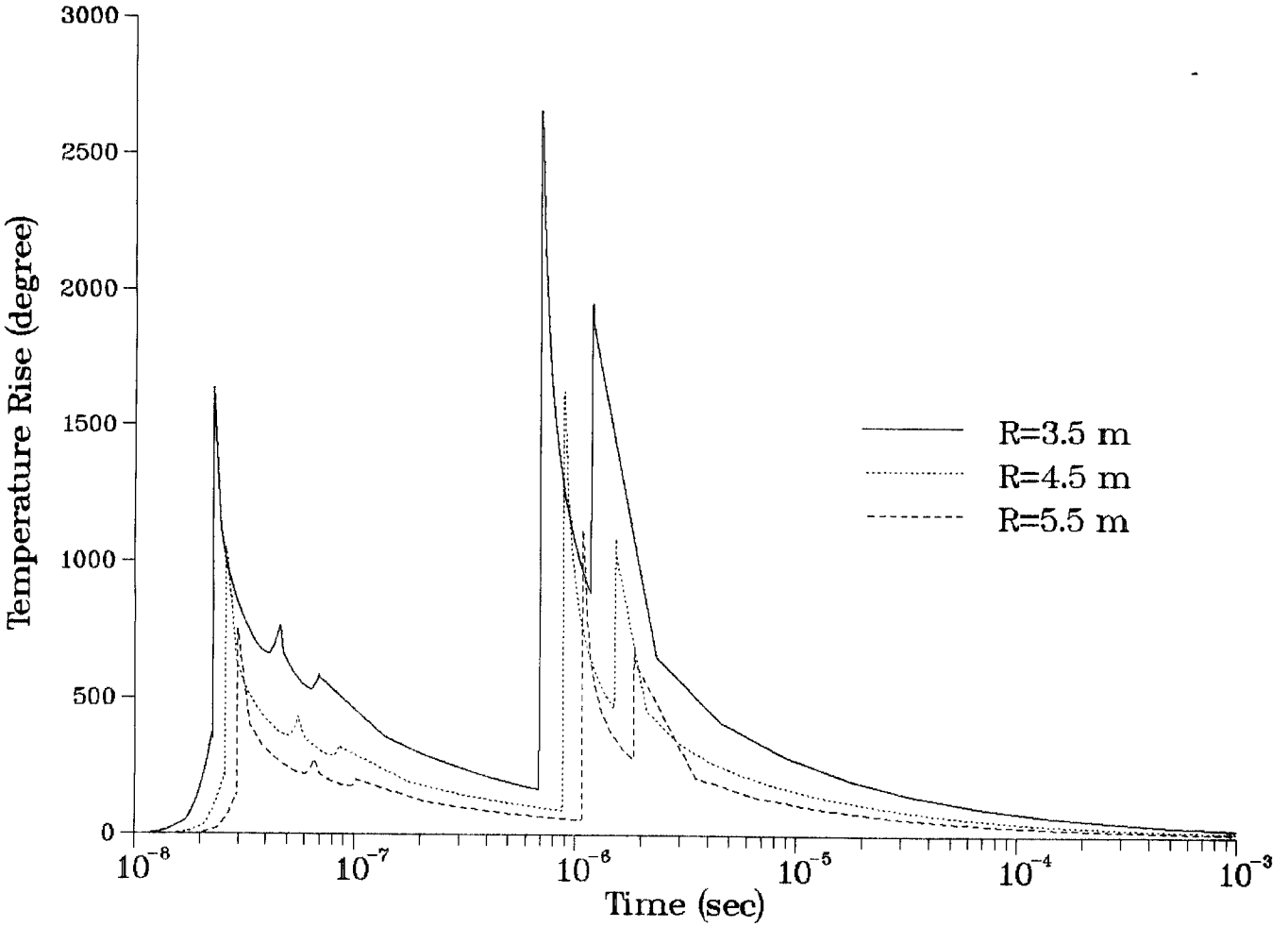

Fig. II.2.15. Temperature rise at the front surfaces of the FW for a cavity radius of 3.5, 4.5 and 5.5 m, with a steady state temperature of 500°K.

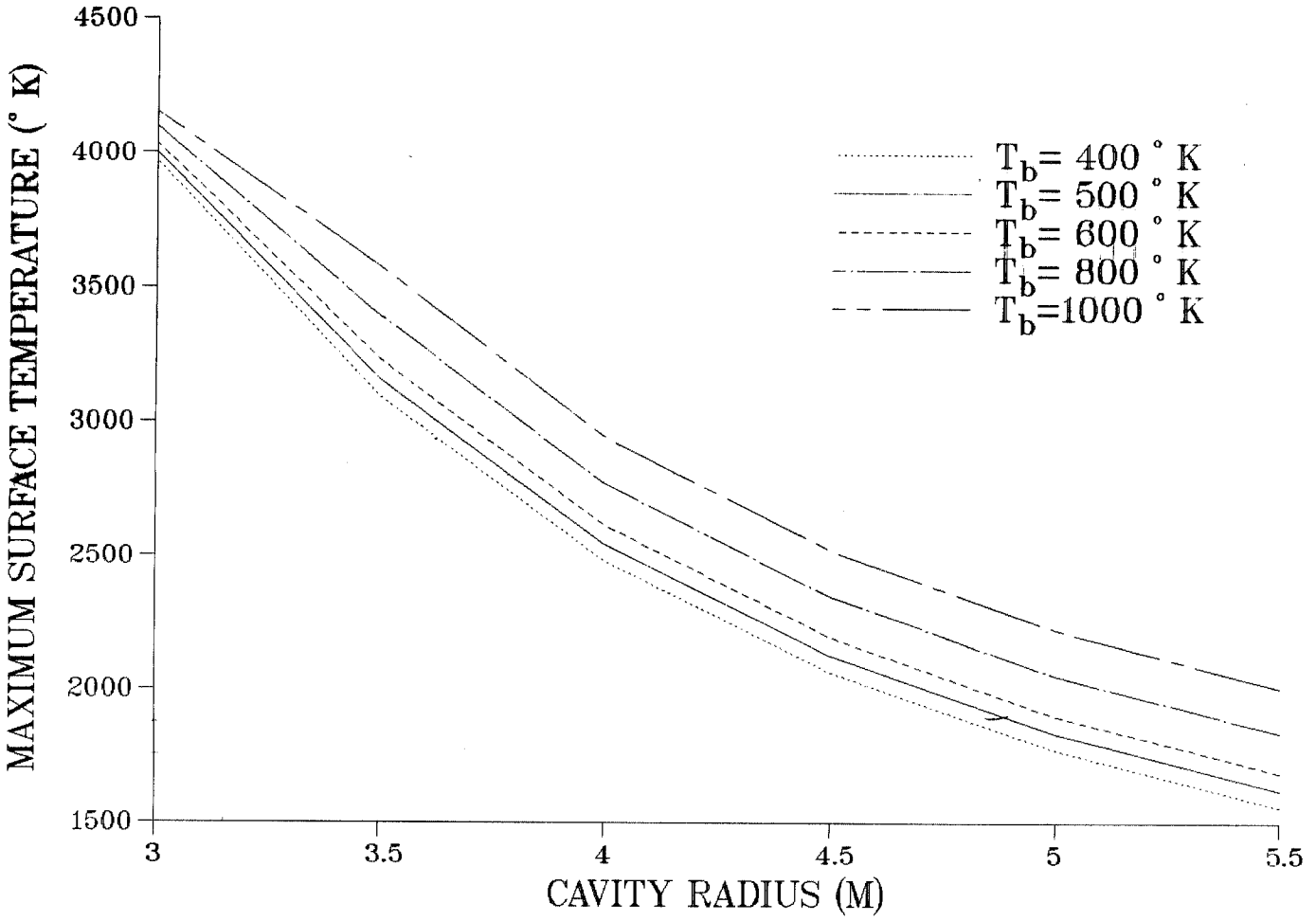

Fig. II.2.16. The maximum surface temperature for different steady state temperatures and cavity radii.

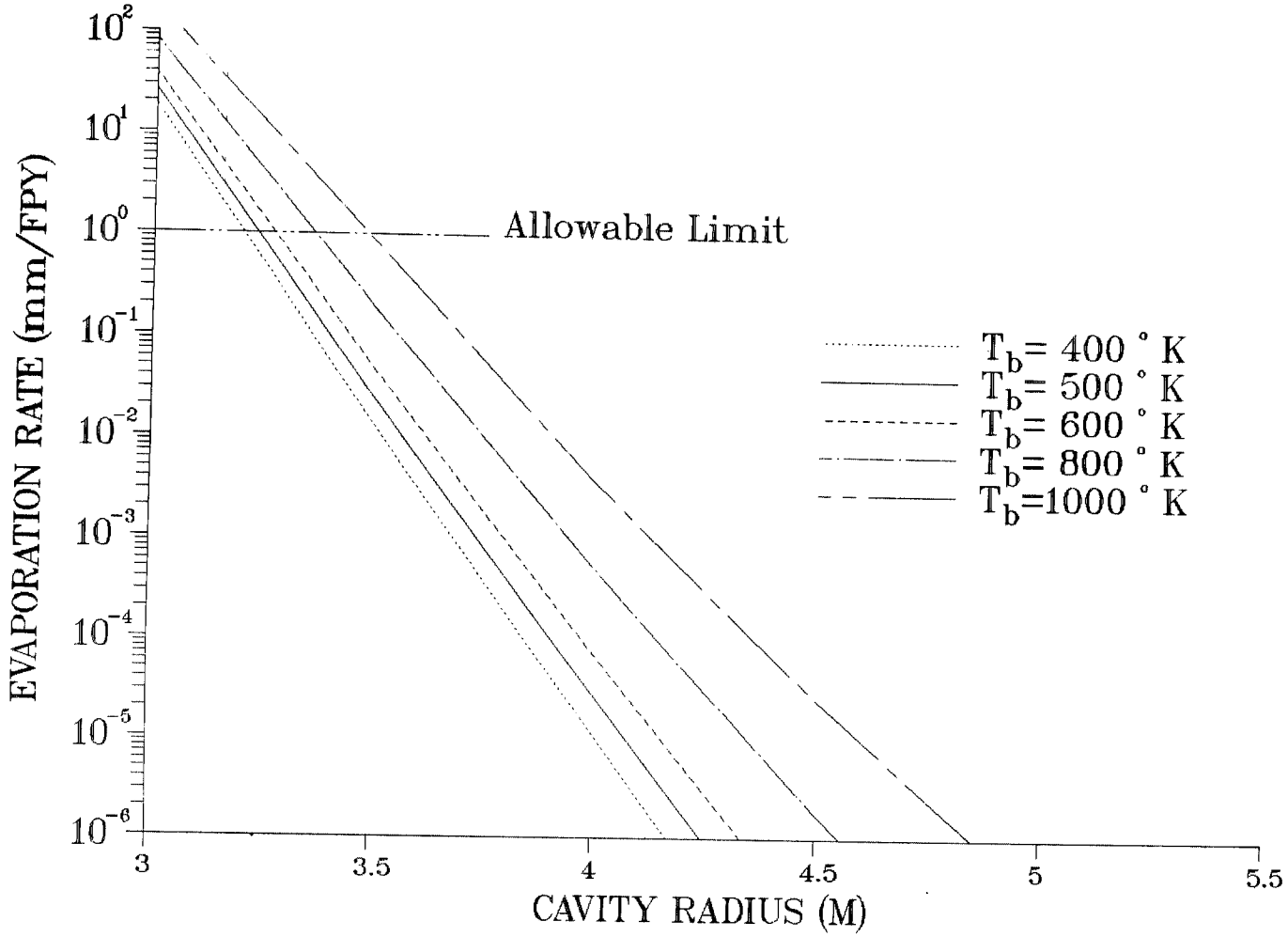

Fig. II.2.17. Evaporation rate as a function of the cavity radius and steady state surface temperature.

II.2.3 Gas Protection

A gas in the target chamber can protect the first wall from the damaging effects of target generated soft x-rays and target debris.[1-5] The energy would be absorbed in the gas and reradiated to the first wall over a much longer time period. We hope that the use of this gas will allow us a smaller cavity and, thus, a higher neutron loading in the materials test modules. The gas we have chosen is 1 torr of Xe, where the pressure is taken at 0°K. The density that this pressure corresponds to is assumed to not degrade the driver laser beams. We have performed calculations of the deposition of debris ions and x-rays in the gas, reradiation of the target energy from the gas, propagation of hydrodynamic shocks in the gas, and the thermal and mechanical response of the first wall to these loadings. We have found that gas protection can considerably reduce the thermal damage to the first wall, which allows us a smaller target chamber radius, i.e. a higher neutron wall loading.

II.2.3.1 Ion Energy Deposition in the Gas

Theoretical Basis. The interaction of pellet ion debris with materials occurs through electronic and nuclear energy loss.[6-8] Electronic energy loss is due to inelastic collisions between the debris ions and the electrons in the material. Nuclear energy loss is through elastic collisions between the ions and the nuclei in the material. The relative importance of these two mechanisms depends upon the instantaneous energy of the ion. The energy loss associated with each mechanism can be determined by specifying an appropriate interaction potential. These two mechanisms are briefly described below.

Electronic Energy Loss. Since the electronic energy loss depends on the energy of the incident ion, this mechanism is usually divided into three energy regimes, i.e. high, intermediate, and low energy regimes.

In the high energy regime, the velocity of the incident ion greatly exceeds the velocities of the orbital electrons. In this case, the ion acts as a point charge with a value equal to $Z_1 e$. The Bethe-Bloch[9] formula, which is a quantum mechanical derivation of the original classical result by Bohr,[10] is most commonly accepted and is expressed as

$$\frac{dE}{dx} = \frac{4\pi Z_1^2 e^4 N Z_2}{m_0 v^2} \ln \left(\frac{2m_0 v^2}{I}\right)$$

where: Z_1 = atomic number of incident ion

e = electron charge

N = atom density

Z_2 = atomic number of target atom

m_0 = electron mass

v = velocity of incident ion

I = mean ionization potential.

When the velocity of the incident ion is below the velocities of the orbital electrons, the ion is covered with an electron cloud that dynamically screens the ions over a distance of a few times the screening length of the static atoms. Therefore, the incident ion can be effectively considered as a neutral atom for the long range interaction with the target electrons. This energy loss can be modeled by the Lindhard (LSS)[11] or Firsov model. In these models, the energy loss of the incident ion is proportional to its velocity. The LSS model for the electronic energy loss is usually presented in a non-dimensional form as:

$$\frac{d\varepsilon}{d\rho} = k\varepsilon^{1/2}$$

where: $k = 0.0793 \dfrac{Z_1^{2/3} Z_2^{1/2} (1 + A)^{3/2}}{(Z_1^{2/3} + Z_2^{3/2})^{3/4} M_2^{1/2}}$

$$\varepsilon = \frac{E}{E_L}$$

$$\rho = \frac{R}{R_L}$$

$$E_L = \frac{(1 + A) Z_1 Z_2 e^2}{Aa} \text{ (ergs)}$$

$$R_L = \frac{(1 + A)^2}{4A\pi Na^2} \text{ (cm)}$$

$$a = 0.4683 \, (Z_1^{2/3} + Z_2^{2/3})^{-1/2} \, 10^{-8} \text{ (cm)}$$

$$A = \frac{M_2}{M_1} .$$

At the present time, there is no basic treatment for the intermediate energy regime which lies between the upper limit of LSS model and the lower limit of the Bethe-Bloch model. Fortunately, a comprehensive semi-phenomenological model based on three adjusted parameters determined from experiments has been proposed by Brice to predict the electronic energy loss for all three energy regimes. This model is derived from a modification of the Firsov model by giving a quantum mechanical treatment of the electron flux between adjacent interacting particles in terms of bound state wave functions. The result of this model is expressed as the electronic stopping power S(E) and is given by:

$$S(E) = N(Z_1 + Z_2) \, S_e(u) \, f(u) \qquad \text{(eV/cm)}$$

where: $S_e(u) = C\{u^{1/2}\left[\frac{30\ u^2 + 53\ u + 21}{3(1 + u)^2}\right] + (10\ u + 1)\ \arctan\ (u^{1/2})\}$

E = energy of incident ion (keV)

$C = 0.60961 \times 10^{-15}$ (eV-cm^2/atom)

$u = E/(\zeta^2 M_1 E_1)$

$f(u) = [1 + (4\zeta^2 a'^2 u)^{n/2}]^{-1}$

M_1 = particle mass (amu)

E_1 = 100 keV

ζ, a' and n = three adjustable parameters.

These three adjustable parameters can be determined from reliable experimental data or from semi-empirical values which are determined from the data in the three energy regimes. A tabulation of these three parameters for various ion-target combinations has been compiled in Ref. 12. In the SIRIUS-M study, the three adjustable parameters were determined from Ziegler and Chu[13] and a tabulation of stopping powers for different materials was made by Northcliffe and Schilling.[14] In addition, a tabulation of stopping powers and range data for different materials has recently been completed by Ziegler and Anderson.[15]

Nuclear Energy Loss. In the nuclear energy loss process, the rate of interaction depends on the nuclear cross sections. Theoretical values for nuclear cross sections are determined by the interatomic potential between the nuclei and the particle. The most widely accepted model for this energy loss process is the nuclear cross sections derived by Lindhard[11] using a shielded Coulomb interaction potential with a Thomas-Fermi atomic model. An approximation for a non-dimensional nuclear cross section is given by Oen and Robinson:[16]

$$\frac{d\varepsilon}{d\rho} = \frac{9}{8\varepsilon}\{\ln [u + (1 + u^2)^{1/2}] - u(1 + u^2)^{-1/2}\}$$

where: $\varepsilon = \frac{E}{E_L}$

$\rho = \frac{R}{R_L}$

$u = (2\lambda)^{1/3} \varepsilon^{4/9}$

$\lambda = 1.309.$

A qualitative comparison between nuclear energy loss and electronic energy loss can be seen in Fig. II.2.18 for the case of helium in carbon. It is obvious that the nuclear energy loss is negligible compared with electronic energy loss for the incident energies even down to the energy regime of about hundreds of keV.

Computational Methods. The ion implantation range and energy deposition BRICE[17] code was used to perform the ion energy loss calculations for SIRIUS-M. Information on H, D, T, He, and C ions was obtained. The BRICE model was used in the calculation of the energy losses of H, D, T, and He ions. The LSS model was used to model the energy loss of C ion debris.

Target calculations described in the SIRIUS report[19] have determined the velocities of the ions after explosion. The numbers of ions emitted from the target have been scaled to give the proper target yield. A list of the energies and number of ions for the base case as well as two other targets with a higher CH_2 mass is given in Table II.2.2. The buffer gas in the SIRIUS-M reactor cavity is Xe at 1 torr, a density that was chosen so that the longest stopping length of a target debris ion is 2 meters. In addition to energy deposition density, the temperature rise of the reactor cavity was used

Table II.2.2. Energies and Number of Particles of Ion Debris for Different Cases

	Case 1*		Case 2		Case 3	
Ion	Energy[A]	Number of Particles	Energy	Number of Particles	Energy	Number of Particles
H	137.5	1.31 +19[B]	103.35	1.87 +19	68.9	2.8 +19
D	92.5	1.21 +19	93.9	1.3 +19	93.9	1.3 +19
T	139.0	1.21 +19	140.8	1.3 +19	140.8	1.3 +19
He	185.0	4.67 +18	187.7	5.0 +18	187.7	5.0 +18
C	1649.0	6.54 +18	1237.5	9.33 +18	825.0	1.4 +19

*Base Case. A. The unit is keV. B. Read as 1.4×10^{19}.

to modify the energy deposition of ions in Xe gas. Use of the MIXERG[18] computer code provided equation-of-state information to calculate the temperature rise in the target chamber gas due to ion energy deposition. The conversion curve is shown in Fig. II.2.19.

Results and Conclusions. Figure II.2.20 shows the calculation result for the ion implantation range of different ions as a function of their energy in xenon gas. The relationship between ion implantation range and its energy is approximately linear. The total energy deposition profile (electronic plus nuclear energy loss) of each ion in xenon gas is presented in Fig. II.2.21. Since the longest range amongst the ions in the base target is that of 1.65

MeV carbon which was originally in the form of CH_2,[19] it was felt necessary to study how the gas temperature and energy deposition density depend on the ion energy and number of ions per shot. Three combinations of ion energies and numbers of ions are suggested where the total amount of energy in the ions coming from the CH_2 is preserved. The first combination is the basic reference case previously described. The second case divides energies of H and C ions by 2, and multiplies the number of H and C ions by 2. Similarly, in case 3, the energies of H and C ions are 3/4 of the base case energies and the numbers of H and C ions are appropriately scaled. The three cases are listed in Table II.2.2. The quantitative calculation of the response of each case can be seen in Fig. II.2.22. Furthermore, the temperature rise due to energy deposition of ions (including the 0.1 eV initial temperature of xenon gas) in the reactor cavity is shown in Fig. II.2.23. In Fig. II.2.21, the energy deposition profile drops rapidly to a very small value within the first 25 cm for all three cases. This phenomenon is also true for the temperature profile in Fig. II.2.23. Therefore, the energies of ions are greatly attenuated before bombarding the first wall. Furthermore, from numerical data listed in Table II.2.3, it is clear that the temperature rise drops about 3 orders of magnitude between radius 5 cm and 200 cm. Hence, we conclude that the debris ions can be contained in a 2 meter radius cavity filled with 1 torr of xenon gas for all three cases.

From the above analysis, we can conclude that the radius of the reactor cavity will be approximately 1.8 and 1.5 meters for cases 2 and 3 respectively if the gas temperature rise at the edge of the reactor cavity is to be the same as that for the base case. Since the exact design of the target is still

Table II.2.3. Temperature Rises of Xe Gas for Three Cases

	Temperature Rise (eV)		
Depth (cm)	Case 1	Case 2	Case 3
5	195.523	238.866	245.604
10	58.182	62.739	70.343
20	21.147	22.425	24.865
30	12.527	14.032	15.580
40	5.912	6.403	6.441
50	4.259	4.298	4.345
60	3.130	3.042	3.317
70	2.259	2.224	2.614
80	1.687	1.742	2.055
90	1.362	1.458	1.655
100	1.169	1.275	1.354
120	0.956	1.027	0.944
140	0.852	0.865	0.655
150	0.790	0.768	0.549
180	0.631	0.533	0.272
200	0.534	0.427	0.136

unknown, it is felt that the variations of the number of C and H particles in cases 1-3 are reasonable. Future target design should take this into account.

II.2.3.2 Gas Response

The target generated x-ray and ion energy deposited in the target chamber gas heats the gas to the point that it radiates some of that energy to the wall. Parametric calculations, presented in the next section, have shown that the first wall temperature response is sensitive to the time that this energy is radiated to the wall. Most of the energy is deposited near the location of the target explosion so that a large temperature gradient is generated, which implies a steep pressure profile that will launch potentially damaging shock waves. The MFFIRE computer code[20] models both of these effects.

MFFIRE is a Lagrangian hydrodynamics multigroup radiative heat transfer finite difference computer code. It uses equations of state and opacities obtained from tables that have been created by the computer code MIXERG.[18] MFFIRE calculates the deposition of x-rays from the conditions in the gas and the x-ray spectrum, shown for this study in Fig. II.2.24. There is approximately 0.8 MJ in this spectrum; MFFIRE predicts that about 60% of these x-rays would be absorbed in 2 meters of 1 torr Xe. The spectrum of x-rays leaving the gas is also shown in Fig. II.2.24, where one sees that a large fraction of the photons with energies greater than 3 keV are not stopped while there is almost no transmission of those with energies less than 2 keV. This deposition calculation includes the bleaching effect that increases the stopping length of the x-rays due to depletion of the tightly-bound electrons in the gas atoms near the target explosion. The energy deposition from x-rays is in addition to the energy density profile due to the debris ions described in the previous section. We assume, in MFFIRE, that the x-ray and ion energy is

deposited over a time short compared to the time scales for radiative heat transfer and hydromotion in the gas so that the energy density from deposition is treated as an initial condition. The gas is then allowed to radiate and hydrodynamically move as it will. Radiative heat transfer is modeled within a 20 group flux-limited diffusion approximation, where the group opacities are provided by MIXERG. The code provides the radiative heat flux and the shock pressure on the first wall as functions of time.

The results of a simulation of the behavior of the target chamber gas in the SIRIUS-M reactor are shown in Figs. II.2.25 through II.2.28. The simulation is for a 1 torr gas in a 2 meter radius cavity, where the initial temperature profile corresponds to energy deposited from a 13.4 MJ target explosion. One sees in Fig. II.2.25 the diffusion of the gas temperature through the target chamber gas to the wall, beginning with the initial profile. The temperature profile at 3.1 μs is close to reaching the first wall. Figure II.2.26 shows the heat flux at the first wall as a function of time and Fig. II.2.27 shows the integrated radiation flux on the wall. From Fig. II.2.27 one sees that at 3 μs, most of the radiation has yet to occur. The pressure at the first wall is given in Fig. II.2.28. The maximum pressure is only 0.14 atmospheres, which calculations discussed in Section II.3 show is probably low enough to not cause any damage to the first wall tiles.

II.2.3.3 Wall Thermal Response

We have studied the response of the graphite tile first wall in SIRIUS-M to the pulsed thermal loadings in the presence of a protecting region of Xe gas. Since one purpose of the protecting gas is to spread out the thermal pulse on the wall, we have parametrically studied the sensitivity to the thermal pulse width of the maximum temperature seen in the wall. We have also

calculated the temperature of the graphite wall where the thermal loadings are our best estimates of the heat fluxes due to reradiated energy from the gas, laser light reflected and refracted off of the target, and x-ray and ions that have penetrated the gas. We have used standard finite difference temperature diffusion computer methods for both the parametric and base case calculations.

Two sets of parametric calculations, one for square and the other for exponential heat pulses, have been carried out. These are depicted in Figs. II.2.29 and II.2.30, respectively. In both sets of calculations, the total radiated energy density is 7.2 J/cm^2, the temperature of the back of the tile is 500°K, and the thickness of the graphite tile is 1 cm. The reader will note that there is a discrepancy between the 7.2 J/cm^2 used here and the actual reradiated energy density in Fig. II.2.27 of 3.5 J/cm^2. This difference occurs because for the parametric calculations we assumed that the total x-ray and ion energy from the target, about 3.5 MJ, is reradiated within the specified reradiation pulse width, while in fact about half of this remains in the gas for a long time. We expect that the total 3.5 MJ would be radiated by the next shot, which occurs 100 ms later, but we have not carried the simulations discussed in Section II.2.3.2 out that long. The results shown in Figs. II.2.29 and II.2.30 demonstrate the great sensitivity of the surface temperature to the time over which the heat flux is incident on the surface. For both the exponential and square pulse cases, one sees that as the characteristic pulse time changes from 10 microseconds to 100 microseconds, the maximum surface temperature rise decreases by as much a factor of four. From Fig. II.2.27, one sees that about 1 J/cm^2 is radiated by 100 ms so that we should see great reductions in the maximum surface temperature due to this effect.

To calculate the thermal response of the graphite tiles for the base case of SIRIUS-M we must include all of the contributions to the heat flux. As we have just discussed, the reradiated energy is spread over a long enough time to reduce the surface temperature rise considerably. The reflected laser light is, however, deposited over an extremely short time and may be the major source of thermal damage. This was unexpected because there is less energy in reflected light than in the reradiated light. The total heat incident power on the first wall is shown in Fig. II.2.31. Plotted in Fig. II.2.32 is the surface temperature rise for the SIRIUS-M base case; when the steady state temperature is added to these results the maximum surface temperature is 1666°K. Based on this surface temperature history, the rate that material is evaporated off of the wall is 5.23×10^{-15} mm per full power year. This is low enough to not be important. Thermal stresses may still be a concern, though, because the temperature profile in the graphite is rather steep. An isothermal mapping of the temperature in the first wall is shown in Fig. II.2.33. This issue is discussed further in Section II.3.

References for Section II.2.3

1. J.J. Duderstadt and G.A. Moses, Inertial Confinement Fusion, (1982).

2. G.A. Moses and R.R. Peterson, "First Wall Protection in ICF Reactors by Inert Cavity Gases," University of Wisconsin Fusion Technology Institute Report UWFDM-323 (October 1979).

3. S.I. Abdel-Khalik, G.A. Moses and R.R. Peterson, "Inertial Confinement Fusion Reactors Based on the Gas Protection Concept," University of Wisconsin Fusion Technology Institute Report UWFDM-341 (January 1980).

4. T.O. Hunter and G.L. Kulcinski, "Surface Damage and Thermal Effects from Transient Pulsed Thermonuclear Radiation in Inertial Fusion Reactors," Journal of Nuclear Materials 76, 383-388 (1978).

5. T.J. McCarville, G.A. Moses and G.L. Kulcinski, "A Model for Depositing Inertial Confinement Fusion X-Rays and Pellet Debris into a Cavity Gas," University of Wisconsin Fusion Technology Institute Report UWFDM-406 (April 1981).

6. T.O. Hunter, "A General Model for the Analysis of the Transient Radiation Damage Environment from Pulsed Thermonuclear Radiation," University of Wisconsin-Madison, (July 1978).

7. H.M. Attaya, "The Effect of Microstructure on the Spatial Distribution of the Damage Produced by the Ions in Solids," University of Wisconsin Fusion Technology Institute Report UWFDM-420 (May 1981).

8. A.M. Hassanein, "Thermal Effects and Erosion Rates Resulting from Intense Deposition of Energy in Fusion Reactor First Walls," University of Wisconsin Fusion Technology Institute Report UWFDM-465 (April 1982).

9. L.T. Chadderton, Radiation Damage in Crystals, John Wiley and Sons, Inc., New York.

10. N. Bohr, Mat. Fys. Medd. Dan. Vid. Selsk. 18(8), (1948).

11. J. Lindhard et al., "Range Concepts and Heavy Ion Ranges," Mat. Fys. Medd. Dan. Vid. Selsk. 33(14), 3 (1963).

12. D.K. Brice, Ion Implantation Range and Energy Deposition Distribution, Vol. 1, IFI/Plenum, New York, 1975.

13. J.F. Ziegler and W.K. Chu, "The Stopping of ^{4}He Ions in Elemental Matter," Thin Solid Films 19, 281-287 (1973).

14. L.C. Northcliffe and R.F. Schilling, "Range and Stopping-Power Tables for Heavy Ions," Nuclear Data Sec. 7(3-4), (1970).

15. J.F. Ziegler and H.H. Anderson, The Stopping and Ranges of Ions in Matter, Vol. 1-5, Pergamon Press, New York (1977).

16. O.S. Oen and M.T. Robinson, "Slowing-Down Time of Energetic Ions in Solids," Journal of Applied Physics 46(12), 5069 (December 1975).

17. D.K. Brice, "Three-Parameter Formula for the Electronic Stopping Cross Section at Non-Relativistic Velocities," Physical Review A6(5), 1791 (Nov. 1972).

18. R.R. Peterson and G.A. Moses, "MIXERG - An Equation of State and Opacity Computer Code," Computer Physics Communications 28, 367 (1983).

19. B. Badger et al., "Preliminary Conceptual Design of SIRIUS, A Symmetric Illumination, Direct Drive Laser Fusion Reactor," University of Wisconsin Fusion Technology Institute Report UWFDM-568 (March 1984).

20. G.A. Moses, T.J. McCarville and R. R. Peterson, "Documentation for MFFIRE, A Multifrequency Radiative Heat Transfer Version of FIRE," University of Wisconsin Fusion Technology Institute Report UWFDM-458 (August 1984).

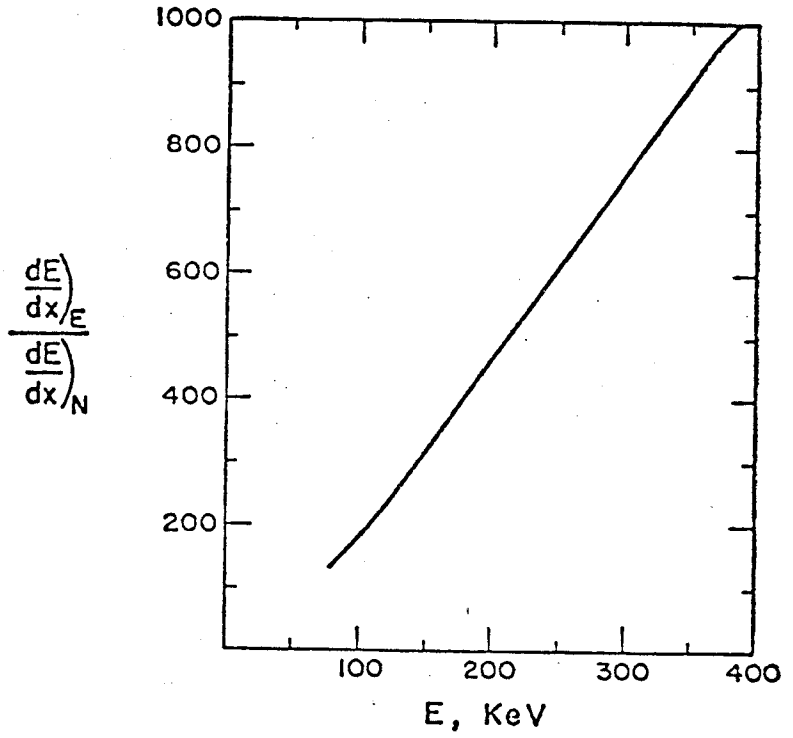

Fig. II.2.18. Ratio of electronic and nuclear energy loss for He in C.

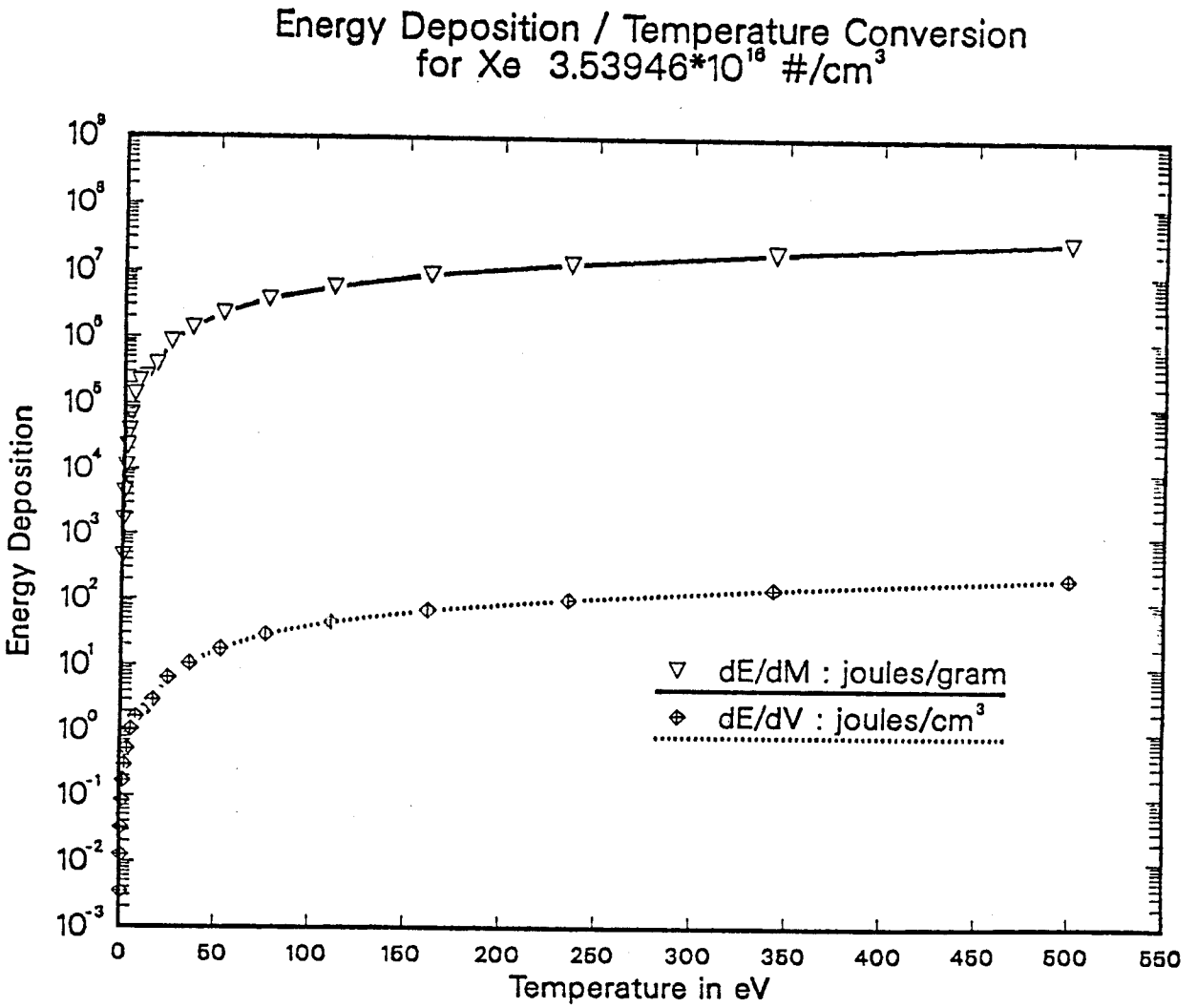

Fig. II.2.19. Energy deposition density versus temperature rise conversion curve results are for SIRIUS-M reference target spectrum.

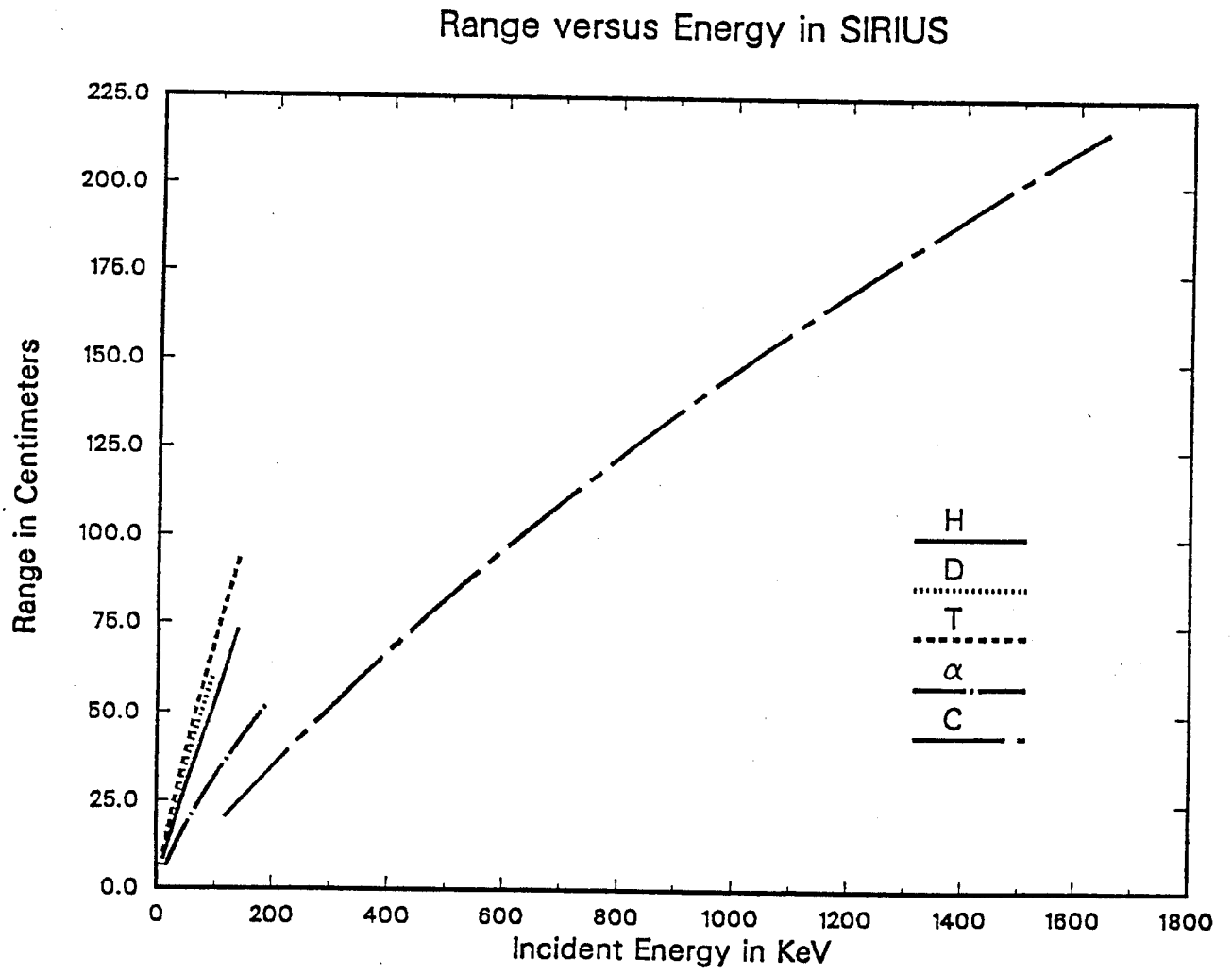

Fig. II.2.20. Range of H, D, T, He, and C in 1 torr, 273°K Xe gas.

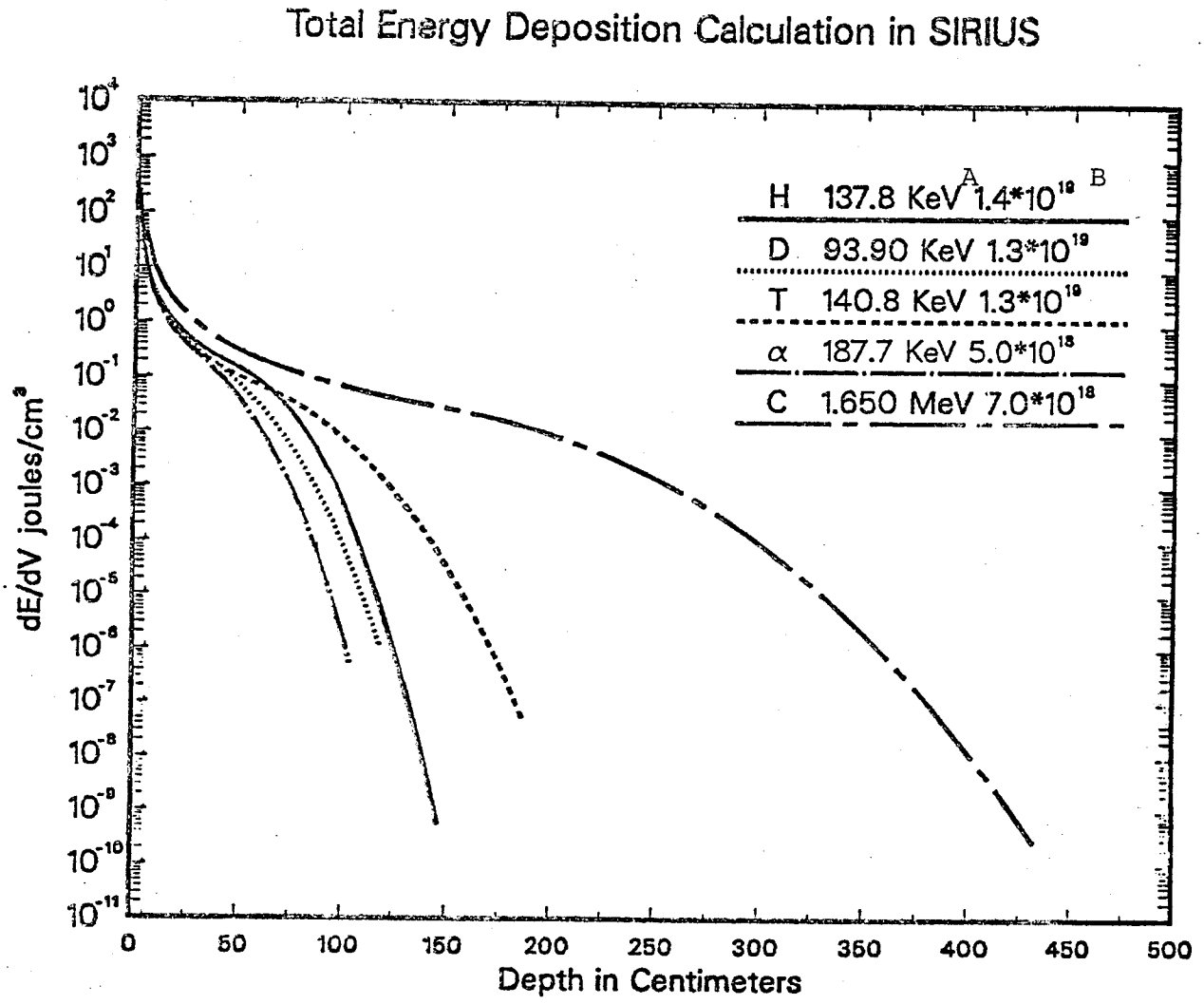

A. Ion Energy.

B. Number of ion particles.

Fig. II.2.21. Energy deposition density of ion in Xe gas.

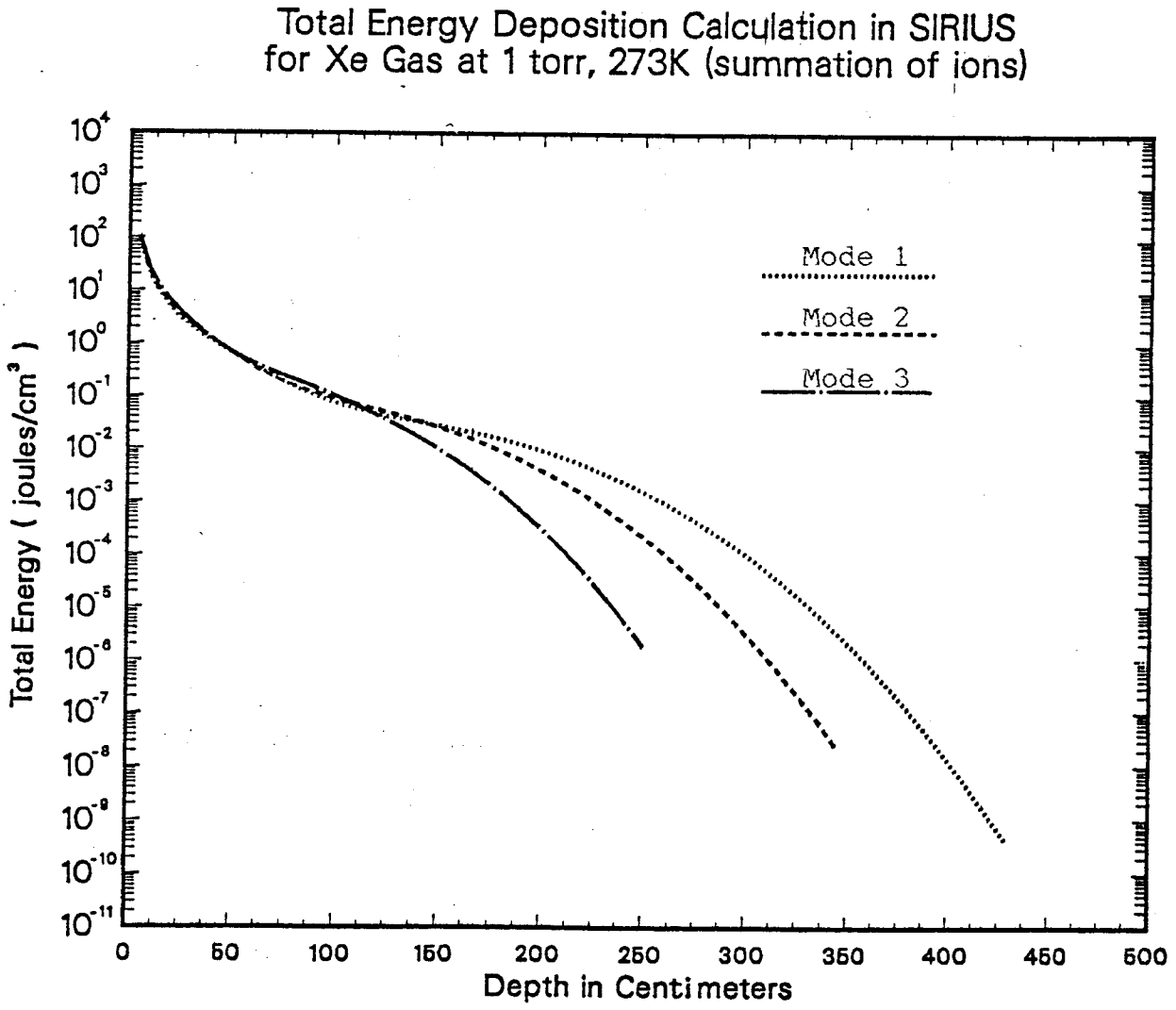

Fig. II.2.22. Total energy deposition density of ions in Xe gas.

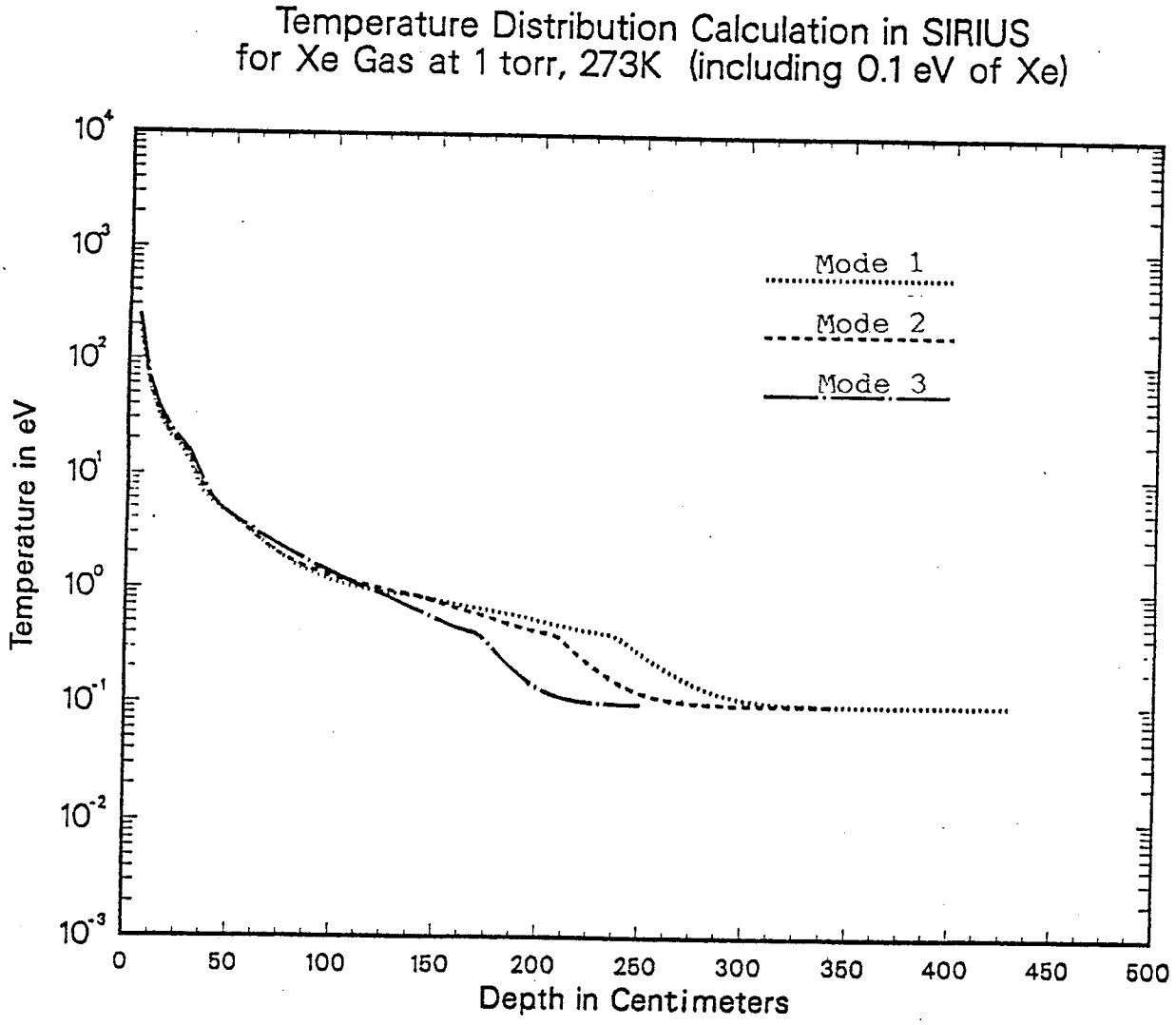

Fig. II.2.23. Temperature rise in Xe gas due to energy deposition of ions.

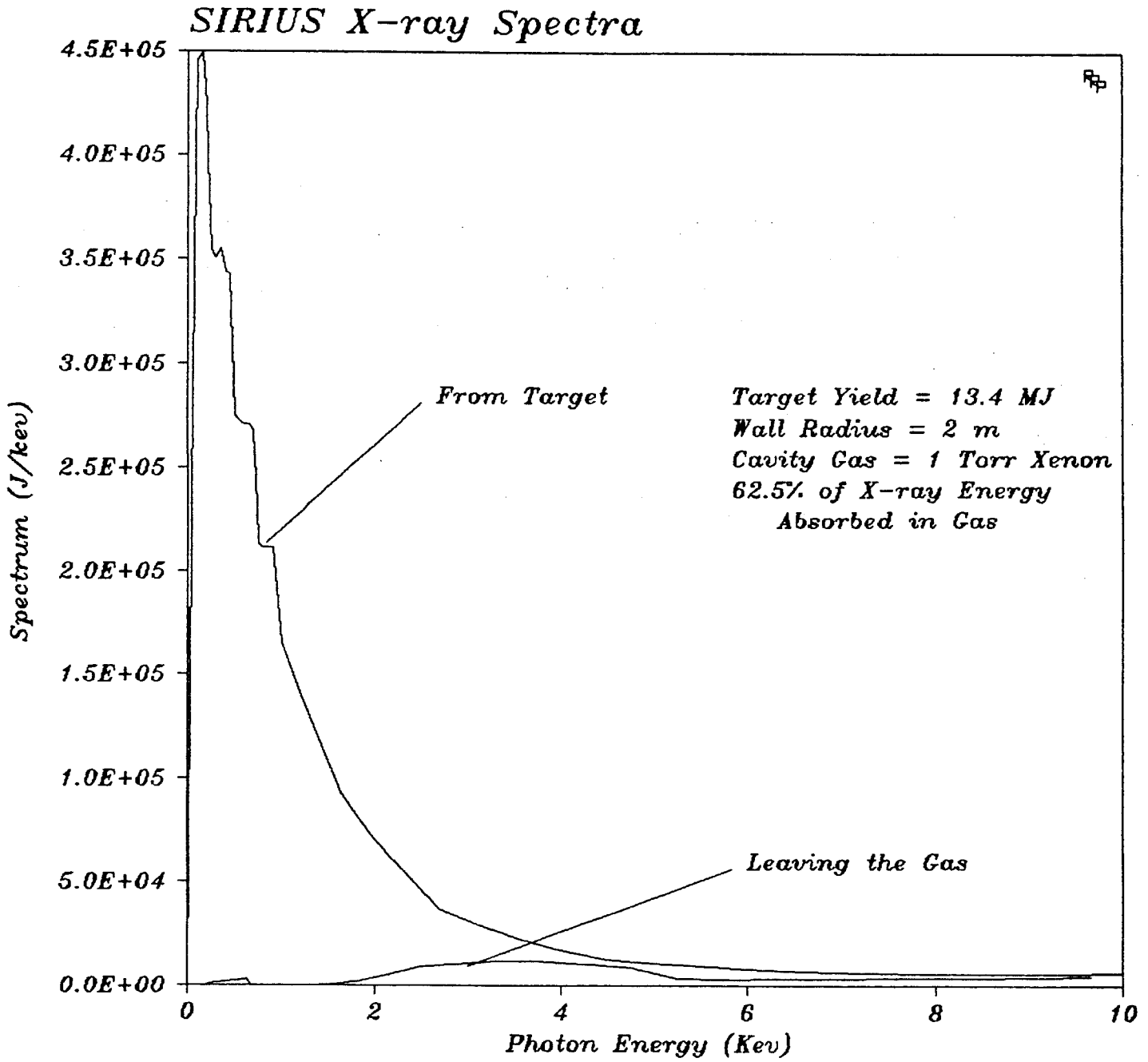

Fig. II.2.24. Target x-ray spectrum.

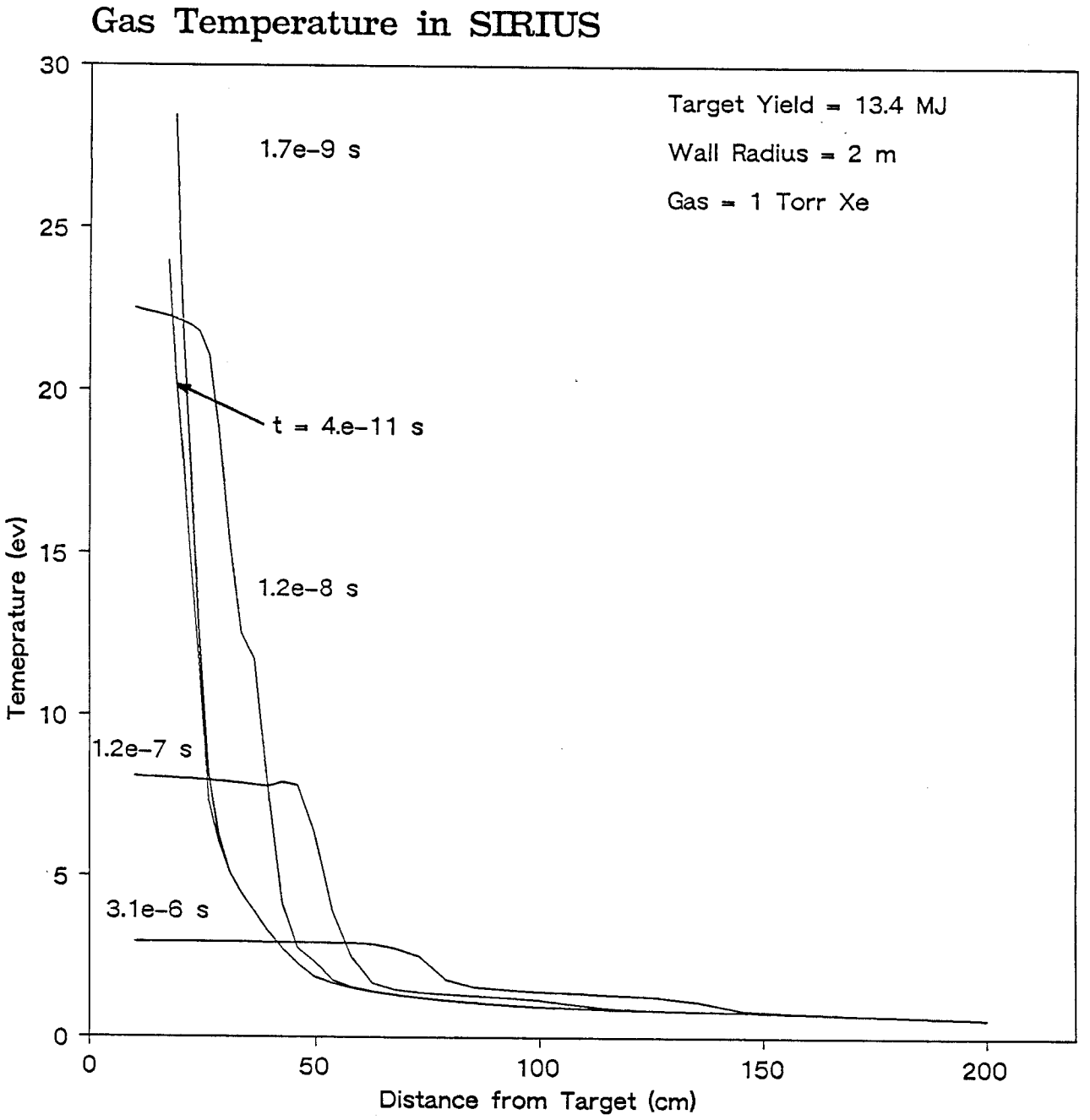

Fig. II.2.25. Gas temperature profiles in the SIRIUS-M target chamber gas for various times.

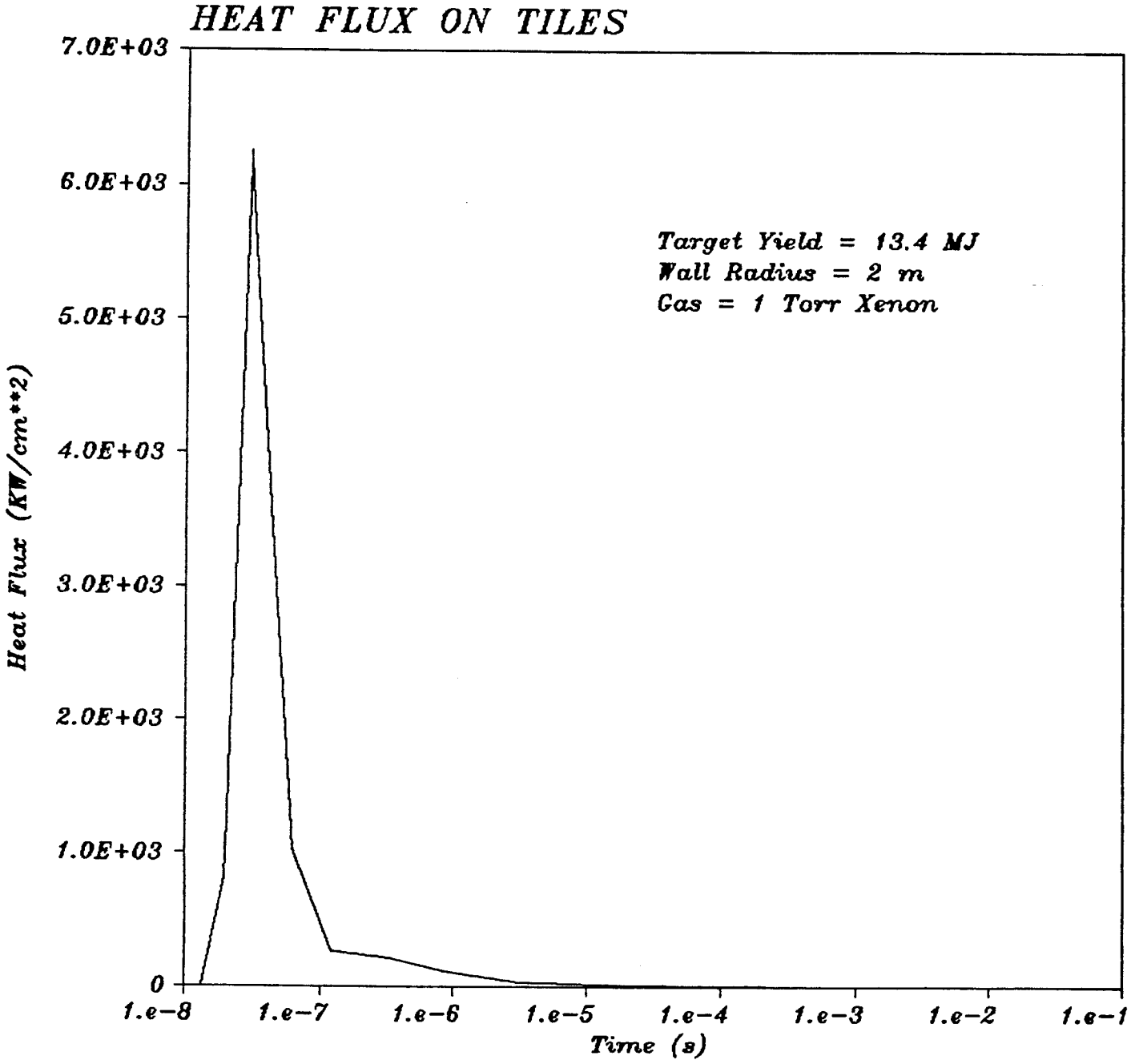

Fig. II.2.26. Radiation heat flux on the first wall of the SIRIUS-M target chamber.

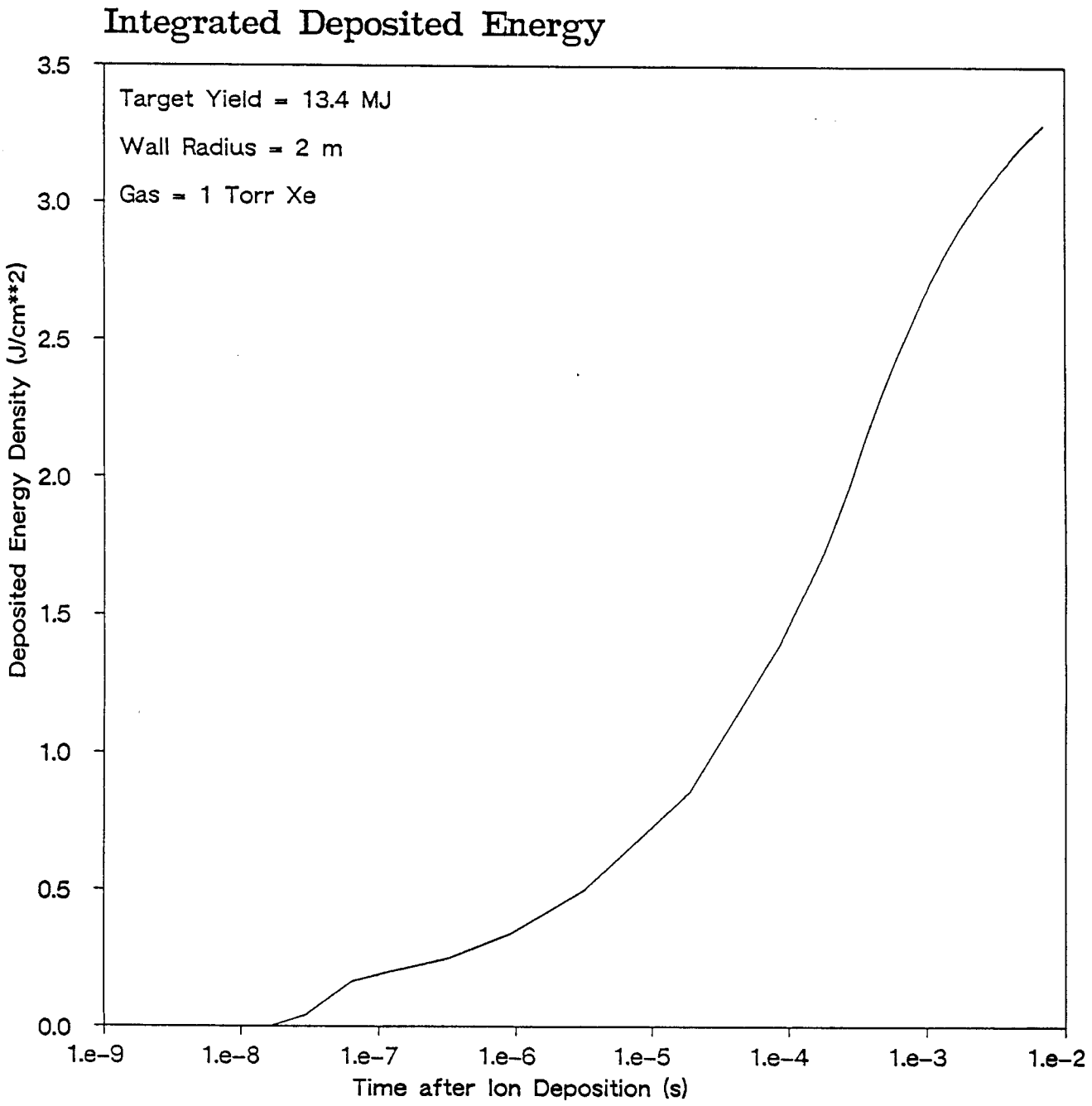

Fig. II.2.27. Integrated radiation heat flux on first wall of the SIRIUS-M target chamber.

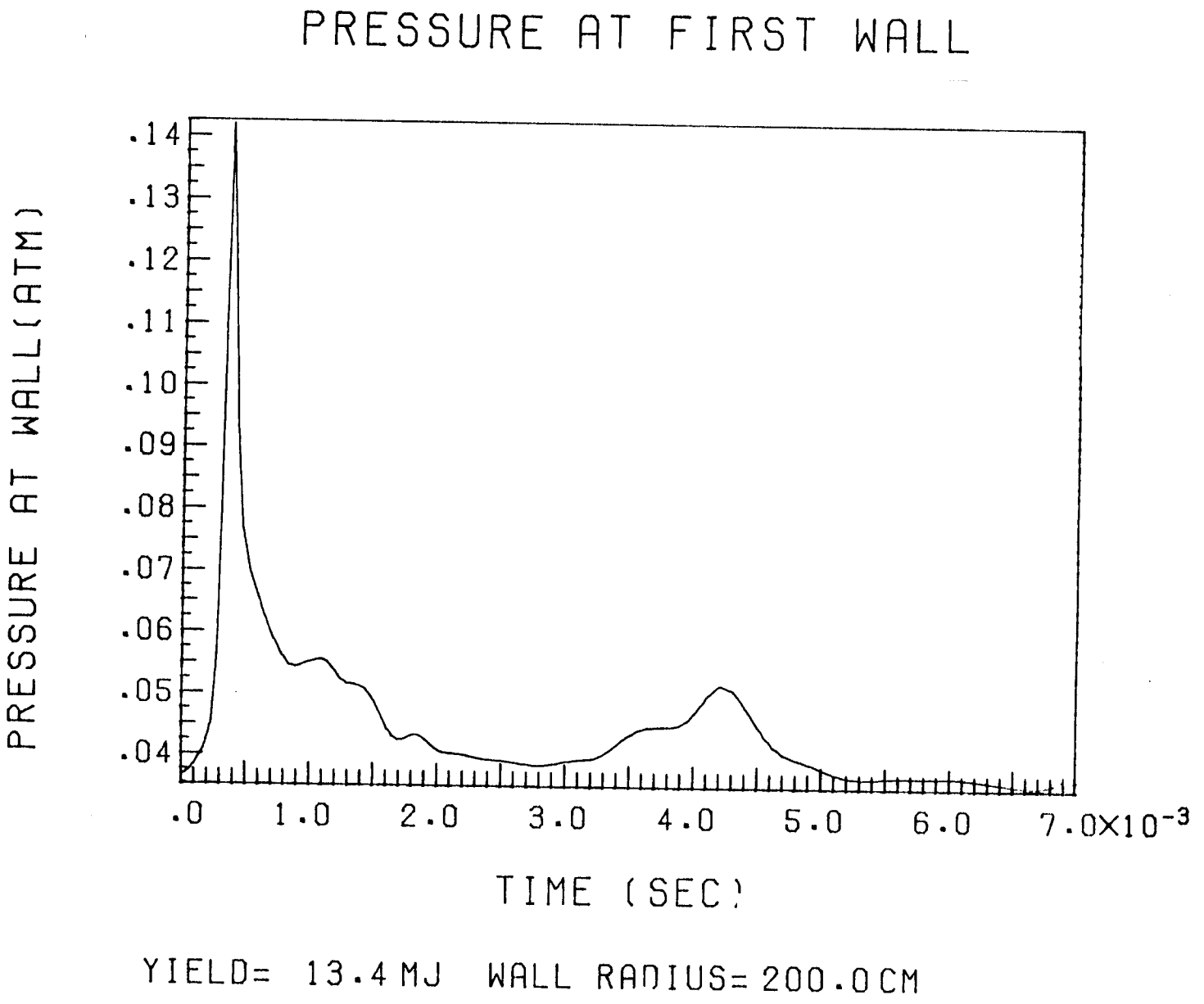

Fig. II.2.28. Shock overpressure on SIRIUS-M target chamber first wall.

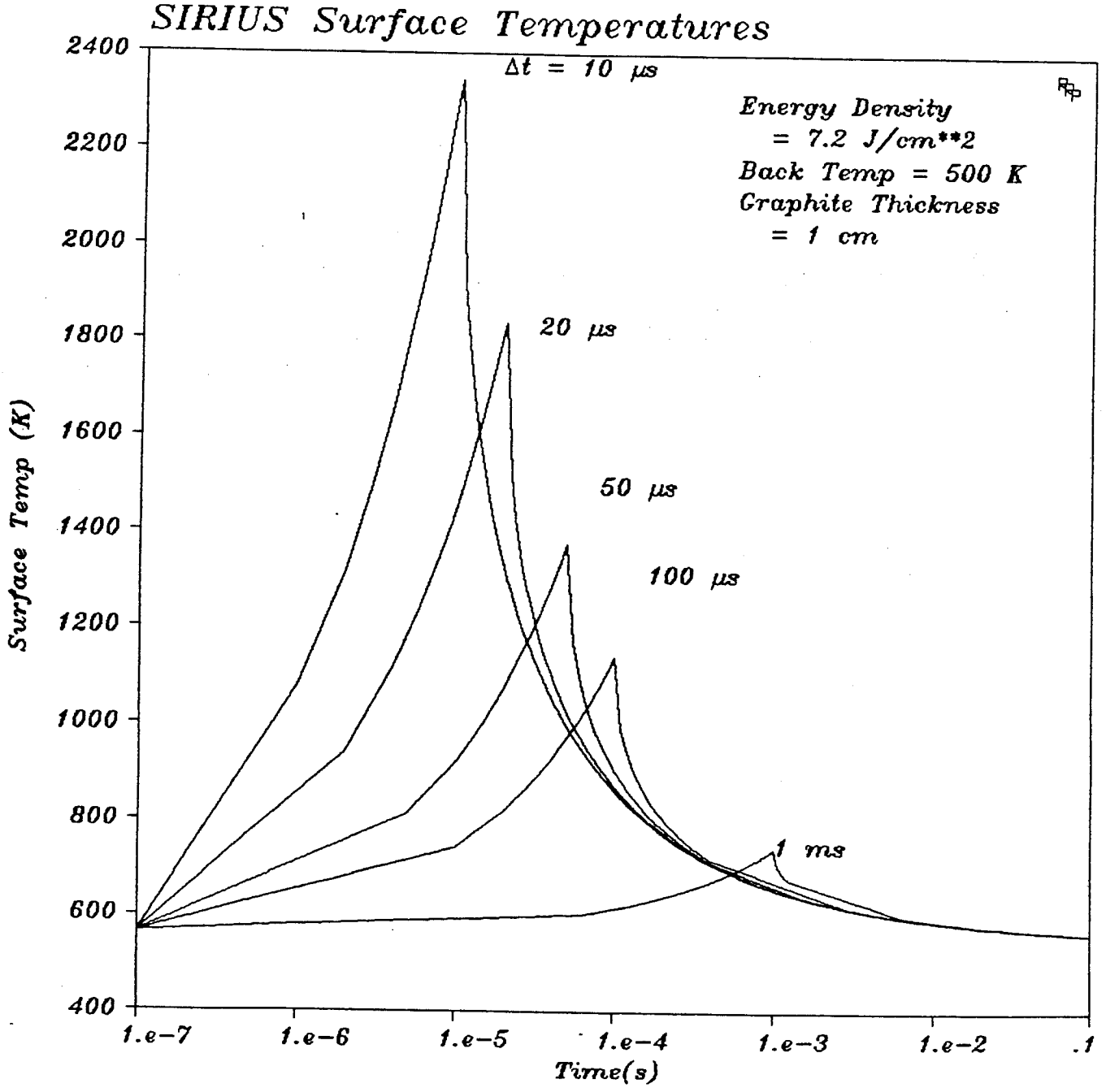

Fig. II.2.29. Surface temperatures in graphite tiles for square thermal pulses with parametrically varied pulse widths.

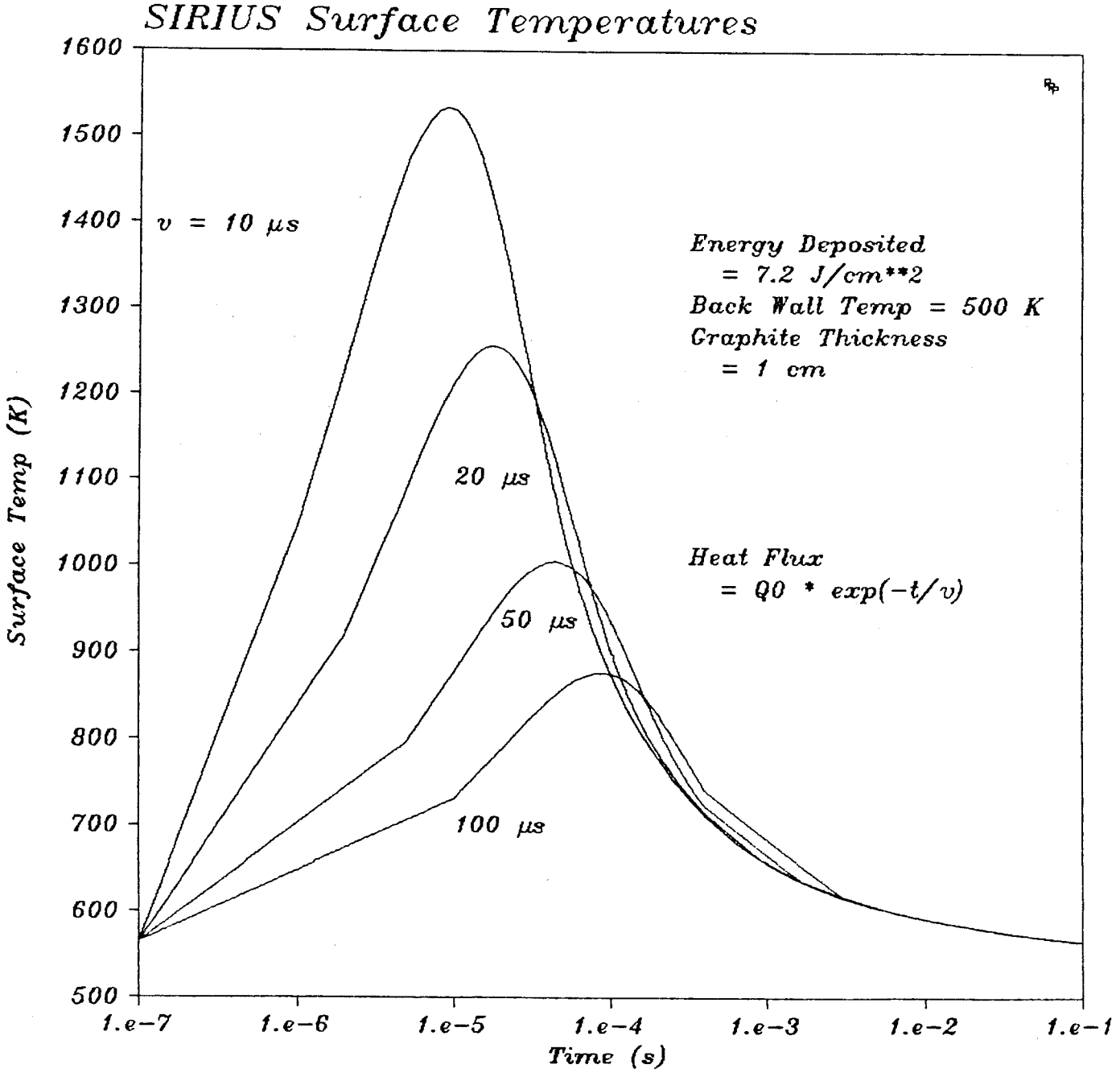

Fig. II.2.30. Surface temperatures in graphite tiles for exponential thermal pulses with parametrically varied decay times.

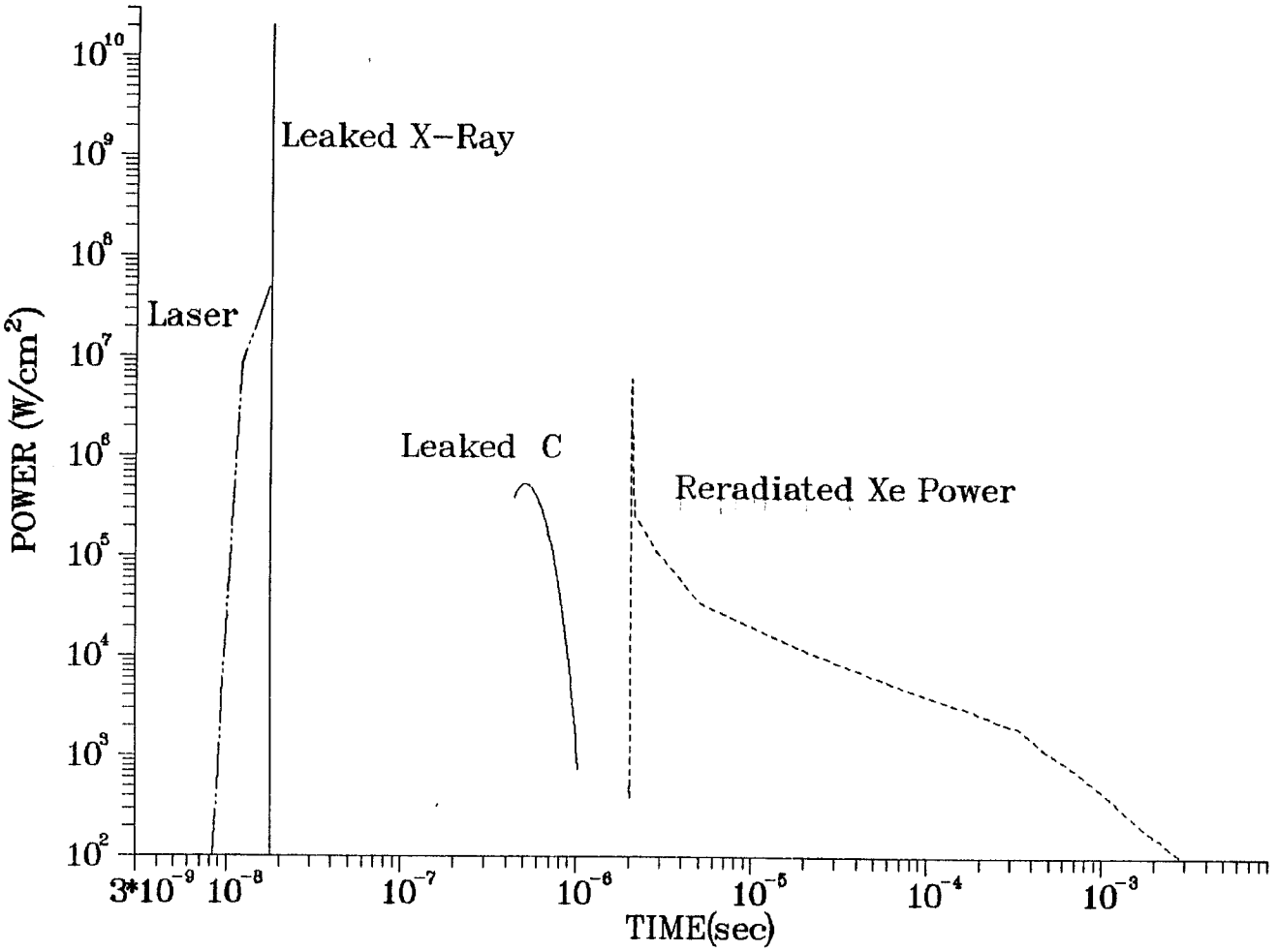

Fig. II.2.31. Total heat flux on first wall including reflected laser, re-radiated, and unabsorbed target x-rays and ions for base case.

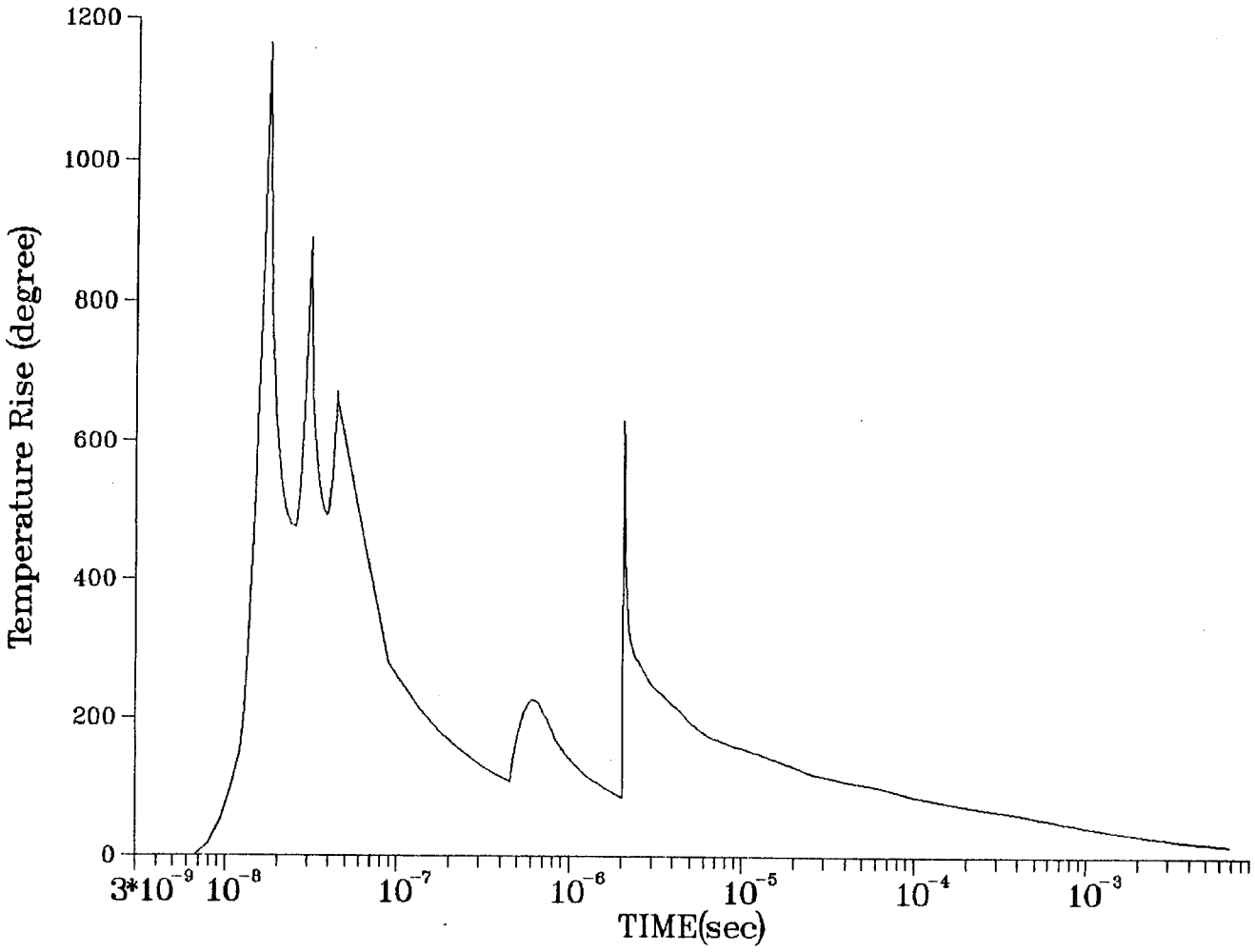

Fig. II.2.32. Temperature rise in graphite tiles in SIRIUS-M for base case.

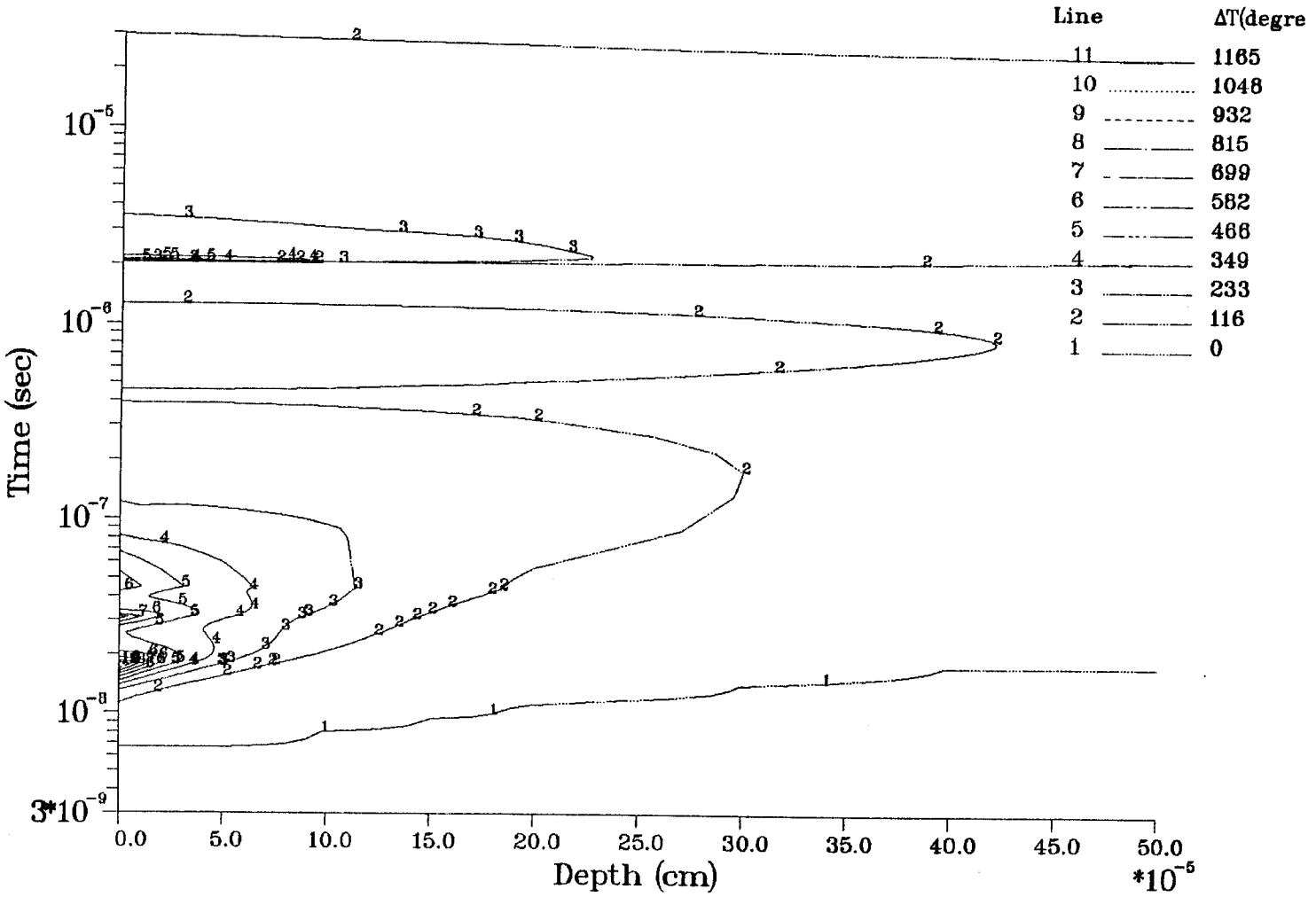

Fig. II.2.33. Isotherms in graphite tiles for SIRIUS-M base case.

II.3 Stress Analysis of First Wall

II.3.1 Mechanical Stress

The chamber gas will transmit a shock pressure to the first wall after each microexplosion. The resulting dynamic stresses have been determined for the case in which the structure is represented by a thin spherical shell of H-451 graphite. This implies mechanical continuity between tiles and ignores outer structure support. For a radius of 2 m and thickness of 1.0 cm, the natural frequency and vibration period for symmetric motion are 261 Hz and 3.83 ms, respectively. These values indicate that mechanical resonance associated with driver synchronization will not be an issue and that the shock pulse width is comparatively very small, i.e. an impulsive pressure. The response is shown in Fig. II.3.1 for an impulse of 4.80 Pa-s, and a conservative dissipation level of 2% critical damping. The peak tensile stress is 1.52 MPa, which is only 10.6% of the tensile strength, 14.38 MPa, at 500°K.[1]

II.3.2 Thermal Stresses

Energy deposition in the first wall will develop an intense compressive thermal stress distribution at the inner surface. Since the heated layer is comparatively very thin it will be almost totally constrained by the unaffected graphite. The general results of this in Fig. II.3.2 show the increase in thermal stress and strength with surface temperature for an outer surface temperature of 500°K. The compressive strength is reached at 1800°K, i.e. an increase of 1300°K.

The first surface thermal stress history is shown in Fig. II.3.3. The maximum value is 61.37 MPa occurring at 17.7 ns. This represents 87.6% of the compressive strength (70.06 MPa). The stress profile in the first wall corre-

sponding to the peak surface stress appears in Fig. II.3.4 and characterizes the high gradient from energy deposition.

In summary, the preceding results have shown that the maximum dynamic mechanical stresses from the cavity gas pressure pulse are quite small for a design in which the chamber responds as a spherical shell. If the first wall tiles are free, as individual plates, such stresses may be larger. In contrast, the design will be influenced by thermal stress. For the base design the values are within strength limits but the margin is small.

Peak thermal stresses have also been determined for unprotected graphite cavity walls. Maximum surface temperatures depend strongly upon cavity size and steady state wall temperature and from this, such stresses are found with limits established as values which equal the compressive strength of graphite. The temperature-dependence of mechanical properties and strength were used in obtaining the results shown in Fig. II.3.5. It can be seen that the limit line spans a moderate range of steady state temperatures but the cavity radius is restricted to approximately 5 meters.

References for Section II.3

1. G.R. Hopkins et al., "Carbon and Silicon Carbide as First Wall Materials in Inertial Confinement Fusion Reactors," General Atomic Report GA-A14894, March, 1978.

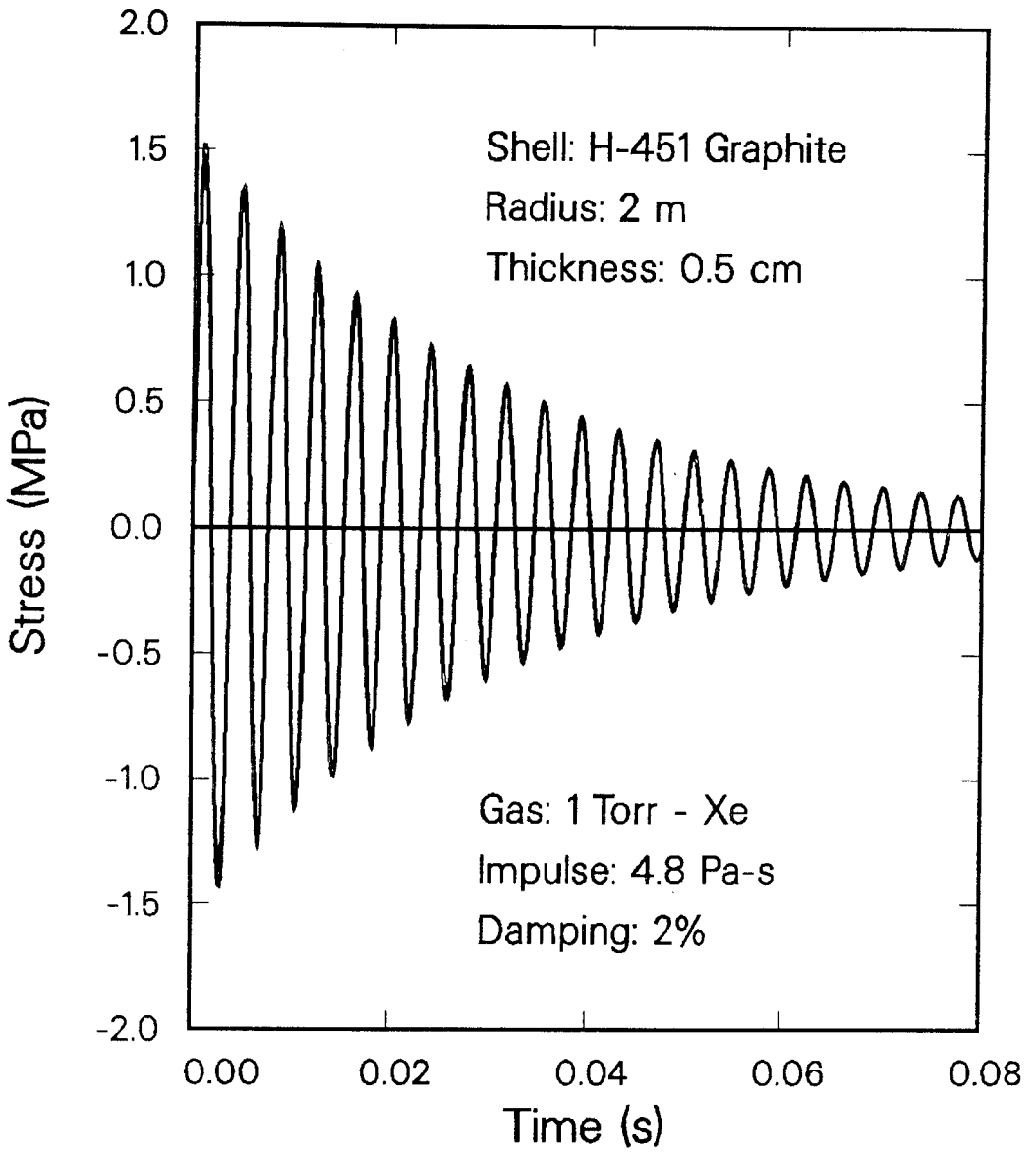

Fig. II.3.1. SIRIUS-M mechanical stress history.

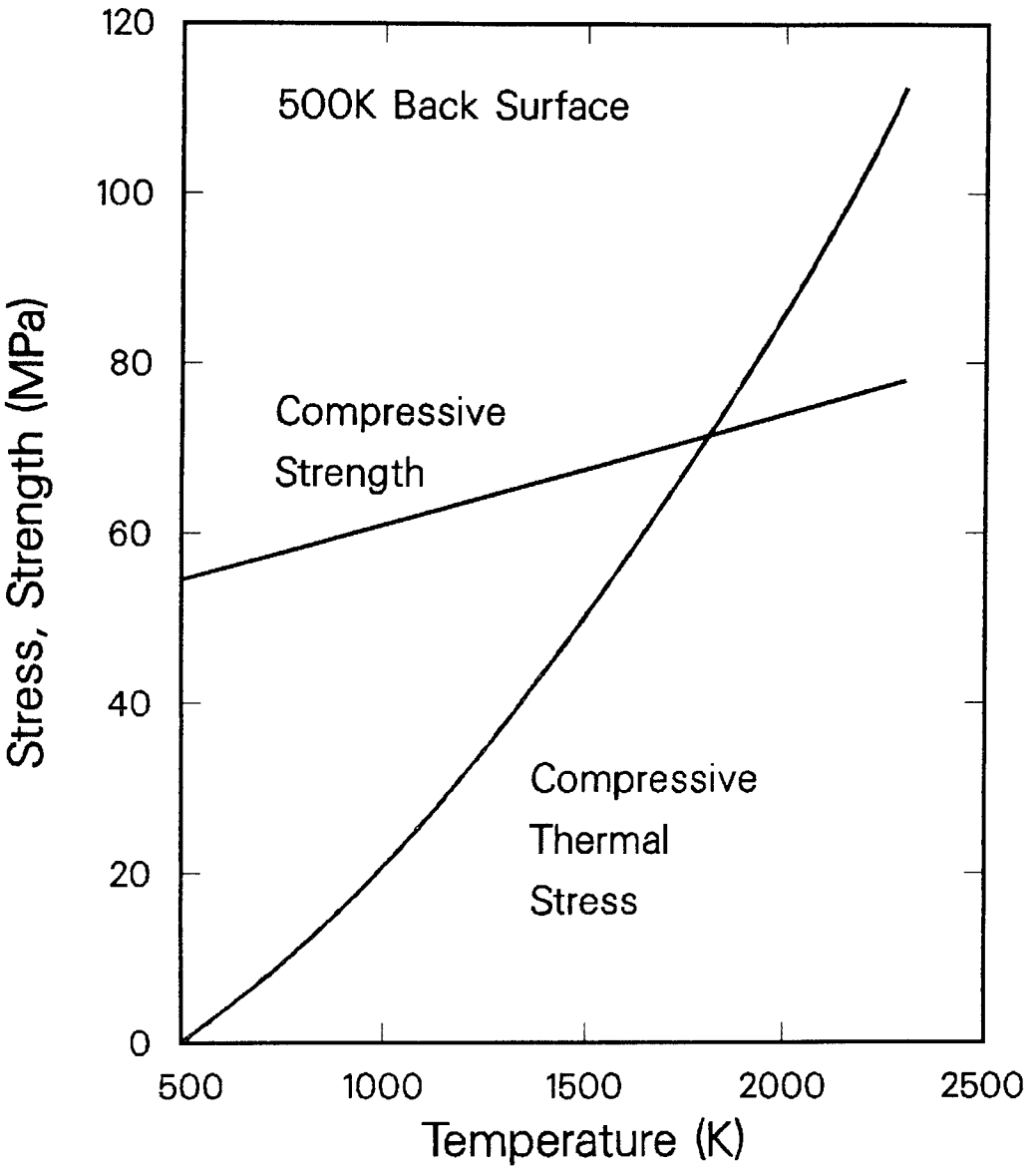

Fig. II.3.2. Thermal stress in H-451 graphite.

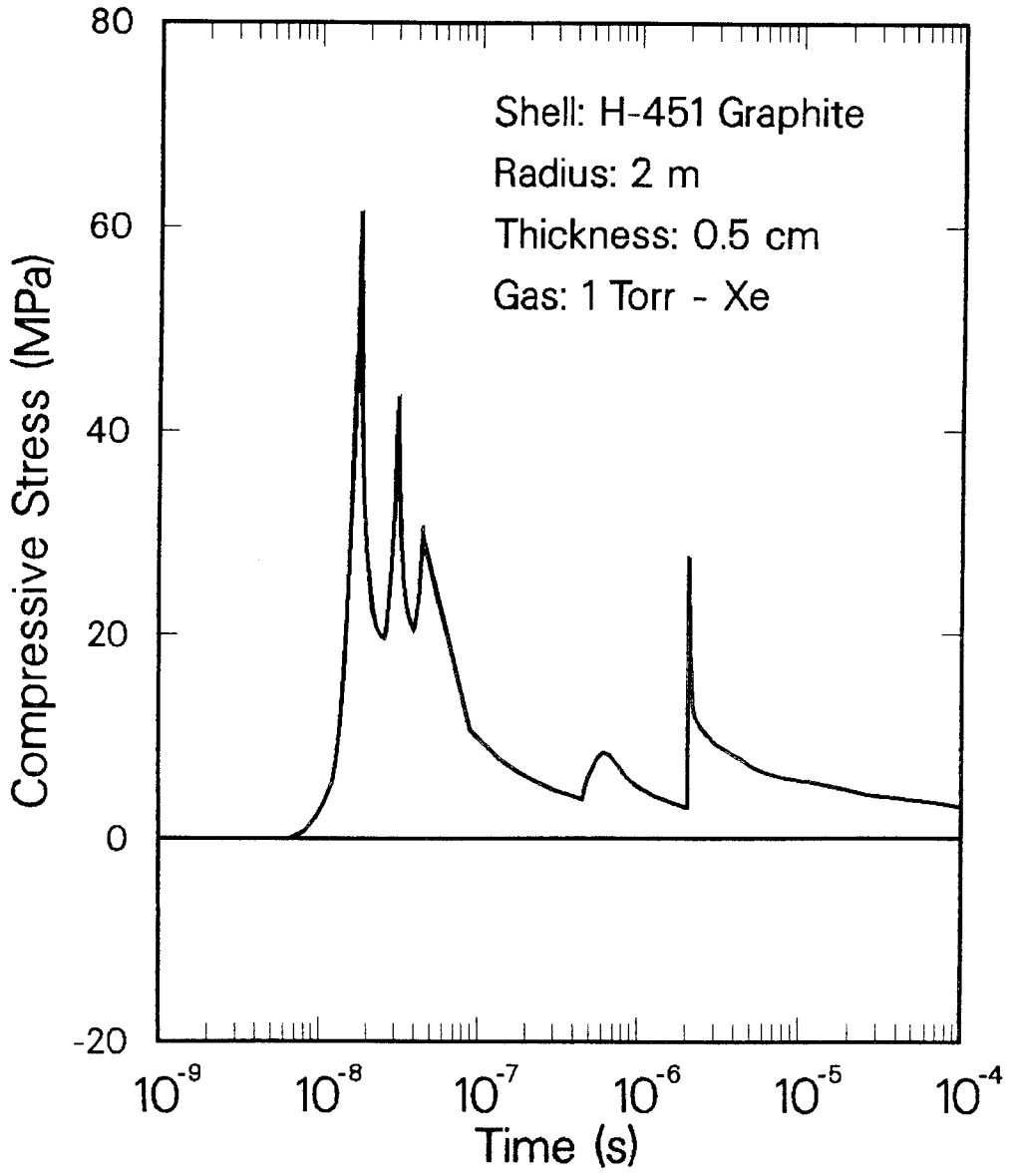

Fig. II.3.3. SIRIUS-M thermal stress history.

Fig. II.3.4

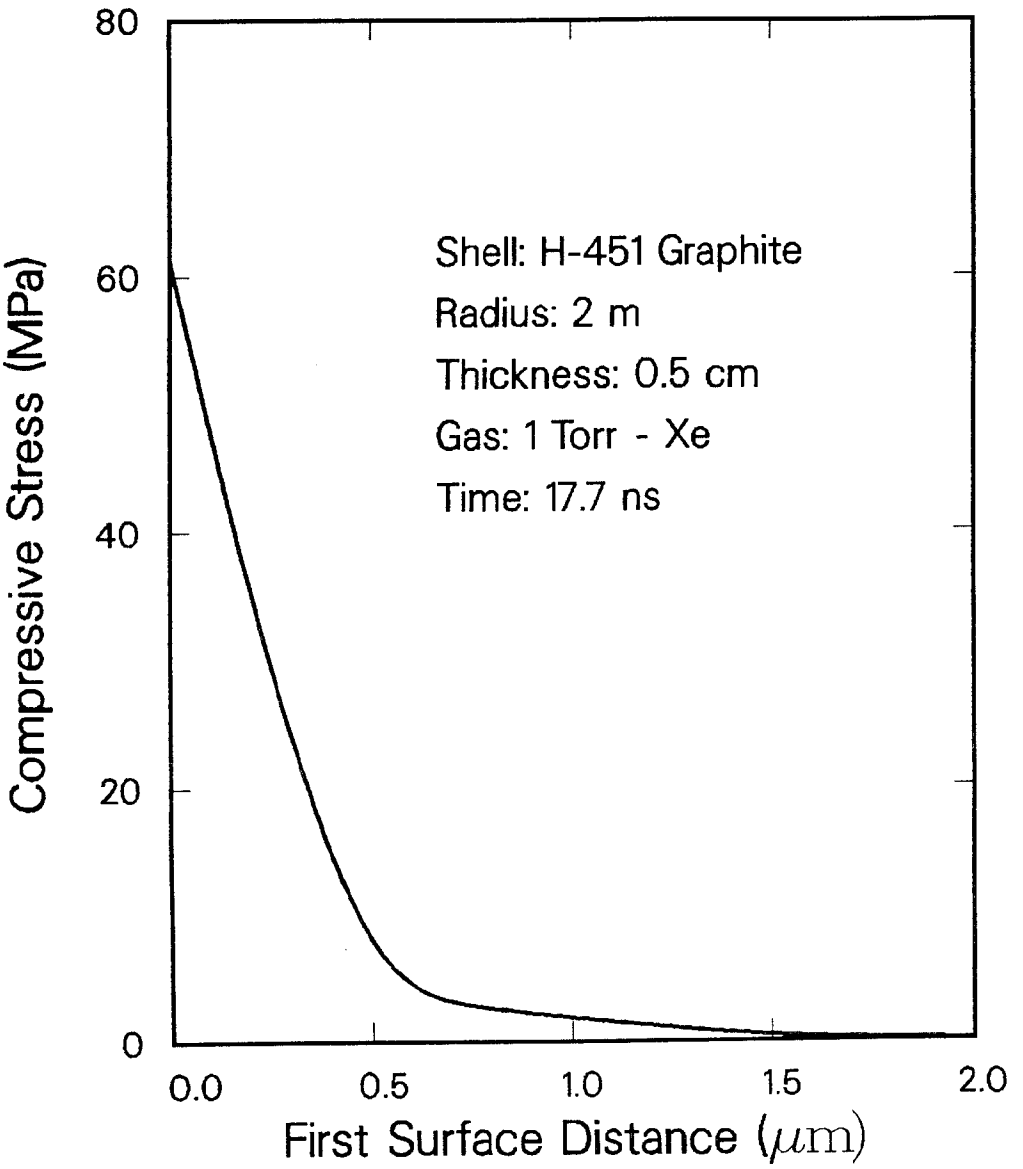

Fig. II.3.4. SIRIUS-M first wall thermal surface stress profile.

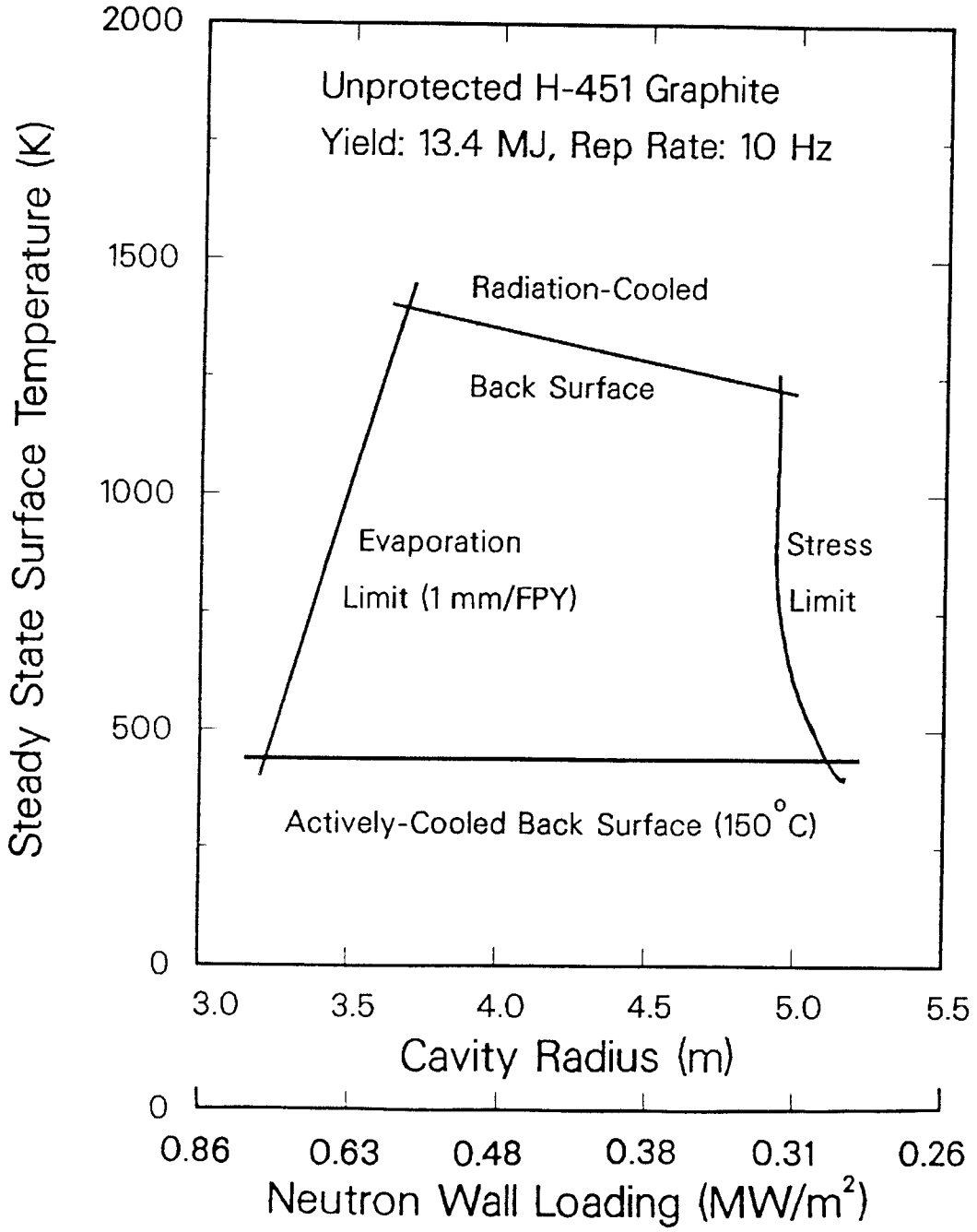

Fig. II.3.5. Evaporation and stress limits for dry wall cavities.

II.4 Gas Handling/Processing System

This section presents a conceptual design of a simple gas handling system which will process the exhaust gases from the reactor chamber, prepare decontaminated xenon gas for reinsertion in the reactor cavity, and recover, purify, and isotopically-separate DT for the preparation of new target fuel. This processing must be accomplished with low loss and minimal inventories of xenon and tritium because of the high cost of Xe ($10.20/liter (STP)) and tritium ($10,000/g) and the radiological hazard caused by tritium escaping to inhabited areas.

The required flow rate of Xe through the reactor cavity is determined by the allowable impurities in the gas which may degrade either the focus or the power of the laser beams. Such impurity levels have not been determined at this time; therefore, a one second Xe residence time in the cavity was assumed. The gas processing scheme requires, therefore, the purification of 44 liters (STP)/s Xe with small quantities (Table II.4.1) of unburned fuel (DT), He ash, target shell debris $(CH_2)_x$ and some methane and acetylene (containing H, D and T) formed by reaction of the hydrogen isotopes with the hot graphite first wall. At the high temperature of the graphite first wall, > 1000°K, a large fraction of the tritium may be chemically bound to the acetylene.

Briefly, the purification technique proposed (see Fig. II.4.1) considers the oxidation of all the reactor exhaust to form water (containing H, D and T) and carbon dioxide in the Xe carrier gas. Spectrographic analysis of Xe and hydrogen mixtures at high temperatures have reported the formation of xenon hydride. The oxidation of all the gases should destroy such a compound. The oxidized gases are next absorbed on molecular sieve beds at ambient temperature, ~ 25°C. The molecular sieves are selected for preferential adsorption

Table II.4.1. Chemical Composition of Reactor Cavity Exhaust

	m mole	ppm (volume)
Xe	1970	10^6
DT	0.22	110
He	8.3×10^{-2}	40
$(CH_2)_x$-shell debris	0.12	60
$CH_4 + C_2H_2$	(unknown - formed at expense of D, T, H molecules)	

of water and CO_2. Finally, the He is removed from the Xe by cryogenic distillation.

Specific comments on the reprocessing scheme are:

a) A gas compressor, such as a Roots-Blower, is used to exhaust the reactor cavity operating at 1 torr (133 Pa) and boost the gas pressure to nearly one atmosphere. This will decrease the volumes of the pipes and tanks needed. Nearly all of the processing system will be doubly contained so that any leaking Xe or tritium will be captured.

b) The oxidation process will require the addition of excess oxygen to the gas stream ahead of the precious metal catalysis operating at 500°C. The "cracking" of the methane, acetylene and other hydrocarbons is usually difficult. It may be necessary to recycle the gases through the oxidizer several times in order to destroy these hydrocarbons. Also, oxidation in the presence of Xe may be very inefficient because of poor mixing. The excess oxygen should probably be removed after the desiccant beds because

of the necessity to retain all hydrogen isotopes as water and the carbon as CO_2.

c) The desiccant beds are recycled approximately every 24 hours. Tritiated water is released and collected when the desiccant bed off-line is heated to 300°C. The tritium is reclaimed from this water by a technique which initially electrolyzes the water. Then, the hydrogen isotopes are sent to a cryogenic distillation column which produces a stream of pure DT (very low in protium) and a protium stream (very low in tritium). The protium stream can be vented after suitable tritium decontamination. The isotope recovery system is so small that it will probably be operated as a batch process only a few hours per day.

d) The concentration of He in the Xe is permitted to increase to nearly 1% because the He should not detrimentally affect the operation of the reactor cavity. As a result, a 4×10^{-3} fraction of the Xe flow needs to be diverted to the distillation column for He removal. Such a distillation apparatus could be small, containing only 50 cm^3 of liquid Xe and have a continuous gas throughput of only 0.2 liter (STP) Xe/s.

The inventories of Xe and tritium in the various processing equipment have been estimated, Table II.4.2. At the present Xe cost of $10.20/liter (STP) in 300 liter-gas cylinders, the Xe inventory cost is a modest $17,000. The total tritium inventory is only 114 g and needs to be compared with the amount of tritium in the target manufacturing process.

Table II.4.2. Inventory of Xenon and Tritium in Gas Handling System

	Xe liters (STP)	Tritium (g)
Reactor cavity	44	6.6×10^{-4}
Surge Tank (10 s)	440	6.6×10^{-3}
Oxidizer	22	3.3×10^{-4}
Cooler	220	3.3×10^{-3}
Dryer beds	22	57.0
Pipes	440	6.6×10^{-3}
Distillation column ($50\ cm^3$ liq. Xe)	30	---
Xe storage (10 s)	440	---
H_2-Isotope purification	---	57.0
	1658	114

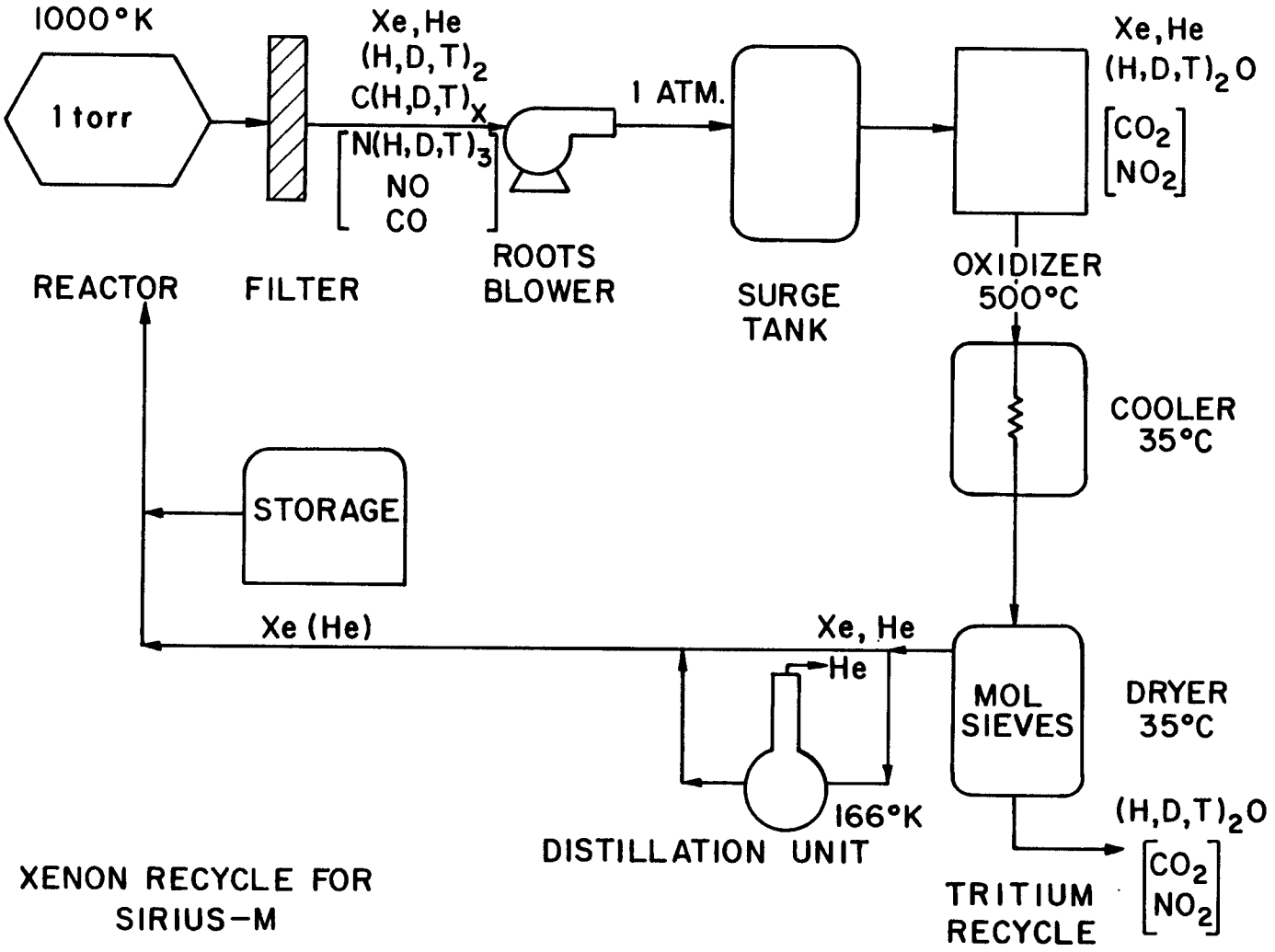

Fig. II.4.1. Xenon recycle for SIRIUS-M.

III. MATERIALS TEST MODULE ANALYSIS

III.1 Introduction

The need to test structural materials under realistic fusion reactor conditions has been discussed in both the magnetic confinement fusion (MCF) and inertial confinement fusion (ICF) communities for over a decade. It is important to emphasize the need for integrated testing of materials in the complex nuclear environment. Simply irradiating small size materials samples in a neutron flux can be accomplished in fission reactors or small DT neutron source facilities. However, the restricted temperature range and small individual test volumes, along with serious neutron energy spectral differences, make complete testing of materials in these facilities impossible. The MCF program has taken the lead in attempting to solve this problem by sponsoring several test reactor studies such as FERF,[1] TETR,[2] INTOR,[3] TASKA,[4] TASKA-M,[5] TDF[6] and FEF.[7] Most of these studies have concentrated on providing a nuclear and thermal environment which would closely simulate that to be expected in the first demonstration reactor or the first commercial magnetic fusion reactor.

In contrast to the MCF technology program, the efforts of the ICF technology program have been on conceptual design of commercial power plants and there has been a curious lack of near term test facility designs. The singular exception is a brief scoping study of a device called LA FERF[8] in 1975 at LLNL. It is commonly assumed by the ICF community that the MCF materials program will provide the data needed for designing the inertial confinement reactors. In Section III.2 we discuss the differences between the damage con-

ditions in ICF and MCF environments explaining why a dedicated ICF materials test facility such as SIRIUS-M is needed.

To test materials for an ICF demonstration, we need to obtain high integrated fluence (in the neighborhood of 5 MW-yr/m^2) under reactor relevant conditions in the shortest possible time. This required placing the test module as close as possible to the target to achieve a high neutron wall loading. Furthermore, attempts were made to increase the damage rate in the test module, for the same wall loading, by using different reflector materials and varying the reflector location relative to the test module. The results of this parametric study are given in Section III.3. The damage profiles and testing capability for the final SIRIUS-M test module design are given in Section III.4.

III.2 Comparison Between Damage Condition in ICF and MCF Reactors

Neutron damage to structural materials in ICF and MCF reactors can be significantly different even when the first wall is exposed to the same level of radiation (quoted in MW-yr/m^2). These discrepancies arise from geometrical, spectral, and temporal effects. Before considering the combined effects of these parameters, it is worthwhile to examine them individually.

III.2.1 Geometrical Differences

While a cylindrical (or toroidal) chamber surrounds a volumetric distributed neutron source in a MCF reactor, a point neutron source is usually surrounded by a spherical first wall in ICF reactors. At first glance, one would not expect that the damage per MW-yr/m^2 in the first wall to be significantly different in the two cases. Close examination of the problem reveals that due to the formal definition of the neutron wall loading, there can be substantial differences in damage rates and profiles. The neutron wall loading is defined as the energy carried by uncollided source neutrons incident on a unit area of the wall per unit time regardless of the direction of incidence. While the same neutron wall loading in the ICF and MCF geometries implies the same number of source neutrons incident on unit area of the first wall, the incidence angles of these neutrons are quite different. In the ICF geometry all neutrons from the point source are incident perpendicular to the spherical wall resulting in less damage in the first wall and more damage in the back of the reflector as compared to the MCF case where neutrons from the volumetric distributed source are incident on the cylindrical wall at different glancing angles.

The damage rate profiles were calculated in a 20 cm thick test module consisting of 20% HT-9, 20% NaK and 20% 316 SS and backed by 60 cm steel

shield for both ICF and MCF geometries. A first wall radius of 2 m and a neutron wall loading of 2 MW/m^2, representative of SIRIUS-M conditions, were used. The results for the dpa rate are given in Fig. III.2.1 for a monoenergetic 14.1 MeV neutron source. The results clearly demonstrate that the first wall damage in MCF cylindrical geometry is ~ 50% higher than that in ICF spherical geometry. The situation is even more severe for helium production as 67% more helium is produced per $MW\text{-}yr/m^2$ in the cylindrical wall. Fortunately, the He/dpa ratios are only 11% different as shown in Fig. III.2.2. It is clear also from the results of Fig. III.2.1 that there is a faster dropoff in the damage rate as one proceeds from the first wall into the reflector of a cylindrical chamber. This faster dropoff, despite the slower geometrical dropoff (1/R vs. $1/R^2$ in spherical geometry), is due to the different angular distribution of incident neutrons as discussed above.

Another important geometrical effect relates to the chamber radius of test facilities. For various reasons, relating to plasma physics and the ability of first walls to stand high heat fluxes without melting, the radii of ICF and MCF test facilities might be quite different. For example, the first MCF materials test facility will probably be a tandem mirror. The plasma chamber in this type of device will be a long, but rather small radius tube. Designers of the TASKA,[4] TDF[6] and TASKA-M[5] facilities have all chosen wall radii in the range 0.2-0.4 m. In contrast, the minimum radius of the first ICF test chamber is likely to be at least 2 m in order to avoid melting of the first wall during the target explosion.

The effect of first wall radius on the dpa rate in the test module is shown in Fig. III.2.3 for a cylindrical chamber. The larger the radius the higher the dpa rate in the first wall for the same neutron wall loading. The

reason is that the first wall has a larger view factor for secondary backscattered neutrons, eventually approaching 2π sr as the chamber radius goes to infinity. Since the secondary neutrons do not generally produce more helium, the He/dpa ratio will decrease. While the 2 m radius results in 27% higher first wall dpa, only 5% more helium is produced per MW-yr/m^2. The appm He/dpa ratio dropped by 8%. The chamber radius effect is more pronounced in the spherical geometry. The dropoff in the damage rate as one proceeds from the first wall to the back of the reflector is smaller for the larger chamber radius due to the less influence of geometrical attenuation.

The combined geometrical effects of a point neutron source, spherical chamber and large radius in ICF reactors versus a volumetric neutron source, cylindrical geometry and small radius in MCF test reactors result in 31% more dpa, 59% more He, and 20% more He/dpa ratio in the first wall of a MCF test facility compared to an ICF test facility.

III.2.2 Spectral Differences

The main difference between ICF and MCF neutron spectra is due to the slowing down of neutrons in the highly compressed target before they hit the first wall. Whereas the neutrons emanating from a MCF plasma have a rather well defined energy at 14.1 MeV, those escaping an ICF target can have average energies as low as 10 MeV at high ρR values. The relationship between the average neutron energy impinging on the first wall of an ICF reactor versus the ρR value of the fuel is shown in Fig. III.2.4.[9] The lower the average energy of the impinging neutrons, the larger the required number of source neutrons incident on the first wall in order to achieve the same neutron wall loading.

The effect of neutron source spectrum is shown in Fig. III.2.5 where dpa rate is plotted versus depth in the test module utilizing two neutron source spectra. The first one is a monoenergetic 14.1 MeV neutron source and the second represents the spectrum of neutrons leaking from the SIRIUS-M target. There are 78% of these neutrons at 14.1 MeV, 21% in the range 3.5-14.1 MeV and 1% in the range 1.5-3.5 MeV. The average energy of these neutrons is 12.5 MeV. Because of the lower average neutron energy, a larger neutron source strength (~ 13%) is required to achieve the same wall loading. However, the degraded neutrons cause somewhat less displacement damage than the 14.1 MeV neutrons and that is why the dpa produced in the first wall per MW-yr/m^2 is only 9% higher. The Doppler broadening of the MCF source has a relatively small effect on the dpa values and aside from some reactions which have thresholds at 14 MeV and higher it is not as important as other effects considered here.

When the amount of He produced was calculated for the various spectra it was found to be essentially the same in spite of the 13% higher neutron flux required indicating a balancing of the lower He production cross section and the higher neutron flux. The He/dpa ratio was 10% lower for the degraded neutron spectrum.

III.2.3 Combined Geometrical and Spectral Effects

The geometrical and spectral effects previously illustrated can now be combined to demonstrate how dependent the damage conditions might be on reactor confinement concept. The damage rates and profiles in the test module were compared for typical ICF and MCF test facilities. SIRIUS-M parameters were used for the ICF facility while the parameters for a tandem mirror test facility of the TASKA type were used to represent the MCF facility. The input

to the calculation is summarized below:

	ICF	MCF
Type	laser	tandem mirror
Chamber Geometry	spherical	cylindrical
Radius of Chamber, m	2.0	0.3
Neutron Source Distribution	point	volumetric
Neutron Source Energy	$\rho R = 2\ gcm^{-2}$	Doppler broadening (T = 3.0 keV)
	$\overline{E}$ = 12.5 MeV	$\overline{E}$ = 14.1 MeV

The dpa rate variation in the test module is given in Fig. III.2.6 for the two facilities normalized to the same neutron wall loading. The damage rate in the first wall of the MCF facility is 21% higher than that for the ICF facility but drops faster as one moves towards the back of the test module to a value 37% lower than that in the ICF facility. A comparison between the first wall damage per MW-yr/m^2 is shown in Fig. III.2.7. The effect on helium production is more pronounced with 62% more helium produced in the first wall of the MCF facility versus the ICF reactor. The He/dpa ratio is 35% higher in the MCF case. However, due to the smaller damage gradient in an ICF module, the average dpa rate in the ICF test module is 17% higher than that in an identical test module located in a MCF facility. The average helium production rate in the ICF facility is 2% higher than that in a MCF facility.

These results illustrate that damage units per MW-yr/m^2 are very design dependent. Simply, a MW-yr/m^2 fluence produces damage in a MCF facility that could be quite different than damage produced by a MW-yr/m^2 in an ICF system.

III.2.4 Time Related Effects

A major difference between the ICF and MCF system is the time over which the displacement and transmutation damage is produced. While the time averaged damage rates were compared in the previous sections, adding the time structure of the produced damage results in even larger differences.

In MCF reactors, a steady state first wall damage rate of 10^{-7} to 10^{-6} dpa/s may last for weeks or months before being interrupted. The situation for the ICF test facilities is drastically different. The neutrons are born over 10-100 picosecond time scales and the uncollided neutrons travel toward the first wall at a velocity of roughly 50,000 km/s. This means that the neutrons could transverse a 2 m radius spherical chamber in about 35 ns. Those that get downscattered in the target have slower velocities, but all of the neutrons from the target arrive at the first wall over a time period of 5-10 ns. For a 1 MW/m^2 wall loading at a 1 Hz repetition rate, this "first wave" of neutrons can produce damage rates on the order of 70 dpa/s as shown in Fig. III.2.8. For SIRIUS-M with a repetition rate of 10 Hz and 2 MW/m^2 wall loading the peak instantaneous first wall dpa rate is 14 dpa/s. Backscattered neutrons from the reflector extend the damage time for another 50 ns or so but usually 99% of the displacement damage is produced in less than 10 ns. This leaves a relatively long time between shots where the damage can anneal out or agglomerate into different microdefects. Figure III.2.8 illustrates the wide difference in instantaneous damage rates for ICF and MCF materials test facilities. The more than 8 orders of magnitude difference in displacement rates is accentuated by the time between shots where annealing can occur.

A recent review of pulsed damage effects[10] concluded that there is sufficient experimental and theoretical evidence to be concerned about this phenomenon. Pulsing effects on precipitate phase stability and large changes in swelling and interstitial loops have been observed in stainless steel.[11] Large changes in the void microstructure in Ni irradiated under pulsed conditions have also been observed.[12] It is therefore clear that in addition to the geometrical and spectral differences, the damage produced by 1 MW-yr/m^2 exposure under steady state conditions might bear no resemblance to 1 MW-yr/m^2 applied in a pulsed mode.

It is concluded that materials information generated to meet MCF applications may not be adequate to determine their behavior in ICF environments. Reliance on MCF test facilities may not be in the best interest of the ICF program in the long run and a dedicated ICF materials test facility is needed.

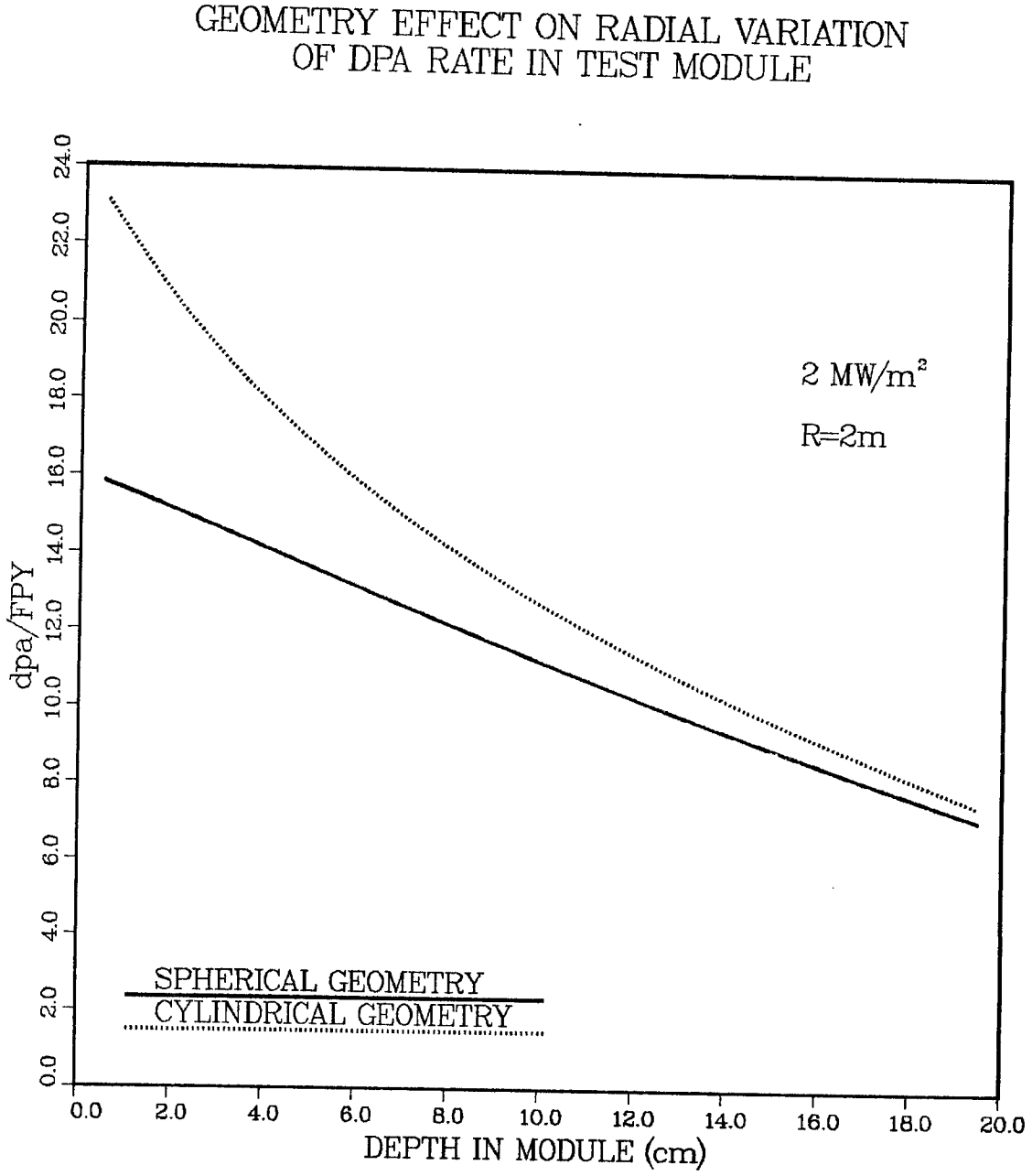

Fig. III.2.1. Geometry effect on spatial variation of dpa rate in test module.

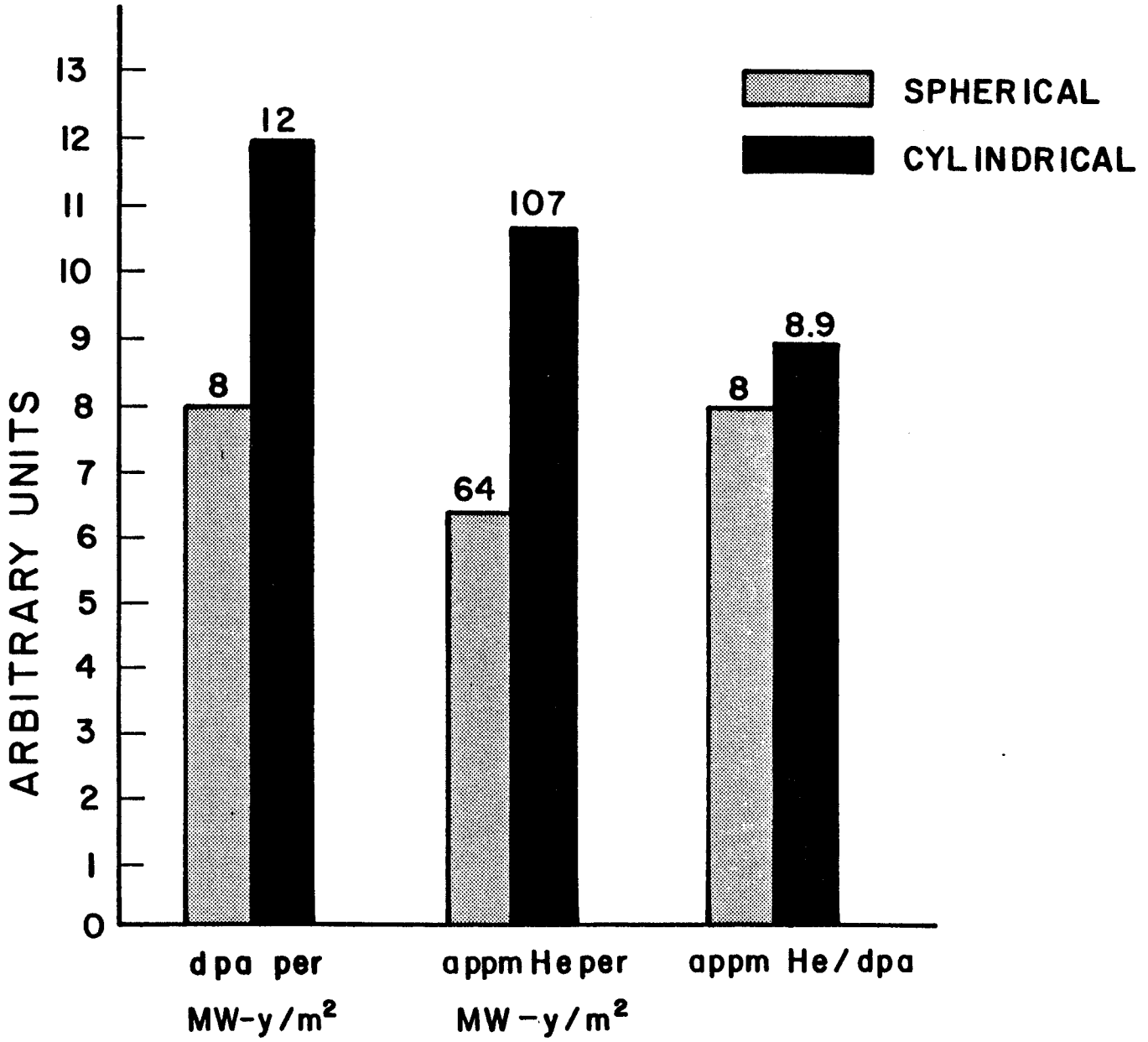

Fig. III.2.2. Comparison of damage parameters in steel first walls of equal radii (2 m) spherical and cylindrical chambers.

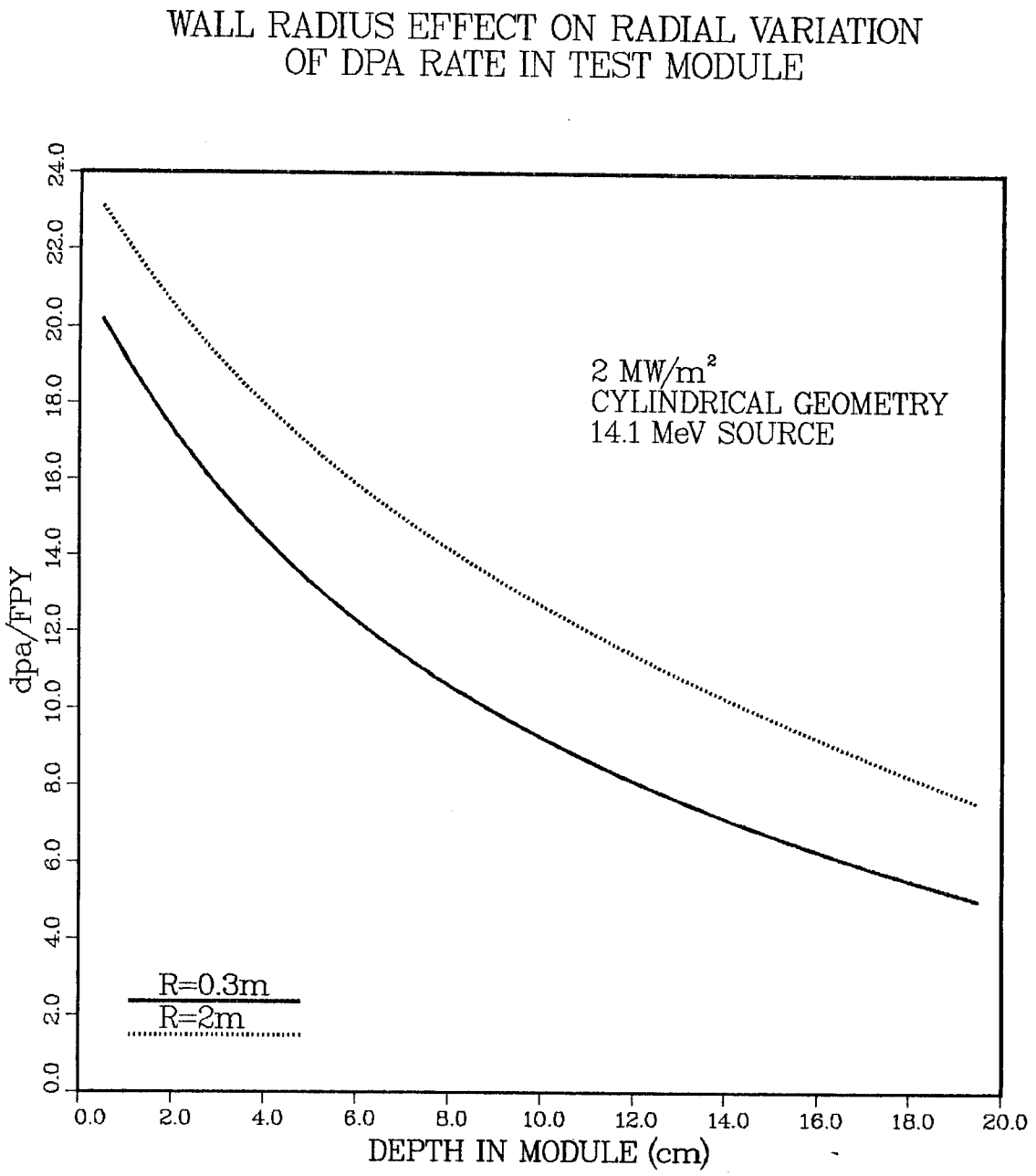

Fig. III.2.3. Wall radius effect on spatial variation of dpa rate in test module.

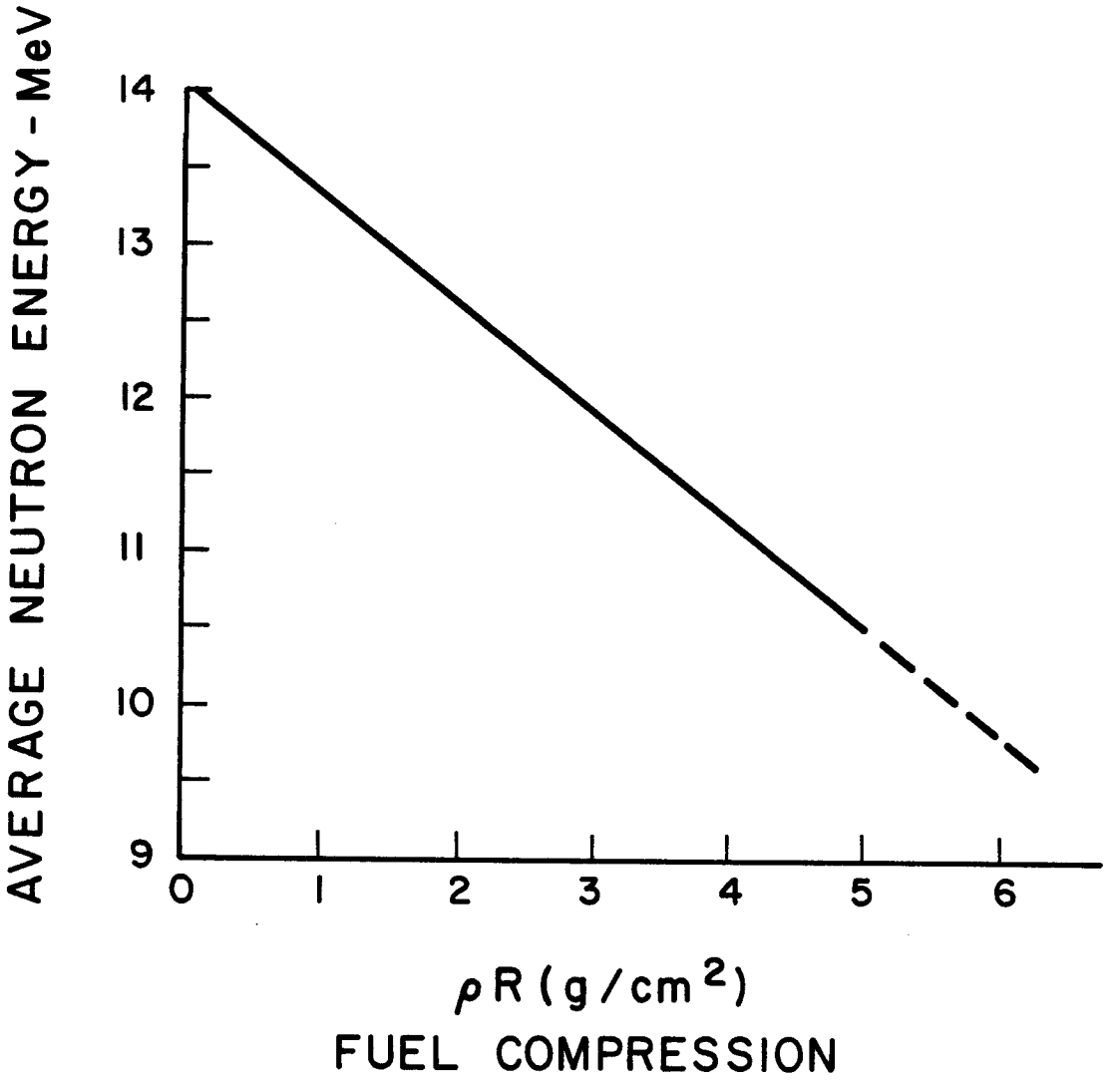

Fig. III.2.4. Effect of fuel compression on average energy of neutrons emitted from the target.

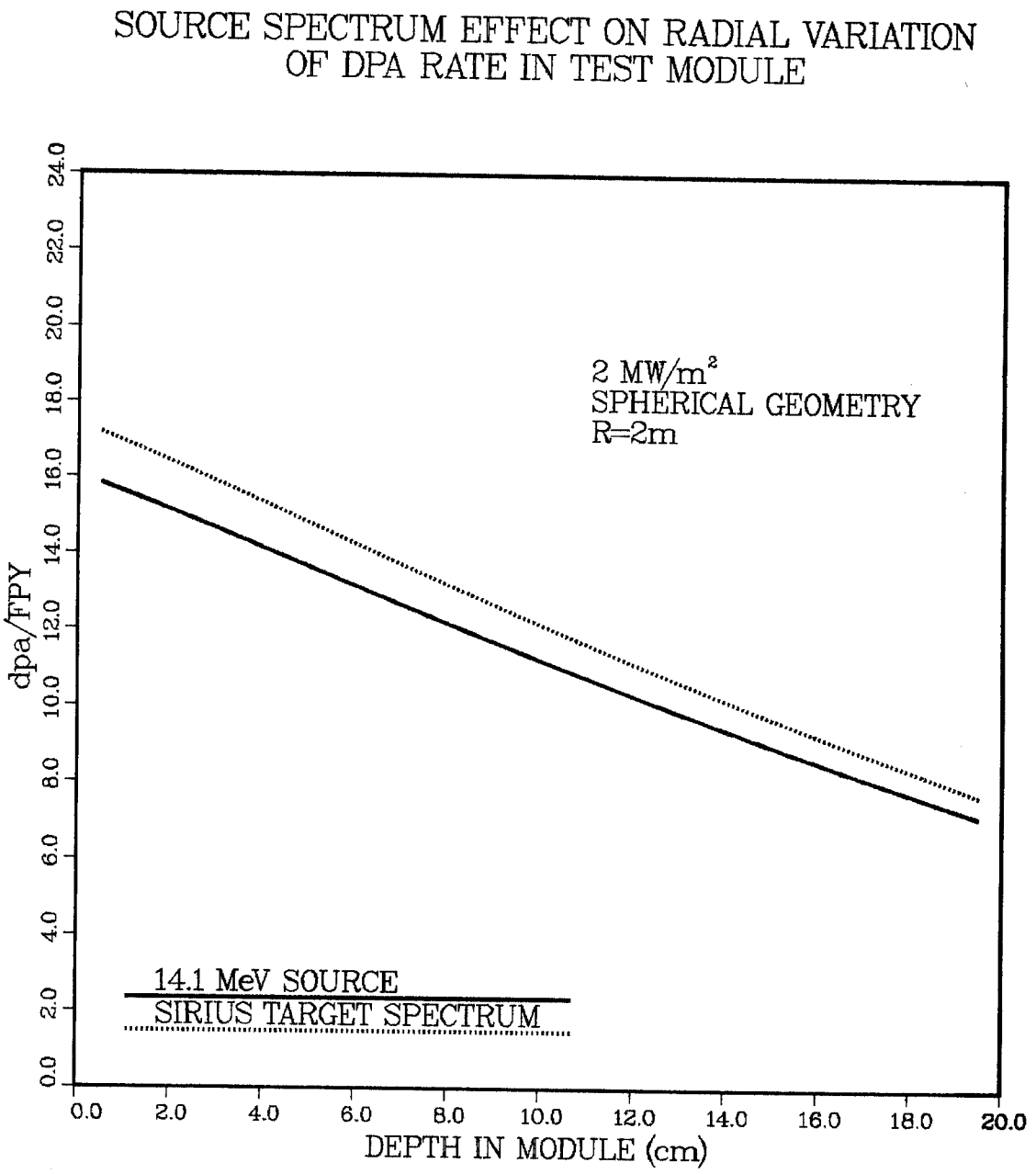

Fig. III.2.5. Source spectrum effect on radial variation of dpa rate in test module.

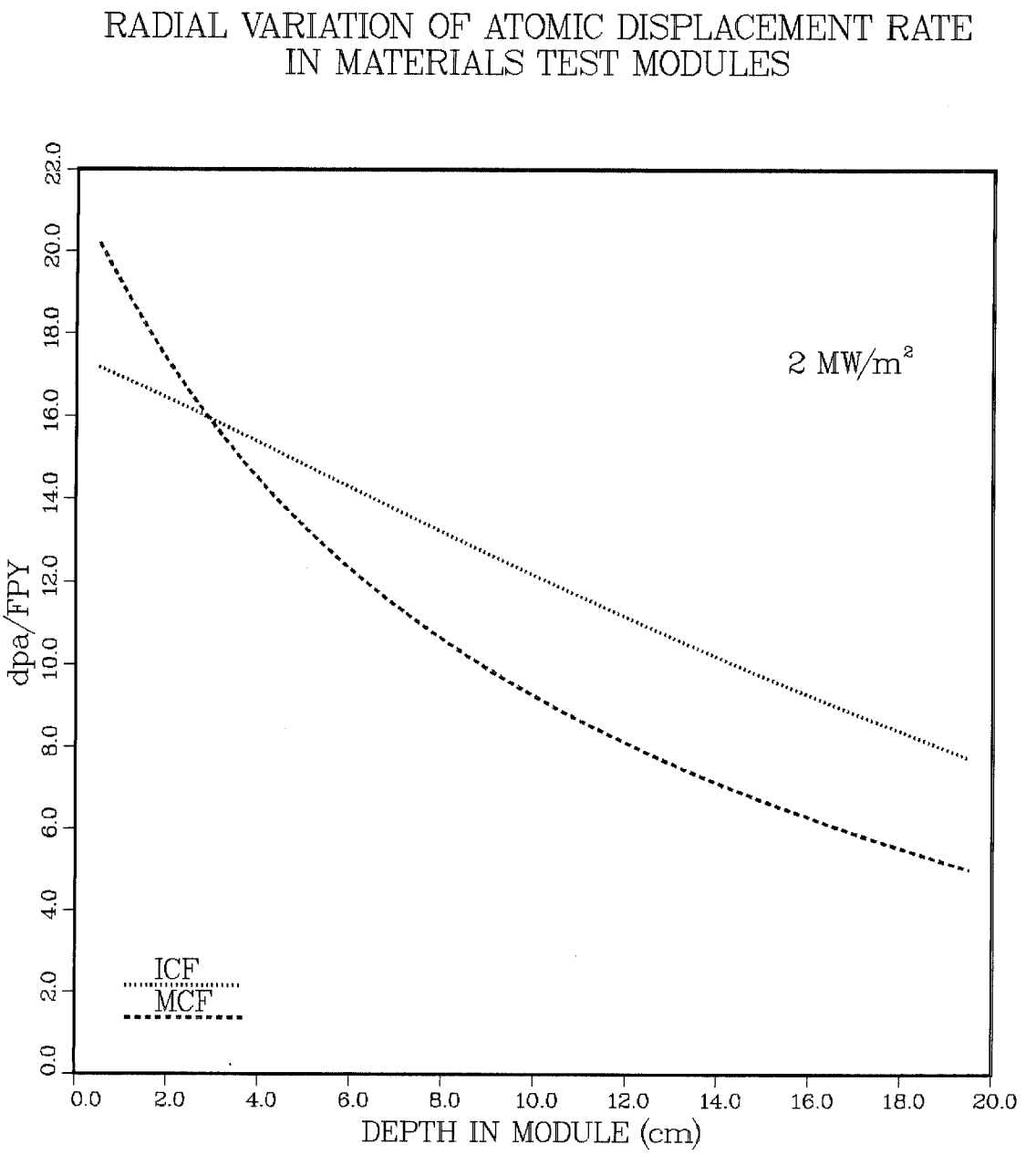

Fig. III.2.6. Spatial variation of dpa rate in ICF and MCF test modules exposed to the same neutron wall loading of 2 MW/m^2.

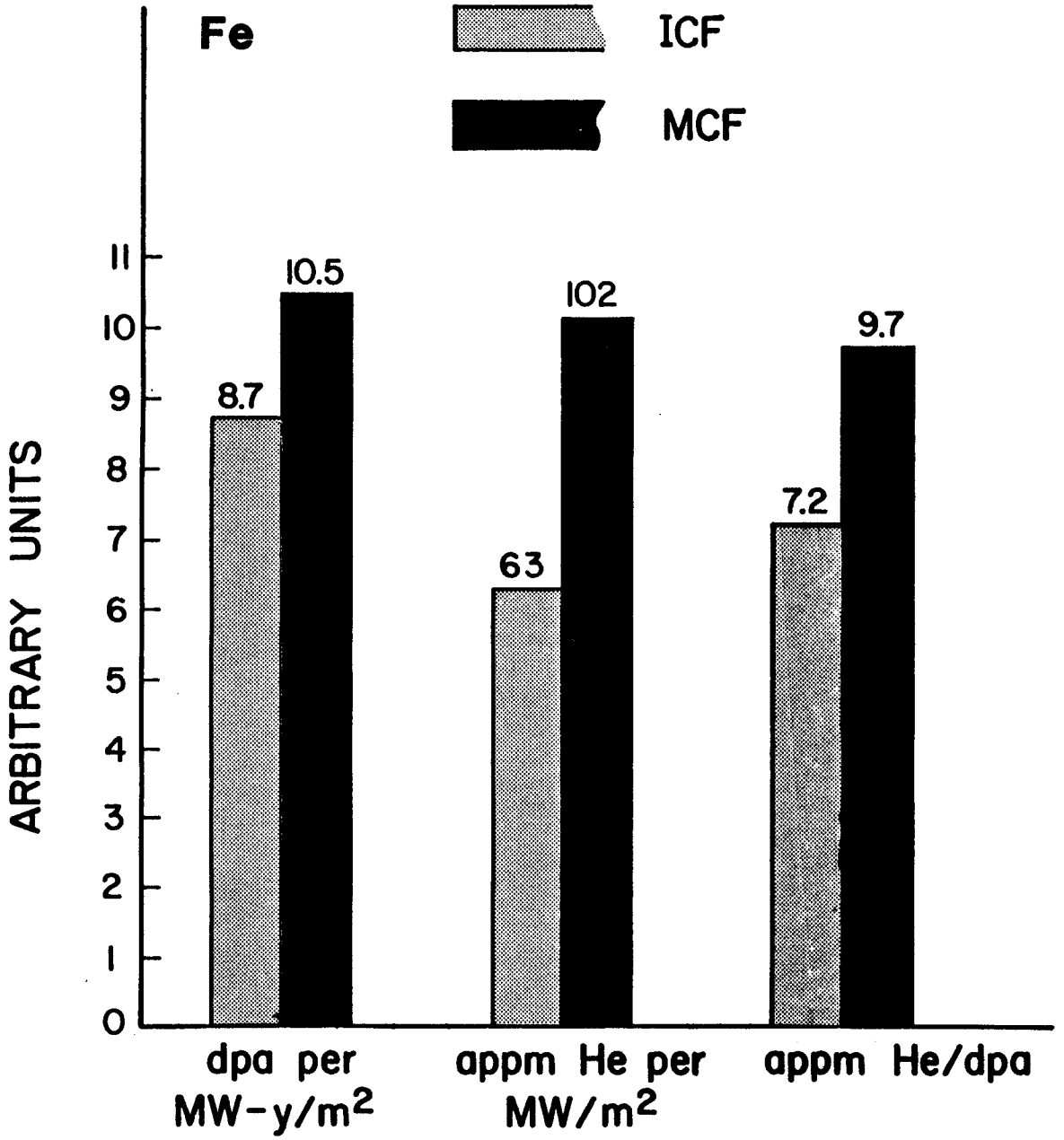

Fig. III.2.7. Comparison between damage effects in the first walls of typical ICF and MCF test facilities.

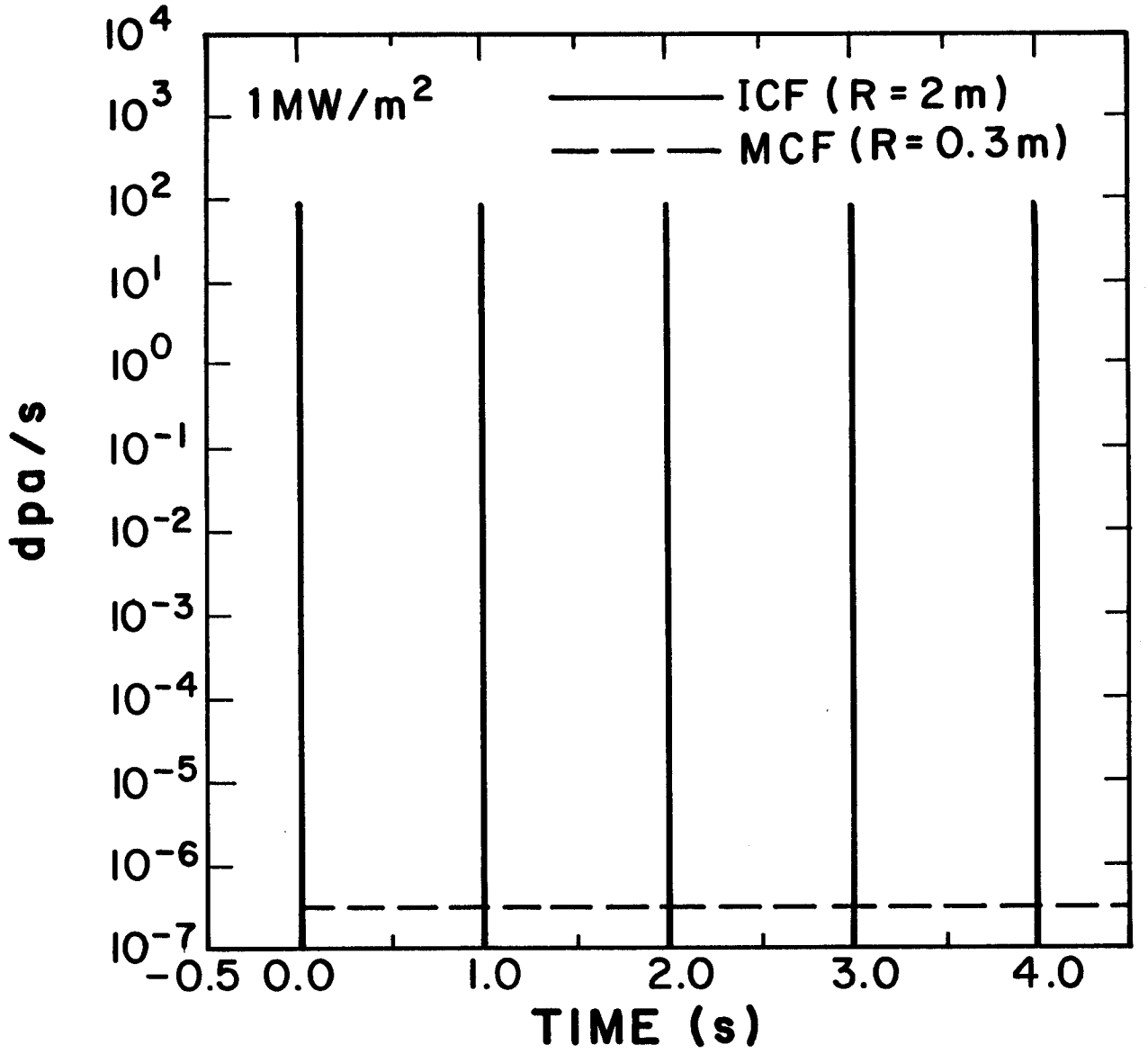

Fig. III.2.8. Comparison between steady state damage rate in a typical MCF test facility and pulsed damage in an ICF test facility with the same wall loading and 1 Hz repetition rate.

III.3 Parametric Studies for the SIRIUS-M Materials Test Module

The test module of SIRIUS-M should be designed such that the test specimens accumulate high damage levels in the shortest possible time. This can be achieved by locating the module as close as possible to the target such that the front of the module is exposed to a high neutron wall loading. However, the need to protect the module from the target ion debris and x-rays imposes a lower limit on the distance between the target and module. A tradeoff study resulted in locating the test module in SIRIUS-M at a distance of 2 m from the target. For a target yield of 13.4 MJ and a repetition rate of 10 Hz, this results in a neutron wall loading of 2 MW/m^2 at the front surface of the module. The test module is protected from the high surface heat flux resulting from x-rays and ion debris (7 J/cm^2) by 1 torr xenon gas. A graphite liner is also used on the test module surface to protect it from the cyclic high heat flux. The impact of the graphite liner on the damage levels achievable in the test module is discussed in Section III.3.1. The reflector material choice and reflector location relative to the test module impact the neutron flux and spectrum in the test module and hence influence the achievable damage rate. An effort was made to maximize the damage rate by proper choice of reflector material and location. This is discussed in Section III.3.2.

III.3.1 Effect of Graphite Liner on Test Module Damage Parameters

The test module was modeled in one-dimensional spherical geometry to investigate the impact of the graphite liner. A 1 cm thick liner at a radius of 2 m was followed by a 20 cm thick test zone. The module was backed by a 40 cm thick steel shield. The discrete ordinates code ONEDANT[13] was used with group cross section data based on ENDF/B-V.

Figure III.3.1 gives the spatial variation of dpa rate in the test module with and without the graphite liner. The dpa rate drops by 6% as a result of using 1 cm of graphite. The effect on helium production is smaller with only a 2.4% reduction. This is due to the fact that graphite is more effective in slowing down and attenuating the intermediate and low energy neutrons which contribute relatively more to atomic displacement than to helium production.

Although a graphite liner thickness of 1 cm was proposed to provide adequate protection for the permanent reactor first wall, a thinner liner can be used for the test module which will be frequently removed from the reactor for test specimen replacement allowing for frequent replacement of the liner if significant erosion occurs. Based on a maximum allowable liner erosion rate of 1 mm/FPY, a 2 mm thick liner is used at the outer surface of the test module. This results in a 2.4% drop in the dpa rate and only a 0.5% drop in the helium production rate compared to the case when no graphite liner is used.

III.3.2 Effect of Reflector Material and Location on Test Module Damage Parameters

In the early stages of the SIRIUS-M design, a chamber radius of 8 m was proposed with a cantilevered test module that is located at a radius of 2 m and exposed to a neutron wall loading of 2 MW/m^2. This geometry was modeled for the three-dimensional neutronics calculations using the Monte Carlo code MCNP.[14] The geometrical model used in the calculations is shown in Fig. III.3.2. The material composition used for the test module is the same as that given in Section III.2.1. The module has a circular front surface with an area of 1.5 m^2 and is covered by a 1 cm thick graphite liner. The module was divided into five concentric annular zones as indicated in Fig. III.3.2 to determine the radial variation of damage. Each zone was segmented into five

axial segments to determine the axial damage variation. A 50 cm thick reflector zone was used in the calculations to properly account for contribution of reflected neutrons to the damage in the test module. Reflection from materials behind this 50 cm zone has negligible effect on the damage in the test module. Two options were considered for the reflector material; one is a steel reflector made of 90% HT-9 and 10% H_2O and the other is a lead reflector consisting of 90% molten lead and 10% HT-9. The inner surface of the reflector is covered by a 1 cm thick graphite tile. The test module and reflector were connected by a 30 cm cylindrical zone consisting of 80% HT-9 and 20% He gas. This zone was used in the calculations to represent the piping and coolant manifolding required for the test module. The effect of the reflector location relative to the test module was analyzed by performing calculations for cavity radii of 8, 4 and 2 m.

A comparison between the values of the peak dpa rate in the test module calculated for the different cases is shown in Fig. III.3.3. It is clear that bringing the reflector closer to the test module results in significant enhancement of the damage produced in the test module. The reason is that the test module has a larger view factor for secondary neutrons reflected from a smaller radius reflector. The effect on helium production is much less pronounced due to the fact that secondary reflected neutrons contribute very little to helium production.

The location in the test module where the peak damage occurs is different in the six cases considered. For the 8 m cavity radius, the peak occurs at the front surface of the module along the module centerline due to the reflection from the steel rod at the back of the central part of the module. The peak dpa rate in the central zone of the module is 12% higher than that in the

outer zone. The radial damage gradient reduces as a cavity radius of 4 m is used due to the increased contribution from neutrons reflected from the reflector to damage in outer zones of the module. For a cavity radius of 2 m, the peak damage in the module is shifted to the outer zone due to the increased contribution from the surrounding reflector. In this case the peak is 3% higher than that in the central zone. The axial damage gradient was found to decrease as the cavity radius is reduced due to the increased contribution at the back of the module from neutrons reflected by the reflector. The cavity radius has a much smaller effect on the spatial variation of helium production in the test module due to the small contribution of secondary neutrons to helium production. Table III.3.1 gives the average dpa and He production rates in the test module for the different cavity radii and reflector materials.

The effect of using a neutron multiplier in the reflector on enhancing the dpa rate in the test module is clear from the results of Fig. III.3.3 and Table III.3.1. Neutron multiplication in lead enhances the neutron flux at the test module yielding ~ 50% higher dpa rate than that in the steel reflector case for a 2 m radius cavity. The effect is smaller for larger cavity radii due to the smaller contribution of secondary neutrons reflected from the reflector. On the other hand, the He production rate remains about the same or becomes slightly smaller as most of the neutrons produced in (n,2n) reactions in Pb have energies below the (n,α) threshold energy. Although beryllium is a better neutron multiplier than lead, we have shown that using Be instead of Pb in the shield surrounding the materials test module of TASKA-M[5] results in a slightly (~ 2%) reduced dpa rate in the module. This is due to the fact that while the neutrons produced from (n,2n) reactions in Pb are

Table III.3.1. Average Damage Rate in Test Module for the Different Design Options

Cavity Radius (m)	Reflector Material	Average dpa/FPY	Average He appm/FPY
8	steel	7.26	70.33
8	lead	7.91	70.49
4	steel	7.97	71.19
4	lead	10.17	70.36
2	steel	10.39	74.02
2	lead	16.08	73.53

emitted isotropically, the neutrons are preferentially emitted in the forward direction in the case of Be with a smaller fraction of them returning into the cavity and contributing to damage in the test module. Furthermore, the secondary neutrons produced from Be have a softer spectrum that has less damage contribution. These effects counterbalance the increased neutrons produced in (n,2n) reactions in Be. Another reason for using Pb instead of Be is that tritium is produced in Be which negates the advantage of having a tritium free reflector in SIRIUS-M. We estimated that ~ 30 g T_2 will be produced per FPY if a Be reflector is used in SIRIUS-M.

It is concluded from the results of this section that the damage rate achievable in the test module can be maximized by incorporating the test module into a lead reflector. This design results in doubling the dpa rate

and testing capability of the module compared to the initial cantilevered test module design with a steel reflector. Reducing the permanent chamber wall radius to 2 m was the main reason for using a reduced target yield of 13.4 MJ with 1 torr xenon gas protection and protective tiles made of a 1 cm graphite layer followed by 1.5 cm of 40% HT-9 and 60% H_2O. The neutronics calculations for the final SIRIUS-M design are presented in the next section.

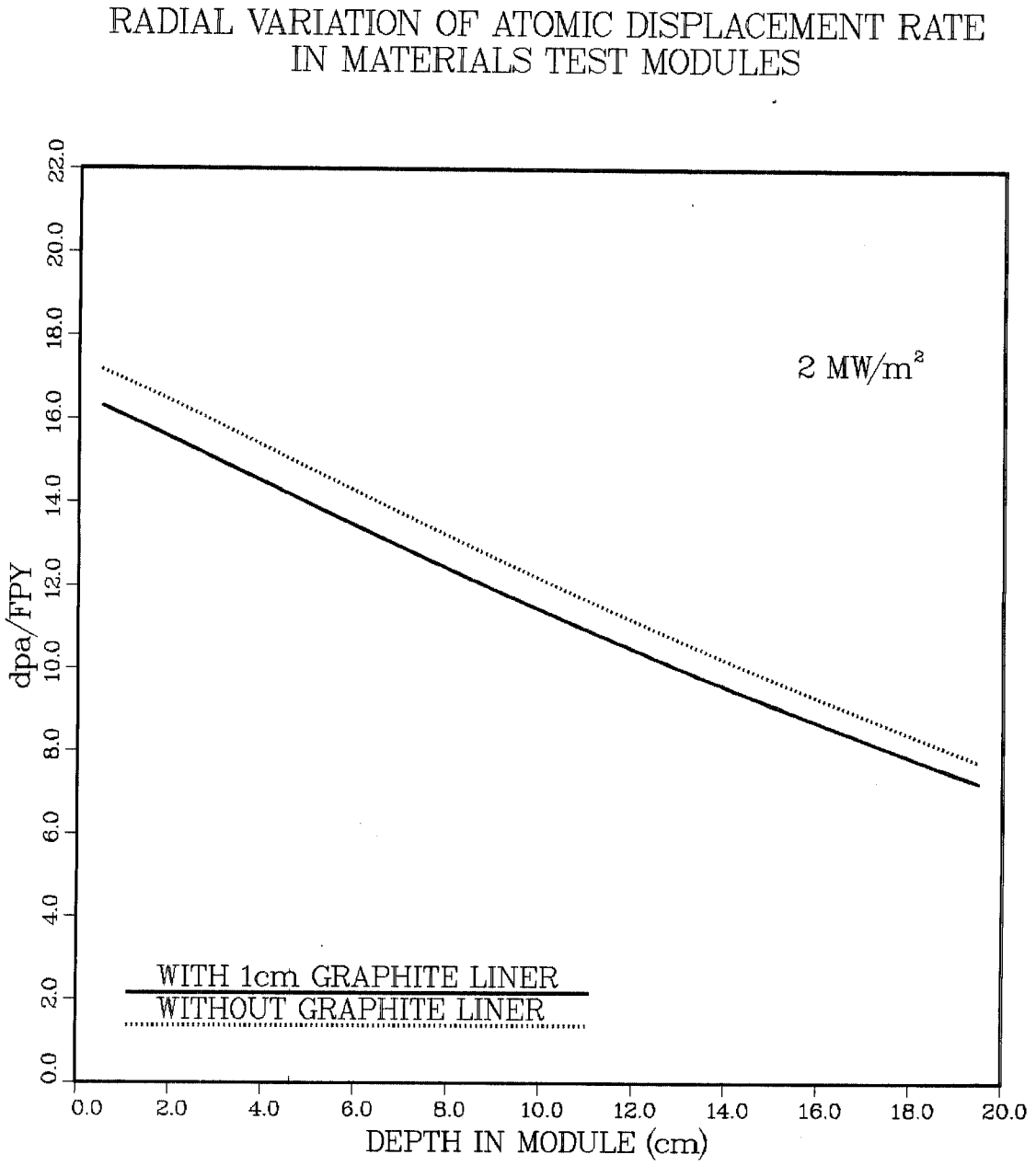

Fig. III.3.1. Spatial variation of dpa rate in the test module with and without 1 cm thick graphite liner.

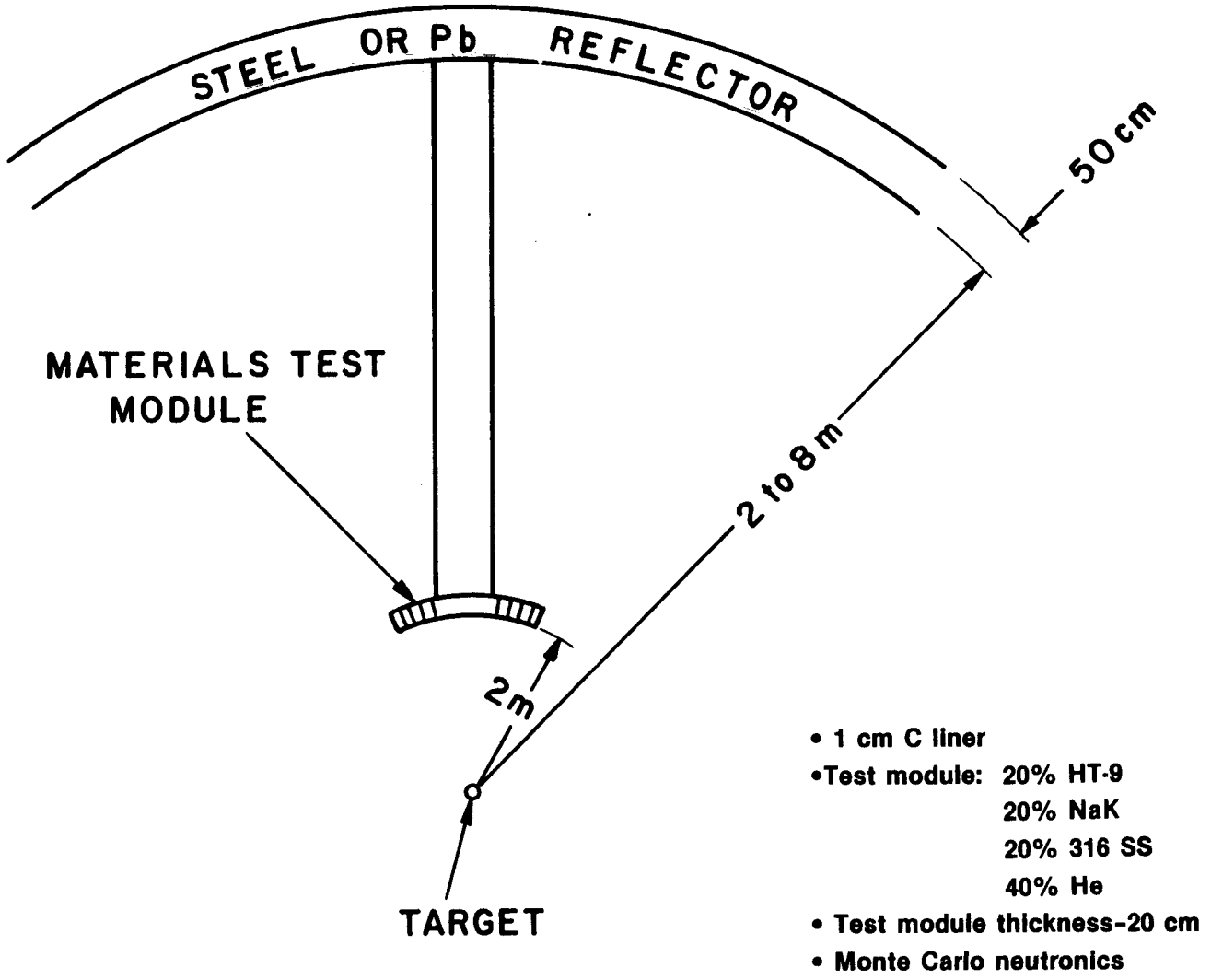

Fig. III.3.2. Geometrical model used in Monte Carlo calculation for SIRIUS-M cantilevered test module.

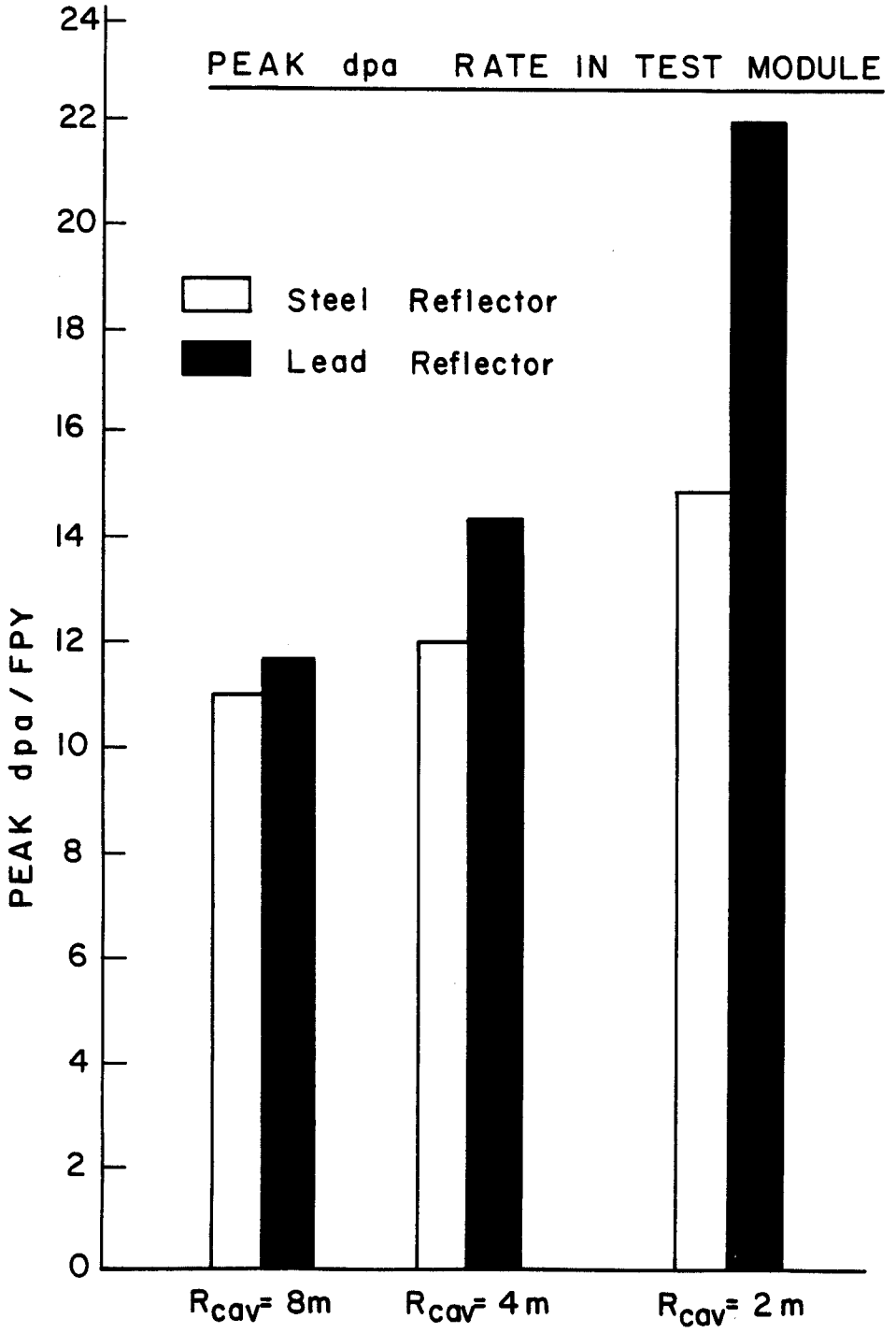

Fig. III.3.3. Effect of cavity radius and reflector material on peak dpa rate in test module.

III.4 Neutronics Analysis for the Final SIRIUS-M Materials Test Module Design

III.4.1 Geometrical Configuration and Material Composition

Thirty-two laser beams are used to uniformly illuminate the target in SIRIUS-M. The 32 beams are equidistantly distributed around the spherical chamber. The beam arrangement is based on a twenty sided icosahedron, where the sides are equilateral triangles superimposed on a spherical surface. The 32 equidistant points on the sphere come from the centers of each triangle (20) plus the vertices where the triangles meet (12). The materials test module must fit between the beam ports. For a cavity radius of 2 m and f/10 final optics, the laser beam radius is 10 cm at the first wall. A 13 cm radius beam port is used to account for the required beam port structure. Using the icosahedron configuration the distance between the centers of any two adjacent beam ports was determined to be 1.2 m resulting in a 0.7 m^2 circular module fitting between two beam ports. A larger test module can fit between three beam ports as shown in Fig. III.4.1. Such a module has a front surface area of 1 m^2. This represents 2% of the solid angle seen by the target. SIRIUS-M utilizes two such modules located at the opposite sides of the chamber.

The test capsules are 5 cm in diameter and 20 cm in length. They are placed perpendicular to the front surface of the module. Each module uses 217 capsules providing 85.4 liters of test volume. This represents 40% of the 213.5 ℓ module volume. The capsules are assumed to consist of 50% NaK, which is used as a thermal contact material, and 50% 316 SS, which represents the specimens and capsule structure material. The module structure is assumed to represent 20% of the module volume and is made of HT-9. The helium gas coolant occupies the remaining volume of the test module. Water cooling was not

used because of the increased damage gradients resulting from higher neutron attenuation in water.[4]

The large pressure of the helium coolant (~ 3400 kPa) requires using curved module front surfaces. The test module for SIRIUS-M is designed as two concentric cylinders terminating in two 3 mm thick HT-9 semi-ellipsoidal heads that protrude 8 cm into the chamber. A 2 mm thick graphite liner covers these heads to protect them from the cyclic high heat flux resulting from the target explosion.

III.4.2 One-Dimensional Analysis

One-dimensional coupled neutronics and photonics calculations have been performed to give estimates for the axial variation of power density and damage rate in the test capsules. In these calculations the front surface of the test module is located at a radius of 1.96 cm which represents the average location of the semi-ellipsoidal heads of the module. Three mm thick HT-9 and 2 mm thick C layers are used in front of the module. The test module is followed by a 20 cm thick Pb reflector (90% Pb and 10% HT-9) and a 30 cm thick steel reflector (90% HT-9 and 10% H_2O). The calculations have been performed in spherical geometry using the ONEDANT code with ENDF/B-V cross section data. A point source isotropically emitting neutrons with the SIRIUS-M target spectrum was used at the origin.

Figure III.4.2 gives the axial variation of dpa and helium production rates in the specimens. The peak values for dpa and He produced per FPY are 21.3 and 123.4, respectively. It is clear that the helium production rate drops faster than the dpa rate as one moves towards the back of the module. The He/dpa ratio is 5.8 at the front of the module and drops to 3 at the back.

The average values for the dpa and He appm per FPY are 16.5 and 72.1, respectively.

The peak and average power densities resulting from nuclear heating in the different components of the test module are given in Table III.4.1. Notice that the power density in steel is a factor of ~ 6 higher than that in NaK. This is primarily due to the higher density and larger gamma absorption. Using a 50% NaK and 50% 316 SS composition for the test capsule the power to be removed from a single test capsule is found to be 3.2 kW. The power generated from nuclear heating in each test module is 1.3 MW. These levels of power can be easily removed by the helium gas coolant that occupies 40% of the module volume.

III.4.3 Three-Dimensional Analysis

Three-dimensional neutronics calculations have been performed to determine the damage profiles and testing capabilities of the materials test modules of SIRIUS-M. The continuous energy Monte Carlo code MCNP[14] was used together with cross section data based on the ENDF/B-V evaluation. Because of symmetry only 1/12 of the reactor was modeled for the Monte Carlo calculation with reflecting surfaces surrounding it. A vertical cross section of the geometrical model used is shown in Fig. III.4.3. The front surface of the test module is at a radius of 1.96 m and has in front of it 3 mm thick HT-9 and 2 mm thick graphite layers. A 0.4 m thick Pb reflector is used in the reactor and backed by a 0.3 m thick steel reflector. The 2.5 cm thick protective tile used in front of the reflector is included in the model. Also included are the 10 cm radius laser beam penetrations. Three such penetrations surround the test module with 120° azimuthal angle spacing. A horizontal cross section at Z = 2 m is shown in Fig. III.4.4. The part of the test module modeled here

Table III.4.1. Power Density (W/cm^3) in Test Module Components

Component	Peak	Average
HT-9 Module Structure	18.9	13.8
Test Capsule:		
316 SS	18.9	13.8
NaK	3.4	2.3

is divided into 10 zones as shown in Figs. III.4.3 and III.4.4. This allows investigating the impact of the beam penetrations on the azimuthal variation of damage in the test module. Each zone is divided into six axial segments to determine the axial damage variation. A point source emitting neutrons isotropically with the SIRIUS-M target spectrum is used at the origin. To get statistically adequate estimates for the damage in the module, an angular source biasing technique was used in which 90% of the source neutrons are forced to impinge directly on the module and the statistical weight of the source is modified for the final estimates to be unbiased. One hundred thousand histories were used in the calculation leading to statistical uncertainties less than 5% in the calculated damage rates for each segment.

Table III.4.2 gives the peak and average damage rates in the 10 zones of the test module. Values averaged over the front 2 cm of each zone were used to represent the peak values. It is clear that no significant radial or azimuthal variation in damage occurs and the results are essentially the same within the statistical uncertainty of the calculation. Since the source

Table III.4.2. Dpa and Helium Production Rates in Different Test Module Zones

Zone	dpa/FPY		He appm/FPY	
	Front Segment	Average	Front Segment	Average
1	21.8	16.9	127.4	77.2
2	21.6	16.6	136.0	76.2
3	22.8	16.6	125.8	71.9
4	20.1	16.3	120.3	77.6
5	22.3	16.8	129.8	76.3
6	23.5	17.0	142.8	82.5
7	21.5	16.1	125.0	74.7
8	21.9	16.4	130.5	73.3
9	21.1	16.6	121.1	75.5
10	21.4	17.0	125.6	77.1
Average over zones 1-5	21.6	16.6	127.9	75.8
Average over zones 6-10	21.9	16.6	129.0	76.6
Whole module	21.8	16.6	128.7	76.4

neutrons are emitted from a point source at the origin, no source neutrons will impinge directly on the side of the module near the penetration. Only lower energy secondary neutrons reflected from the reflector will stream into the penetration and produce more damage in the zones of the test module adjacent to the penetration. This effect is counterbalanced by the higher probability of neutrons being reflected back into the module by the adjacent Pb reflector in zones not adjacent to the penetrations. This leads to a more uniform azimuthal damage variation. The radial variation is also nearly uni-

form due to two competing effects. The additional secondary neutrons impinging on the sides of the protruding part of the module and the reflection from the Pb reflector surrounding the rest of the module tend to produce more damage in the outer zones of the module. This is almost counterbalanced by the lower probability that neutrons leaking from the sides of the protruding part of the module be reflected back into the module.

The peak dpa and helium production rates in the module were calculated to be 24 dpa/FPY and 145 He appm/FPY, respectively. The lowest values at the back of the module are 12 dpa/FPY and 36 He appm/FPY. Hence, the dpa and He production rates drop by factors of 2 and 4, respectively as one moves from the front to the back of the module. This is a modest drop compared to that in MCF test facilities[4,5] where the dpa rate drops by factors of 4-7 and the He production rate drops by factors of 7-15. This is related to the geometrical differences between ICF and MCF test facilities discussed in Section III.2. The peak to average dpa rate ratios in SIRIUS-M, TASKA and TASKA-M are 1.43, 1.56 and 2.74, respectively. The corresponding values for the He production rate are 1.9, 2.16 and 3.72, respectively. The small axial variation of damage in SIRIUS-M suggests that longer test capsules can be utilized in ICF test modules.

Another way of expressing the damage in the test specimens is to sum the product of the damage level times the volume of the test zone that can produce that damage level. This parameter accounts for the number of specimens that can be irradiated to high levels. It can be calculated by multiplying the average damage level by the total capsule volume in the module. This number reflects the total space available not only for specimens but also for temperature, stress, and environmental control. We have assumed that SIRIUS-M will

Table III.4.3. Dpa-ℓ Values per FPY of Operation in Different Facilities

Neutron Production Mode	Device	
Accelerator	RTNS-II	0.0003
Accelerator	FMIT	5
Tokamak-Magnetic	INTOR	182
Mirror-Magnetic	TASKA-M	530
Mirror-Magnetic	TASKA	1510
Laser-Inertial	SIRIUS-M	2840

operate for 10 calendar years at 50% availability. The three-dimensional results were used to determine the values for the volume integrated damage accumulated at the end of life of the device. The total dpa-ℓ value obtained in the two test modules of SIRIUS-M is 14,200. The corresponding He appm-ℓ value is 65,250. Table III.4.3 gives a comparison between the values of dpa-ℓ obtained per FPY of operation for SIRIUS-M, the proposed MCF test facilities (INTOR, TASKA and TASKA-M), and the high energy neutron source test facilities (FMIT and RTNS-II). The dpa-ℓ figure of merit in SIRIUS-M is a factor of 1.9 higher than that in TASKA and much higher than the corresponding values in the other test facilities.

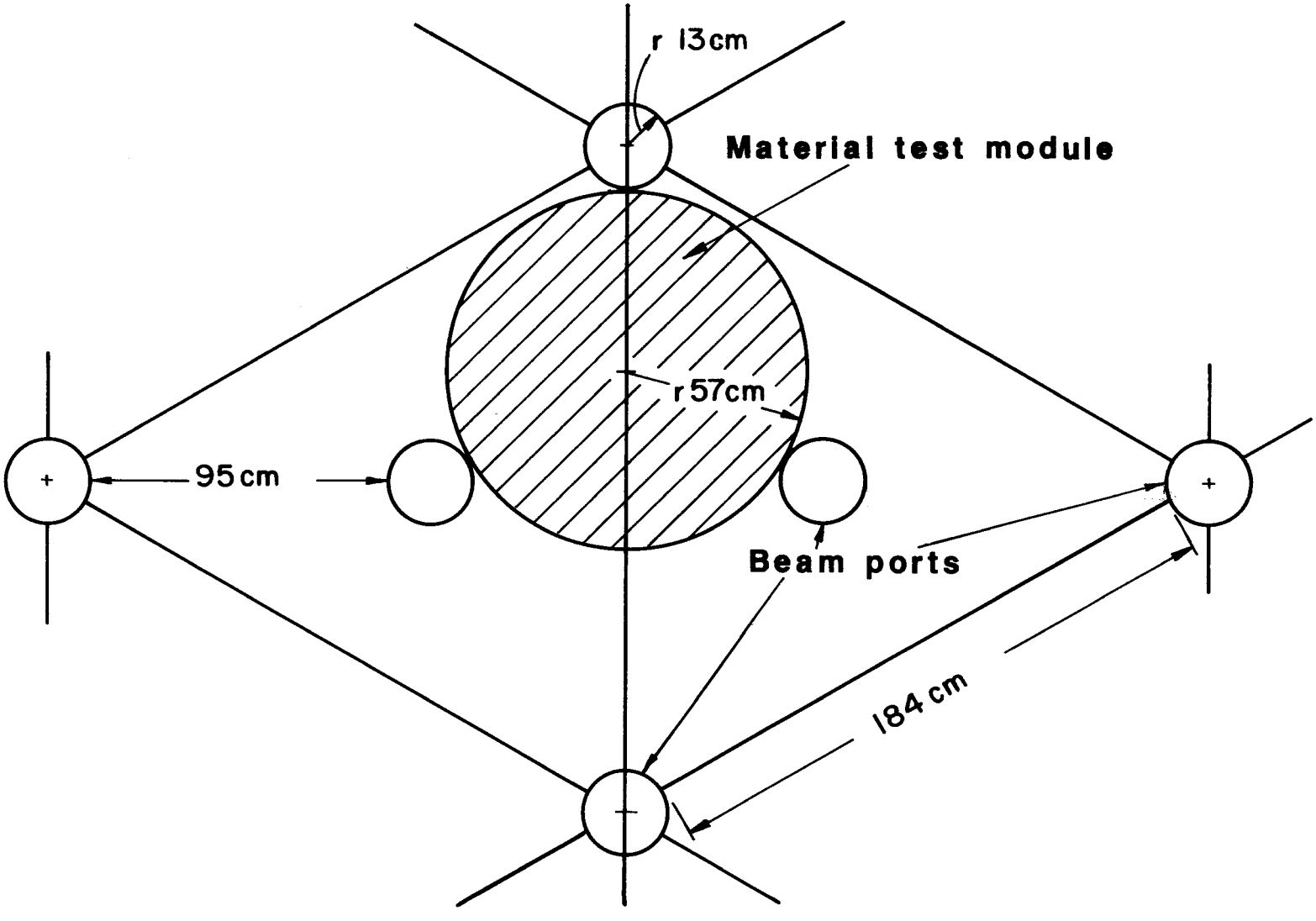

Fig. III.4.1. Two adjacent tiles with beam ports and materials test module.

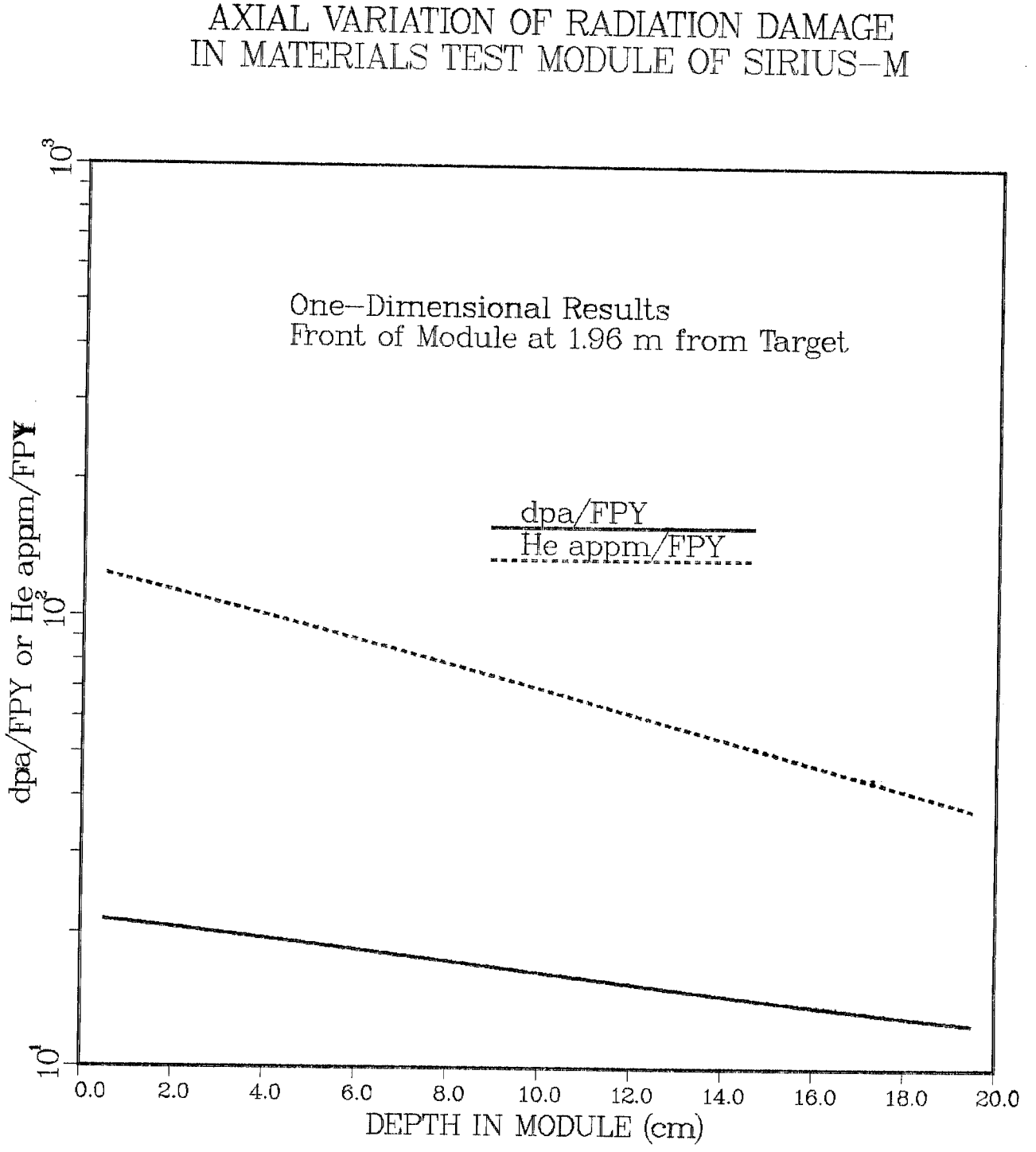

Fig. III.4.2. Axial variation of dpa and He production rates in the test capsule.

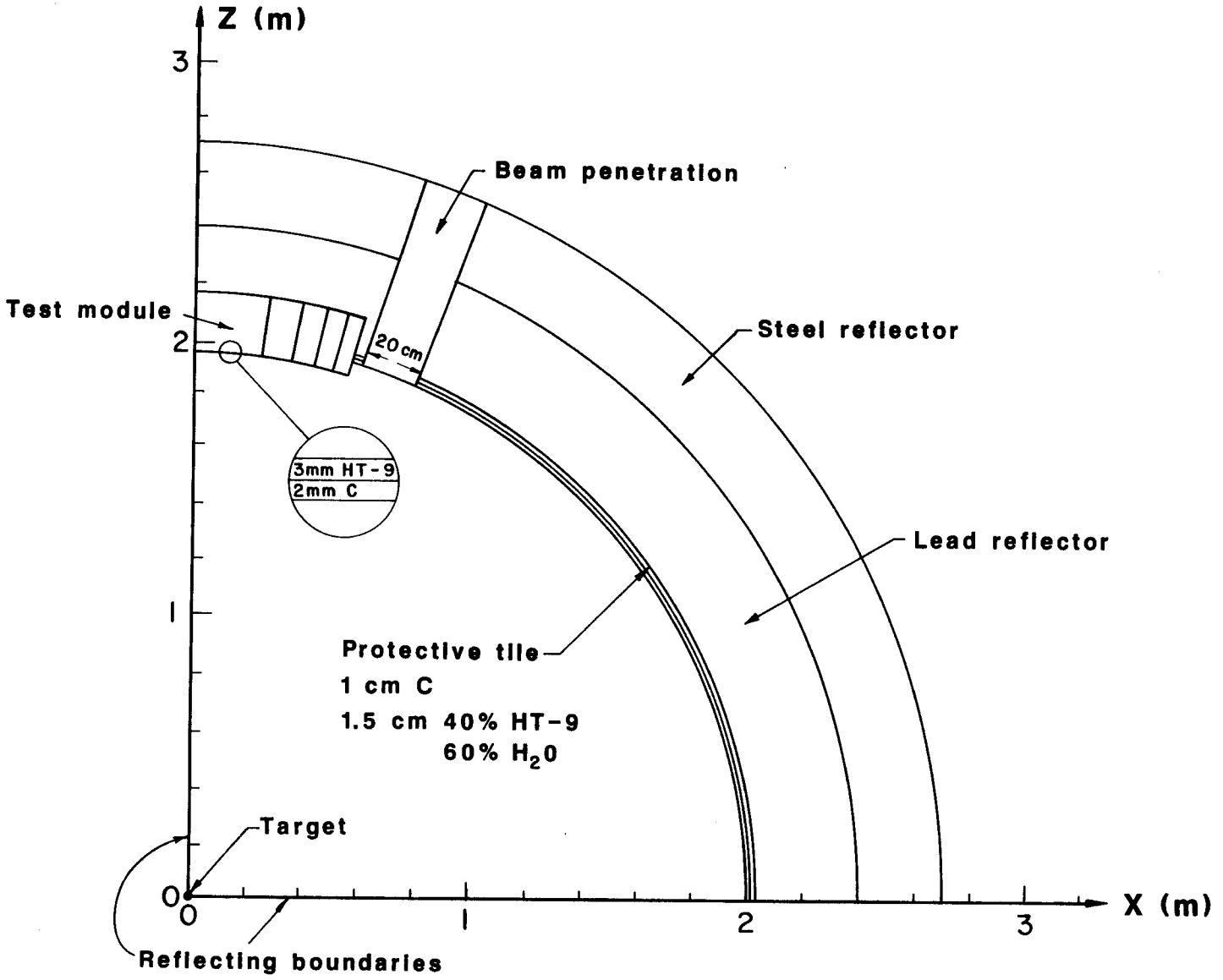

Fig. III.4.3. Vertical cross section of the calculation model.

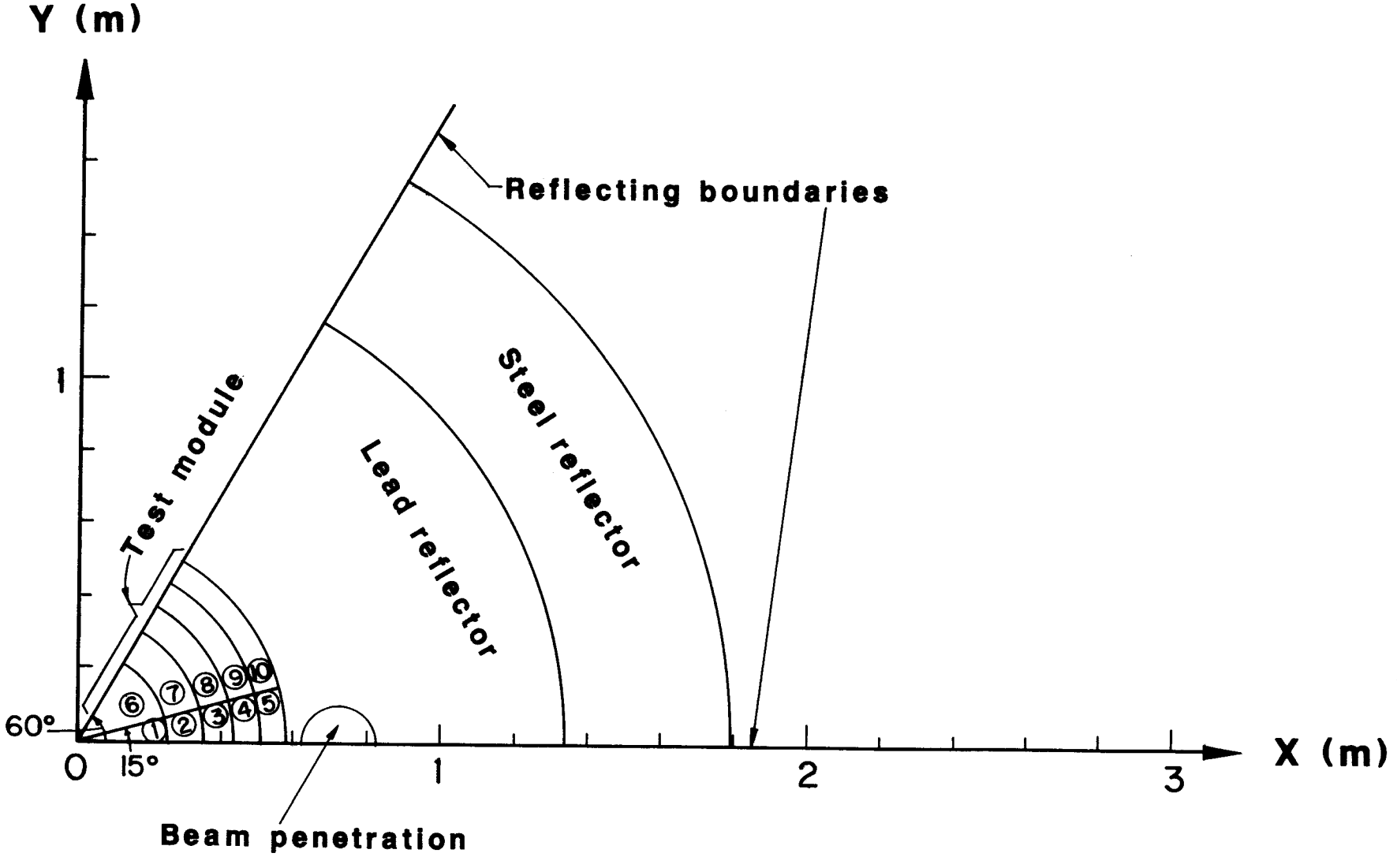

Fig. III.4.4. Horizontal cross section of the calculation model at Z = 2 m.

III.5 Conclusions

Geometrical and spectral differences between ICF and MCF reactors result in a larger damage in the first wall of MCF facilities but a smaller damage gradient in the test modules of ICF facilities. When the time structure of the damage produced is added to the other effects, it is clear that materials information generated to meet MCF applications may not be adequate to determine their behavior in ICF environments and a dedicated ICF materials test facility such as SIRIUS-M is needed.

Several parametric studies have been performed for the SIRIUS-M test module. Using a 2 mm thick graphite liner in front of the module reduces the peak dpa rate by only 2.4%. Using a lead reflector surrounding the test module with a chamber radius of 2 m was found to double the achievable damage level in the test module compared to a cantilevered test module design where a steel reflector is located 8 m from the target.

Two circular test modules are used in SIRIUS-M. Each module has a front surface area of 1 m^2 and fits between three beam ports. No significant radial and azimuthal damage variation in the module results from these penetrations. The peak dpa rate is 24 dpa/FPY yielding a peak accumulated damage of 120 dpa at the end of life of the SIRIUS-M facility. A total volume integrated damage figure of merit of 11,360 dpa-ℓ can be achieved in SIRIUS-M.

References for Chapter III

1. T.M. Batzer et al., "Conceptual Design of a Mirror Reactor for a Fusion Engineering Research Facility (FERF)," UCRL-51617, Aug. 1974.

2. B. Badger et al., "TETR - A Tokamak Engineering Test Reactor to Qualify Materials and Blanket Components for Early DT Fusion Power Reactors," UWFDM-191, 1977.

3. "INTOR - International Tokamak Fusion Reactor, Phase I Report," International Atomic Energy Agency, Vienna, 1982.

4. B. Badger et al., "TASKA - A Tandem Mirror Fusion Engineering Test Facility, KfK-3311/2, UWFDM-500, June 1982.

5. B. Badger et al., "TASKA-M, A Materials Test Reactor for the 1990's," KfK-3680, UWFDM-600, 1983.

6. J. Doggett et al., "A Fusion Technology Demonstration Facility (TDF)," UCRL-90824, 1984.

7. T. Kawabe, to be published.

8. J. Hovingh, "Analysis of a Laser-Initiated, Inertially-Confined Reactor for a Fusion Engineering Research Facility (LA FERF)," UCRL-76517, May 1975.

9. G. Velarde et al., "Neutron Damage, Tritium Production and Energy Deposition in Two Different Cavity Designs for ICF Systems," proceedings of the 13th SOFT Meeting, Varese, Italy, Sept. 1984.

10. E. Simonen, N.M. Ghoniem and N.H. Packen, J. Nucl. Mat. 122 & 123, 391 (1984).

11. E.H. Lee et al., J. Nucl. Mat. 123, 123 (1983).

12. J.A. Sprague and F.A. Smidt, Jr., NRL-Memorandum Report 2629, Naval Research Laboratory (1973).

13. R. O'Dell et al., "User's Manual for ONEDANT: A Code Package for One-Dimensional, Diffusion-Accelerated, Neutral Particle Transport," LA-9184-M, Los Alamos National Lab. (Feb. 1987).

14. "MCNP - A General Monte Carlo Code for Neutron and Photon Transport," LA-7396-M, Los Alamos National Lab. (1981).

IV. TARGET DESIGN AND BEAM TRANSPORT CONSIDERATIONS

IV.1 Tolerance for Irradiation Nonuniformity in Direct-Drive Laser-Fusion Reactors

A crucial issue for the direct-drive approach to laser fusion is whether adequate irradiation uniformity on target can be achieved in a reactor situation. Work performed by the University of Rochester Laboratory for Laser Energetics (UR) as part of this contract represents a first step in determining tolerance levels for uniformity. The work falls into two categories: (1) determining the nature of the nonuniformities produced by different laser-target imperfections, and (2) determining how much of each kind of nonuniformity a target can tolerate. Nonuniformities produced by energy imbalance among the different beams and by poor beam quality were examined, in part, last year using a beam ray-trace code that treats the three-dimensional geometry of the laser configuration and includes refraction of the rays through the plasma atmosphere surrounding the target. One constraint on those calculations was that the numerical method required all beams to pass through the target center. That constraint has now been removed, permitting examination of nonuniformities produced by errors in pointing the beams, which is the subject of this year's work. Tolerances for the beam mispointing are estimated by using the University of Rochester's two-dimensional hydrocode ORCHID to calculate the degradation in target performance produced when the SIRIUS-M target is irradiated by nonuniformities characteristic if mispointing.

Typical numbers associated with errors in beam pointing are shown in Fig. IV.1.1. For the 32-beam SIRIUS-M reactor, with beams subtending 2% of the target-chamber surface, the final optical element will be 21 meters from the

target. As an example, consider a pointing error with the beam axis striking the target off center, at a distance of 5% of the target radius. For a 2 mm target, this is a distance of 10^{-4} m, which corresponds to a point error of 5 μrad. For reference, the OMEGA laser system at the University of Rochester presently achieves a pointing accuracy of about 10 μrad. It should be possible to attain considerably better accuracy in future systems.

We have calculated the amount of nonuniformity produced when each beam is assigned a random pointing error up to a specific maximum amount. The resulting rms nonuniformity is shown in Fig. IV.1.2 for smooth (quadratically shaped) beam profiles, focused tangentially (i.e., each beam would subtend an entire target hemisphere if correctly pointed). The conversion to microradians is indicated for both f/5 and f/10 optics. The error bar characterizes the variation in nonuniformity for different combinations of pointing errors among the individual beams. A 1% nonuniformity is characteristic of the maximum that a target can tolerate.

The target response to irradiation nonuniformity depends on not only the magnitude, but also on the spatial wavelength of the nonuniformity. For instance, short wavelength nonuniformities can be smoothed by thermal conduction once an adequate plasma atmosphere has been established. Longer wavelength nonuniformities will not be smoothed significantly, but neither will they grow substantially within the target by hydrodynamic instabilities.

To characterize the spatial variation of the nonuniformity, we have decomposed it into spherical harmonics. An example is shown in Fig. IV.1.3 which displays the rms nonuniformity σ_ℓ in the first 14 spherical harmonic modes ℓ. (The total rms nonuniformity is related to σ_ℓ by $\sigma = \left(\sum \sigma_\ell^2\right)^{1/2}$.) The first column of σ_ℓ shows the modal decomposition for perfect beam pointing

and perfect energy balance among the beams. The next column shows the effect of random pointing errors for the beams, with no error exceeding 11 μrad for f/5 optics (or 5 μrad for f/10 optics). The effect of the mispointing is to create long wavelength nonuniformities ($\ell \leq 4$). For comparison, the effect of energy imbalance among the beams (but perfect pointing) is shown in the last column. The effect is similar.

A summary of our results characterizing the spatial wavelength of nonuniformities from different sources is shown in Fig. IV.1.4. Pointing error and energy imbalance affect the first four modes. Beam overlap for a 32-beam system predominantly produces modes between 8 and 12 for smooth beam profiles. Nonsmooth profiles will create the total spectrum of nonuniformities, usually dominated by short wavelength modes.

As a first step to establishing tolerances for beam pointing, we have simulated the effects of long wavelength irradiation nonuniformities (ℓ = 2 and 4) on the SIRIUS target using the 2-D hydrocode ORCHID. Results in Fig. IV.1.5 show how the target gain is reduced as the magnitude of the nonuniformity is increased. (A 4% peak-to-valley amplitude corresponds to about 1% rms.) To have less than a 5% reduction in gain, the nonuniformity must be less than about 0.5% rms. From Fig. IV.1.3, we see that this level can be achieved with a pointing error somewhat less than 10 μrad for f/5 optics or less than 5 μrad for f/10 optics.

Since these tolerances are about at the level of present day technology, these calculations suggest that beam-pointing accuracy should not be a serious problem for a direct-drive reactor.

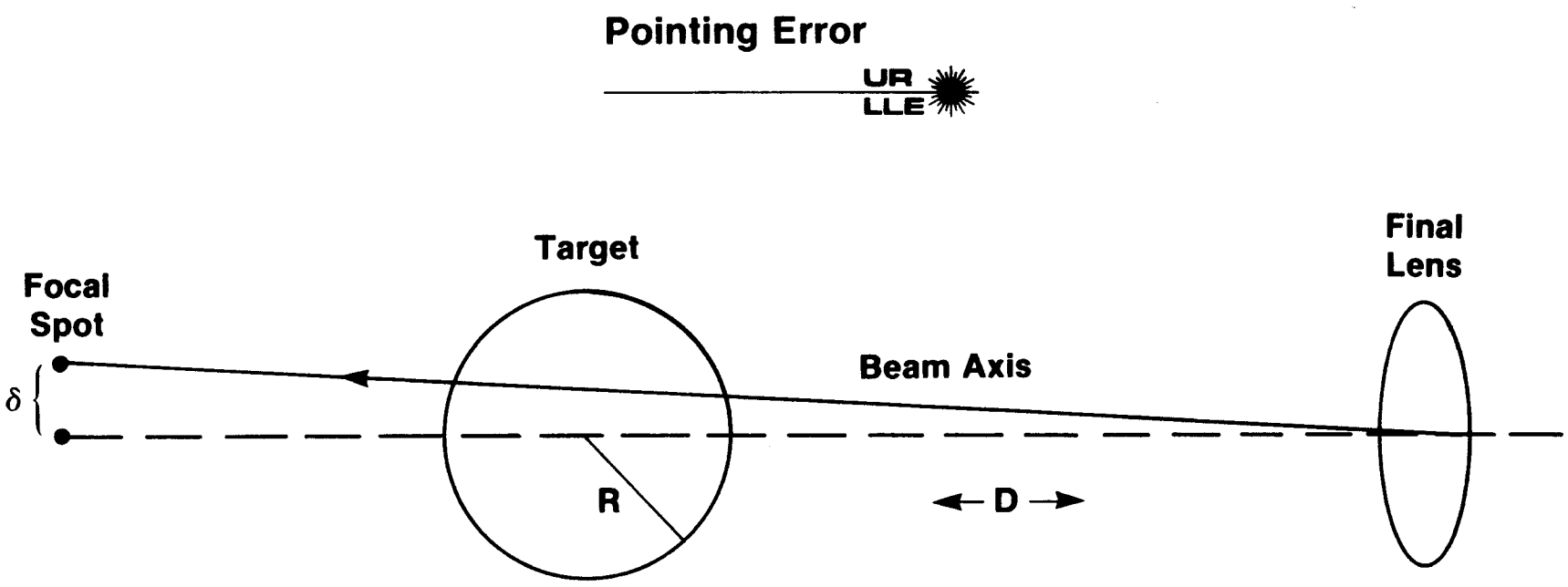

TC1735

Fig. IV.1.1. Characteristic numbers for beam-pointing error in the SIRIUS reactor.

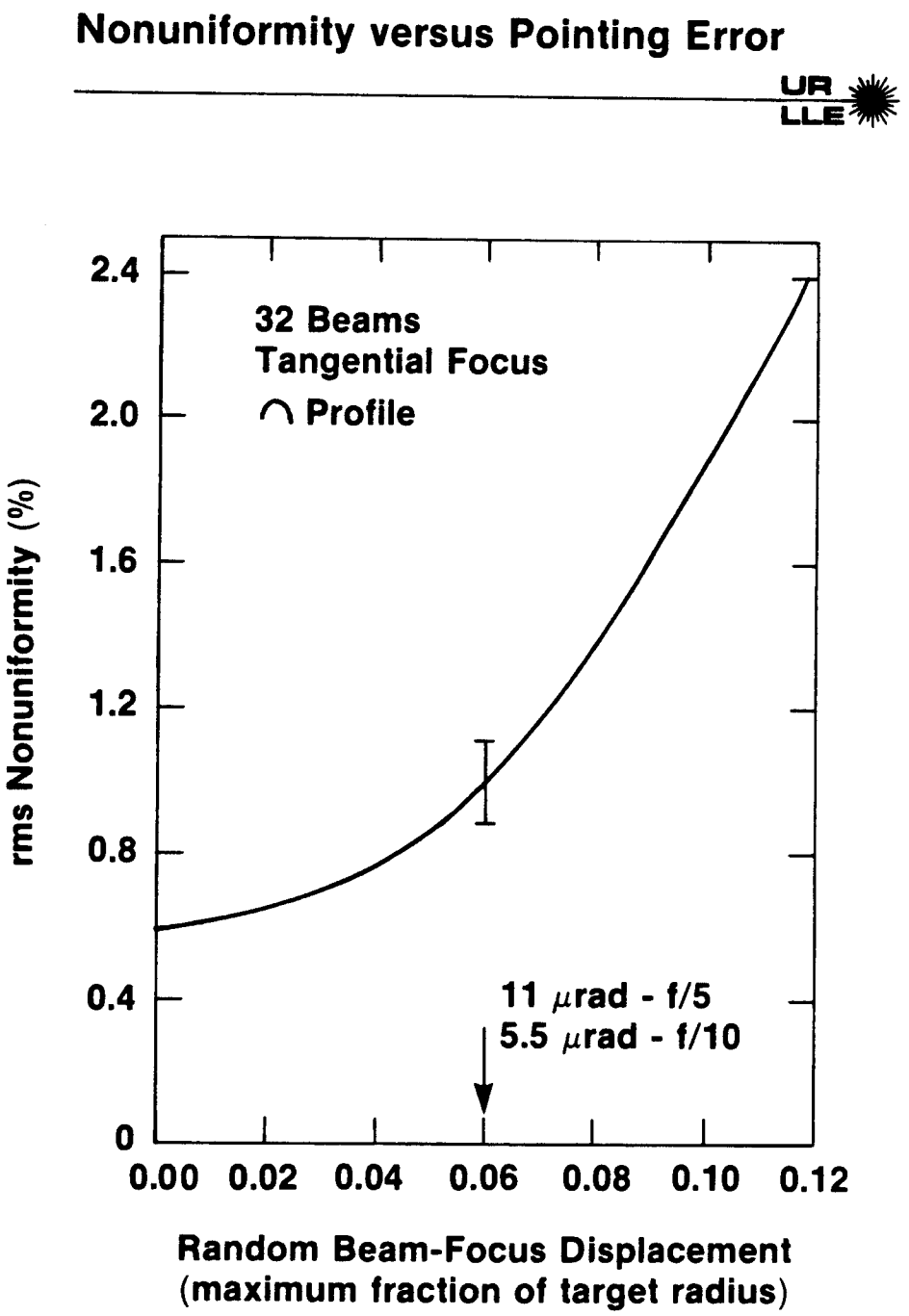

TC1731

Fig. IV.1.2. Nonuniformity produced by random pointing errors among the beams, with the maximum deviation shown on the x-axis.

Pointing Error and Beam Energy Imbalance Produce Similar Effects

UR LLE

Root-Mean-Square Nonuniformity (%)*

Spherical Harmonic Mode (ℓ)	Uniform	Random Pointing Error (11 μrad max)	Random Energy Imbalance (5% max)
1	–	0.36	0.36
2	–	0.38	0.53
3	–	0.39	0.21
4	–	0.27	0.11
5	–	–	–
6	0.10	0.10	0.10
7	–	–	–
8	–	–	–
9	–	–	–
10	0.25	0.25	0.25
11	–	–	–
11	–	–	–
12	0.13	0.13	0.13
13	–	–	–
14	–	–	–
TOTAL ($\ell \leq 32$)	0.6%	1.0%	0.9%

* 32 beams; f/5 lens; focus ratio = 1; /\- profile.

Fig. IV.1.3. Spherical harmonic decomposition of the nonuniformity produced in three cases: (a) perfect beam pointing and perfect energy balance; (b) random pointing error but perfect energy balance; and (c) perfect beam pointing but random energy imbalance among the beams with a maximum deviation of 5%.

Summary of Uniformity Calculations

UR LLE

$\ell = 1$–4

- Pointing error
- Energy imbalance

$\ell = 8$–12

- Beam overlap (24–32 beams)

$\ell \gtrsim 8$

- Beam imperfections

TC1733

Fig. IV.1.4. Summary of the spatial wavelengths (spherical harmonic modes) characteristic of different irradiation nonuniformities.

Yield Reduction versus Illumination Perturbation for 1.6-MJ Pellet Design

UR LLE

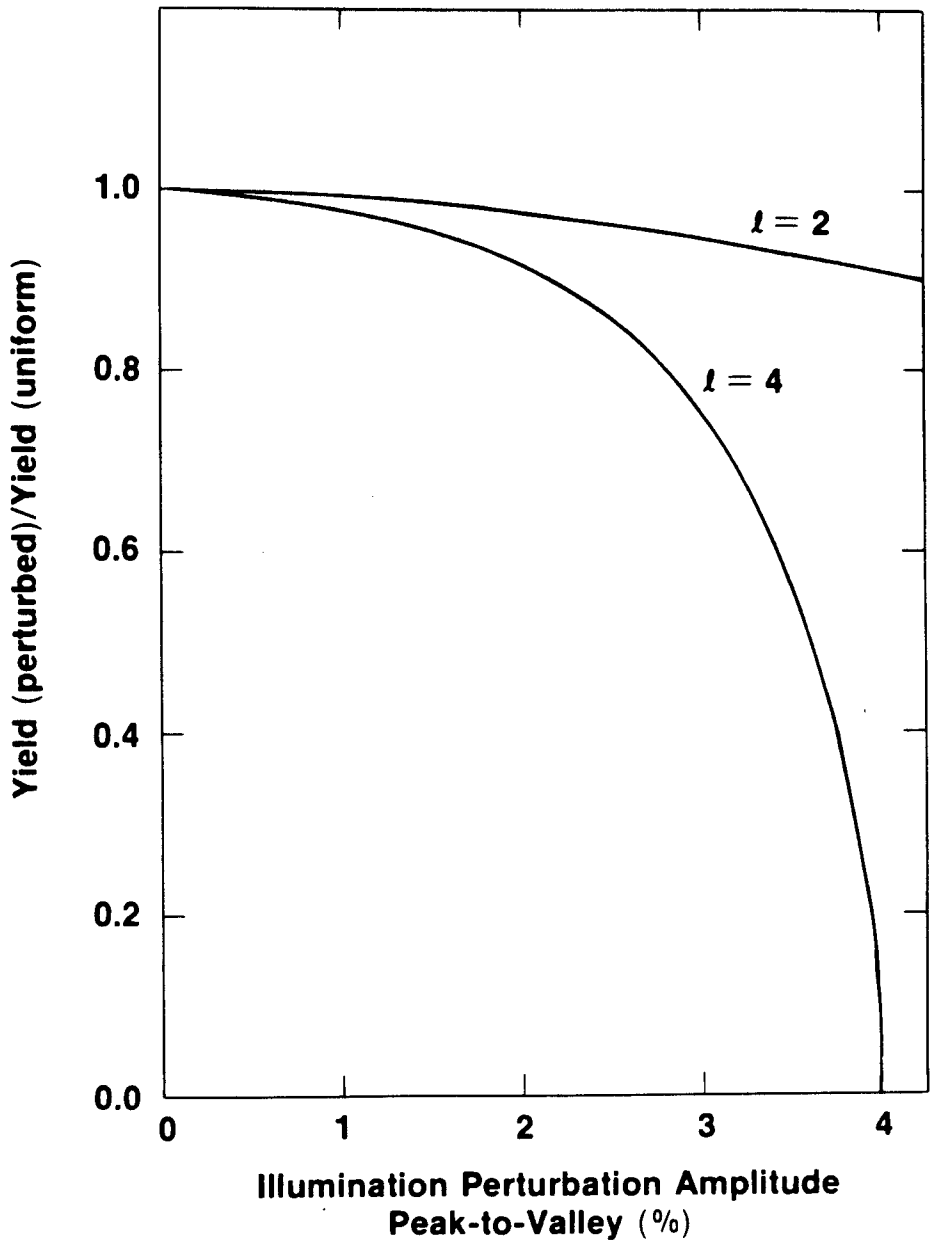

TC1722

Fig. IV.1.5. The degradation in target yield with increasing irradiation non-uniformity for the long wavelength modes characteristic of beam mispointing or energy imbalance.

IV.2 Implementation of Induced Spatial Incoherence in the SIRIUS-M Reactor System

Theoretical studies have shown that acceptable spherical illumination uniformity can be achieved by overlapping a limited number of beams (> 20), provided that each individual beam profile is smooth and reproducible.[1-3] However, previous efforts to obtain such profiles have been frustrated by the inherent imperfections in high power laser systems. The cumulative effect of small phase and amplitude aberrations (both linear and nonlinear) introduced by each optical element of a multi-stage laser is to produce large random nonuniformities in the output intensity. In order to produce the desired irradiance and spot size with a lens of reasonable focal length, one normally places the pellet in the quasi near-field of that lens, rather than at the focus; as a result, the laser nonuniformities tend to be mapped onto the pellet.[2] Efforts to control laser aberrations using ultra-high quality optics and extensive beam relaying have not been completely successful, especially at high energies and shorter laser wavelengths.[4]

The induced spatial incoherence (ISI) technique presents a novel way of achieving a smooth and controllable beam profile.[5] The concept is illustrated in two dimensions in Fig. IV.2.1. Spatial incoherence is created by propagating a laser beam of broad bandwidth $\Delta\nu$ through an echelon structure that imposes different optical delays upon different transverse sections. By choosing the delay increments Δt somewhat larger than the optical coherence time $t_c = 1/\Delta\nu$ (and the total time delay much smaller than the pulse width) one slices the beam into a large number of nearly simultaneous but incoherent beamlets, each of which focuses to the same smooth far-field diffraction profile. Although superposition of these beamlets will produce a complicated

interference pattern at any instant of time, that pattern evolves randomly in times of order t_c. The pellet surface will effectively ignore this rapidly shifting structure if the hydrodynamic response time t_h is much larger than t_c, i.e. it responds only to the superposition of the intensity profiles. For example, a bandwidth $\Delta\nu = 30\ cm^{-1}$ (easily achieved with the KrF laser) provides $t_c = 1$ ps, whereas t_h is typically $\simeq 1000$ ps.

The ISI concept can be easily extended to three dimensions by using two perpendicular echelons constructed so that the time delay increment introduced by each step of one of them is slightly larger than the total delay increment across the other. This configuration offers considerable flexibility in controlling the shape of the beam profile. For example, the diffraction pattern can be smeared out and broadened by tilting alternating echelon steps to slightly different aiming angles (Fig. IV.2.2), or slightly decreasing the distance from the lens to the pellet.

The diffraction profile is not very sensitive to intensity or phase aberrations on the incident beam; the beam need only be approximately uniform over the small width of each beamlet. Numerical simulations indicate that each echelon should have $N_s \geq 3\ N_a$ steps to adequately handle a beam aberrated to $N_a \times$ diffraction limit.

Some concerns regarding the implementation of ISI in a reactor-based system such as SIRIUS-M are addressed here. We have investigated the pellet illumination uniformity that can be realistically expected using the ISI technique. Also, the problem of applying the ISI optics to reactor size systems has been studied.

The illumination uniformity resulting from ISI laser beams incident on laser-fusion pellets has been studied for the SIRIUS-M 32-beam configuration.

A variety of beam shapes and sizes is produced by changing the smear (tilting the echelon steps) and spot size of the diffraction profile (Fig. IV.2.2). The optimum configuration can then be selected. A computer code has been constructed to perform beam ray tracing calculations in the spherical pellet plasmas. The plasma density and temperature profiles are calculated by the NRL FAST1D hydrocode simulation.[6] Energy is deposited by inverse bremsstrahlung absorption, and is weighted by a different amount (depending upon where the absorption takes place) to account for its contribution to the ablation pressure.[7] The ray tracing and energy deposition is done at four different times during the implosion, and the illumination distributions are calculated at each time. The resulting parameters (peak-to-valley energy absorption, total absorbed energy, etc.) are then averaged over the different times. The results of these calculations are shown in Fig. IV.2.3, where the peak-to-valley uniformity and total beam energy absorption are plotted as functions of the beam spot size a and spread distance $\delta a/a$. (RMS values were also calculated for these distributions, and are smaller than the peak-to-valley values by factors of 4 to 6.2.) The goals of high energy absorption and low nonuniformity are somewhat conflicting, but better than 2% peak-to-valley uniformity and 75% total beam energy absorption are simultaneously possible.

Because the time averaging is done after the peak-to-valley values are found, these values neglect phase effects, where peaks (valleys) at one time are washed out by valleys (peaks) that occur in the same location at a later time. Inclusion of this effect would improve the uniformity values. Likewise, the uniformity at a particular time can be better than the time average.

The effect of beam misalignment errors on the illumination uniformity has also been examined. Broader and larger beam profiles are less sensitive to misalignment errors, but tend to result in less total energy absorption on the pellet. Figure IV.2.4 shows the maximum nonuniformity calculated as a function of the beam misalignment, measured in microns and as a percentage of the initial pellet radius r_0. The pellet examined here has a radius of 0.363 cm, but results are independent of the pellet size if the misalignment error is normalized to the pellet radius. The misalignment error is randomly directed on the pellet surface, and its magnitude varies randomly between zero and the maximum shown. The uniformity levels shown here are constrained so that the absorbed beam energies are greater than a given amount -- 60% to 75% in the results presented here. Allowing less absorption can improve the uniformity somewhat, but the increase is relatively small; in general, the nonuniformity increases about 1.5% for every percent increase in $\Delta x/r_0$.

The spectral structure of the illumination is as important as the magnitude of the peak-to-valley nonuniformity. The energy absorption distributions calculated previously are separated into their component spherical harmonic modes. The largest mode (of all possible m values) is found as a function of the frequency ℓ. Figure IV.2.5 shows the largest amplitude modes at different wavelengths as the misalignment is increased. Significant differences occur only in the lowest order (long wavelength) modes, $\ell \leq 4$.

In summary, we have shown that both good uniformity (peak-to-valley variations $\leq$ 2%) and high beam absorption ($\simeq$ 75%) are simultaneously possible using ISI type illumination profiles on laser-fusion pellets. Random misalignment errors degrade these values somewhat; we find that the nonuniformity is increased about 1.5% for every percent increase in the relative misalign-

ment error (measured as a percentage of the target radius). Maximum mode amplitudes are kept below 1% if the relative misalignment error is less than about 2%.

Next, we consider the implementation of the ISI technique in a large reactor system, such as SIRIUS-M. There are several options for incorporating the ISI optics into the drive beams. Figure IV.2.6 shows one such possibility, which takes explicit account of the fact that KrF lasers are likely to require angular multiplexing, and therefore produce an array of output beams. We assume a 16 channel array of 30 cm square beams, giving a total aperture of 120 × 120 cm^2. For an average fluence of 2.5 J/cm^2 (approximately 1/2 the measured damage threshold for 0.25 μm optics[8]) and a 32 beam spherical illumination system, this configuration produces 1.15 MJ on target. In Fig. IV.2.6, each channel is independently sliced into a 60 × 60 array of D_1 = 5 mm square beamlets by the echelons, then focused onto the target by the lens (f = 30 m) and planar turning mirror arrays. The resulting $sinc^2$ far field diffraction pattern has a half-width $a = f\lambda/D_1 \simeq 1.5$ mm (peak to first zero), which can be smeared out to cover a 2 mm radius target by a combination of the two techniques described previously. With 60 steps per channel, the echelons should produce smooth and reproducible target illumination, even with KrF drivers aberrated up to 20 times the diffraction limit. The turning mirrors serve only to isolate the more expensive optical components from target neutrons, and should be placed as close as possible to the lenses. Although neutron damage to these mirrors is inevitable, it will be minimized by the large focal distance (f = 30 m) to the target. An alternative scheme, which replaces the mirrors by prisms, will be discussed below.

Because the ISI echelons are placed in each of the 16 channels, they must be as simple and inexpensive as possible, and require minimal adjustment. These constraints dictate the use of transmissive optics in both the horizontal and vertical directions. With any reasonable number of steps, however, the echelons would have to be excessively thick along the propagation direction. The smallest differential step thickness must be at least $ct_c/(n - 1) = 1/(n - 1)\Delta\nu$, where n is the refractive index, and the optical bandwidth Δn is measured in cm^{-1}; hence, for N_s steps, the larger echelon must have a thickness $z_{max} > N_s^2/(n - 1)\Delta\nu$. Assuming $N_s = 60$, $n = 1.5$, and $\Delta\nu = 50\ cm^{-1}$, for example, one obtains $z_{max} > 1.4$ m. An echelon of this thickness would not only be expensive and difficult to fabricate, but it could also cause a significant amount of self-focusing in the beamlets. To avoid such problems, we propose a partial ISI scheme, in which the echelon step sequence would be repeated across the aperture, as illustrated in the enlarged views in Fig. IV.2.6. Although this configuration allows the repeated pairs of steps to remain mutually coherent, the resulting stationary interference pattern at the target will have only high spatial frequencies, and can therefore be smoothed out by thermal diffusion in the plasma.

The RMS fractional ablation pressure deviation $\Delta P_{rms}/\langle P\rangle$ due to light from the entire $120 \times 120\ cm^2$ aperture can be estimated using a theory[5,9] that accounts for the statistical properties of the chaotic broadband light, and approximates the thermal diffusion process by the well-known "cloudy day" model.[10] This theory has recently been extended to include the partial ISI case, giving the approximate expression:

$$\frac{\Delta P_{rms}}{\langle P\rangle} \simeq \frac{1}{N_{tot}}\left[\frac{t_c}{T}\sum_{\vec{m}\neq 0}\exp\left(-\alpha|\vec{m}|\right) + \sum_{\vec{m}\neq 0}\exp\left(-N_s\alpha|\vec{m}|\right)\right]^{1/2} . \quad \text{(IV.2.1)}$$

Here, $\alpha = 4\pi\Delta R/a$, ΔR is the effective absorption-ablation distance, T is the averaging time, N_s (= 30) is the number of mutually incoherent steps, N_{tot} (= 60 × 4) is the total number of steps in the entire aperture, and the summations run over all of the integer vectors $\vec{m} = (m_x, m_y)$ (m_x, m_y = 0, ±1, ±2, etc.) excepting $m_x = m_y = 0$.

The first term of Eq. (IV.2.1) describes the residual nonuniformity due to the incoherent beamlets, which decreases with the averaging time. The second term describes the contributions of the high spatial frequency interference patterns, which are "frozen in" because of coherence between repeating sections. For ΔR = 20 μm (a reasonable value for the early part of the KrF pulse) and a = 1.5 mm, one obtains $\alpha = 0.168$ and $N_s\alpha = 5.03$. One can evaluate the incoherent terms by approximating the summation by an integral:

$$\sum_{\vec{m}\neq 0} \exp(-\alpha|\vec{m}|) = \sum_{\vec{m}\neq 0} \exp(-\alpha|\vec{m}|) - 1$$

$$= \int_{-\infty}^{\infty} d\mu_x \int_{-\infty}^{\infty} d\mu_y \exp[-\alpha(\mu_x^2 + \mu_y^2)^{1/2}] - 1 = 2\pi/\alpha^2 - 1 \simeq 223 .$$

The stationary contributions due to partial ISI are negligible in comparison:

$$\sum_{\vec{m}\neq 0} \exp(-N_s\alpha|\vec{m}|) = 4\exp(-N_s\alpha) + 4\exp(-2^{1/2} N_s\alpha) \simeq 0.03 .$$

Substituting these results back into Eq. (IV.2.1) and using N_{tot} = 240, we obtain the pressure nonuniformity

$$\frac{\Delta P_{rms}}{\langle P\rangle} = 0.062 \left(\frac{t_c}{T}\right)^{1/2} ,$$

which is < 0.3% for $T \sim t_h >> t_c$. Additional smoothing (by a factor of ~ 2-3) will be provided by the other overlapping beams in the spherical illumination system.

Figures IV.2.7 and IV.2.8 illustrate the comparison between the pure and partial ISI schemes. They show numerical simulations[9] of the time-averaged plus the average ablation pressure, assuming the "cloud day" model. In both cases, a 20 cm, 5 × diffraction limit beam (λ = 0.527 μm) is incident on the pair of echelons, each of which has twenty 1 cm wide steps. However, in the partial ISI scheme (Fig. IV.2.8) the sequence repeats after the 10th step; i.e. steps 1 and 11, 2 and 12, etc., remain mutually coherent. The resulting increase in very fine scale interference structure is clearly evident at the focal plane, and would persist throughout the entire pulse duration. As a result of thermal smoothing, however, this structure is effectively filtered out. (The difference in peak-to-valley deviation in the two cases is purely statistical.)

The existence of a stationary intensity pattern, even one of high spatial frequency, raises the additional question of possible self-focusing in the underdense plasma. In order to examine this question, we have performed numerical simulations of optical propagation in the corona, using a cartesian 2D propagation-hydrodynamic code SELFOCT. This code accounts for both ponderomotive and thermal self-focusing mechanisms, assumes linearized hydrodynamic response with strong ion-acoustic damping, and ignores convection along the laser propagation axis. To compare the pure and partial ISI cases, we performed identical calculations using echelons with 40 steps. In the pure case, none of the steps were repeated, while in the partial case, two repeated sections of 20 steps were used. The plasma background was typical of a 1/4 μm

laser-produced corona, with an electron temperature of 1.3 keV and a density scale length of 1275 μm. The interaction was studied over a 0.5 cm path length in plasma densities varying between 1% and 50% critical. Although the simulation ran for times $\geq$ 640 ps (assuming a 3.17 ps coherence time) at average intensities of 3×10^{14} W/cm^2, they showed no evidence of self-focusing in either case. Evidently, the averaged intensity distribution, even with the stationary nonuniformities introduced by the repeated steps, was below threshold for self-focusing.

Because the target is located at or very near the far-field of the echelon steps, the illumination profile will be independent of the distances between the echelons and lenses. In principle, one could therefore replace the 16 channel echelon array shown in Fig. IV.2.6 by a single pair of larger echelons located back at the final amplifier, where all of the angularly-multiplexed channels cross. (The step widths would be scaled up by the ratio of the apertures.) This option has the disadvantage that it is likely to produce excessive diffraction of the beamlets in the temporal decoding optics. With Fresnel numbers of order unity, the beamlets would have peak intensities nearly three times the present value at some of the decoding mirrors. They would also be more susceptible to aberration due to thermal gradients in the long air paths, because their total widths (including low intensity "skirts" and side lobes) are increased significantly by diffraction spreading. One possible solution to this problem could be to insert optical relay telescopes in the decoding section of each channel; however, it is not clear whether this would really be more cost effective than the use of multiple echelons.

One of the main issues confronting the use of ISI is likely to be the cost and complexity of the echelons. It is therefore worthwhile to briefly

examine a related scheme proposed by Kato.[11] In this technique, each echelon pair would be replaced by a single easily-fabricated phase plate that produces randomly-phased but coherent beamlets. All of the spatial frequencies of the interference pattern would thus be "frozen in" at the target. (One can obtain some temporal smoothing of the high spatial frequencies by introducing incoherence among the 16 angularly multiplexed channels; however, these nonuniformities are already adequately smoothed by thermal diffusion.) The ablation pressure variation is approximately:

$$\frac{\Delta P_{rms}}{\langle P \rangle} = \frac{1}{N_{tot}} \left[\sum_{\vec{m} \neq 0} \exp(-\alpha |\vec{m}|) \right]^{1/2} \simeq \frac{(2\pi/\alpha^2)^{1/2}}{N_{tot}} \qquad \text{(IV.2.2)}$$

which gives $\Delta P_{rms}/\langle P \rangle = 0.062$ under the conditions specified in the previous paragraph. Even allowing for the additional smoothing factor provided by the other overlapping beams in the spherical illumination system, it appears unlikely that the random phase scheme can achieve adequate uniformity of the ablation pressure, at least in the early part of the pulse where ΔP is small.

Neutron damage to the dielectric coating of the turning mirrors remains a major problem in all of the spherical illumination designs proposed so far. One possible solution is to replace the turning mirrors by thin prisms, which would refract the light along the beam tube axis. Although prisms would be less susceptible to neutron damage, they can introduce chromatic aberration, astigmatism, and coma into the beam. The astigmatism and coma can be avoided by placing the focusing lenses in the beam tube just beyond the prisms; however, this partially defeats the purpose of the beam turning optics. For a thin prism of average deflection angle $\beta \ll 1$, the angular spread due to chromatic aberration is

$$\Delta\beta = \frac{\partial n/\partial\lambda}{n - 1} \beta\lambda^2\Delta\nu \ . \qquad \text{(IV.2.3)}$$

Assuming fused quartz ($n = 1.5$, $\partial n/\partial\lambda = 5.6 \times 10^{-4}$ nm^{-1}), $\Delta\nu = 50$ cm^{-1}, and $\beta = 0.1$, one finds $\Delta\beta = 3.5 \times 10^{-5}$ rad, which would smear the focal spot over a distance $f\Delta\beta \simeq 1$ nm in the incidence plane of the prism. An alternative idea, which would avoid these objections, is to use total internal reflection in a 45° prism. The main drawback to this scheme is the possibility that the 5 mm wide beamlets will begin to self-focus in the 30 cm path through the prism; in fact the calculated nonlinear phase distortion through that propagation path is $B \geq 1$.

BEAM SMOOTHING BY INDUCED SPATIAL INCOHERENCE (I.S.I.)

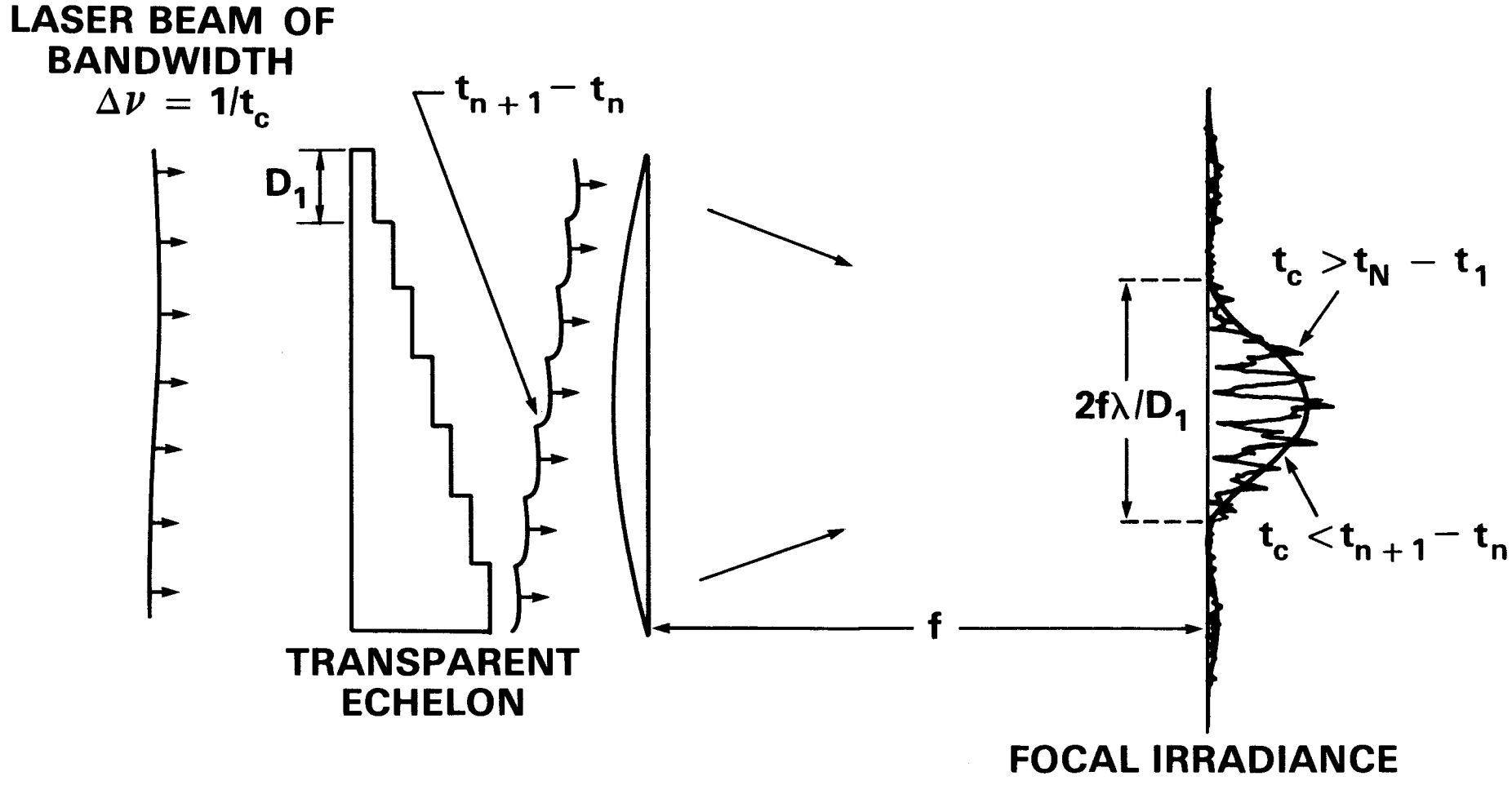

Fig. IV.2.1. Use of spatial incoherence induced by a transparent echelon to smooth the focal spot irradiance of a broadband laser.

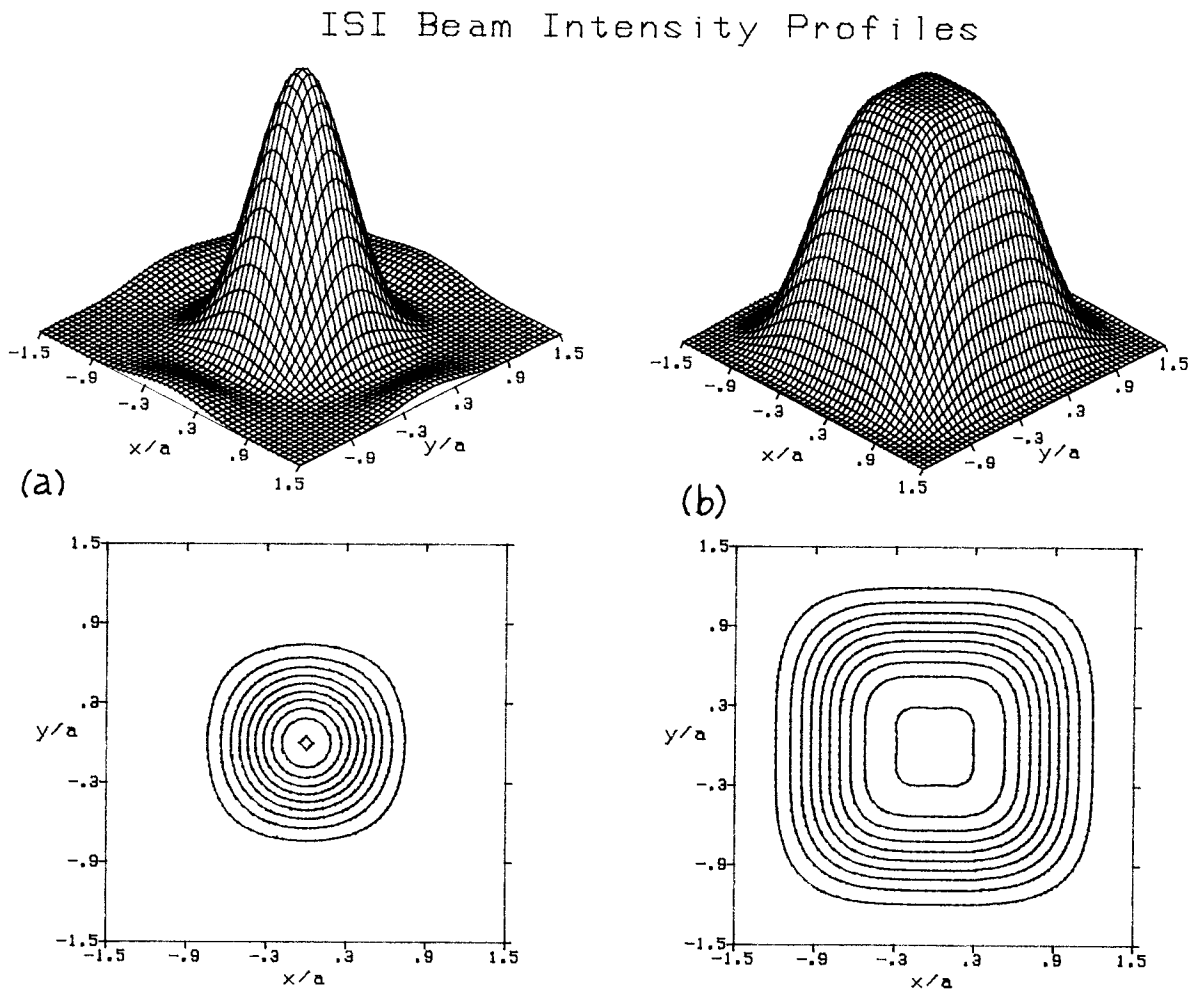

Fig. IV.2.2. Time averaged beam profiles produced with the ISI technique with (a) square echelon steps; and (b) square echelon steps that are alternately tilted relative to one another in the x and y directions. The top figures are isometric plots of the intensity; at bottom are contour plots, with contours at every 10% of peak intensity.

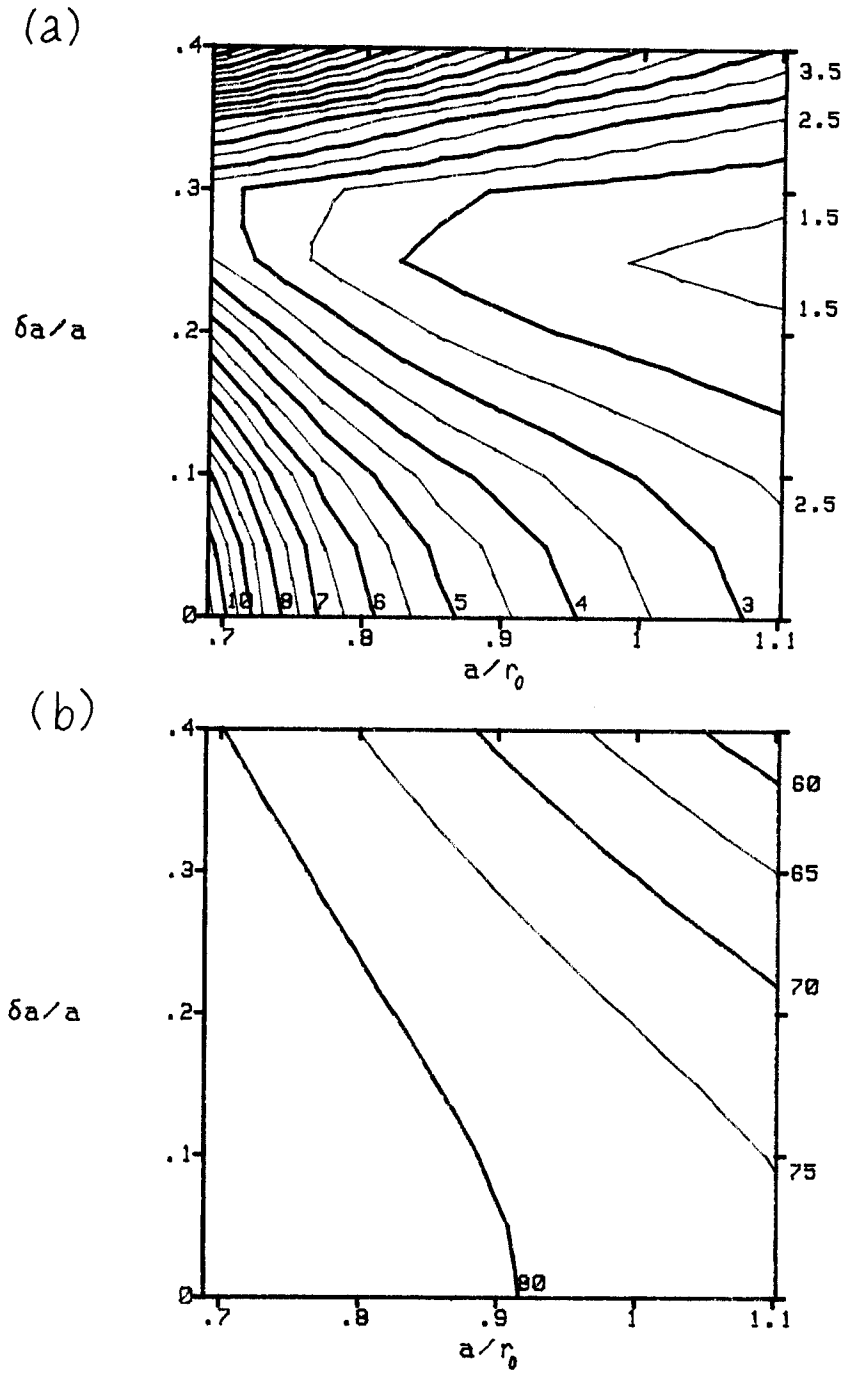

Fig. IV.2.3. Time averaged results of the ray tracing and energy mapping onto the pellet, shown as contour plots.

(a) Maximum-minimum (peak-to-valley) intensity nonuniformity versus spot radius (a, normalized by the initial pellet radius r_0 = 0.363 cm) and spread (tilt-offset distance, δa, normalized by the spot radius a). Contours are plotted as 0.5% intervals.

(b) Total energy absorption for the same parameter space as (a); contours are at 5% intervals.

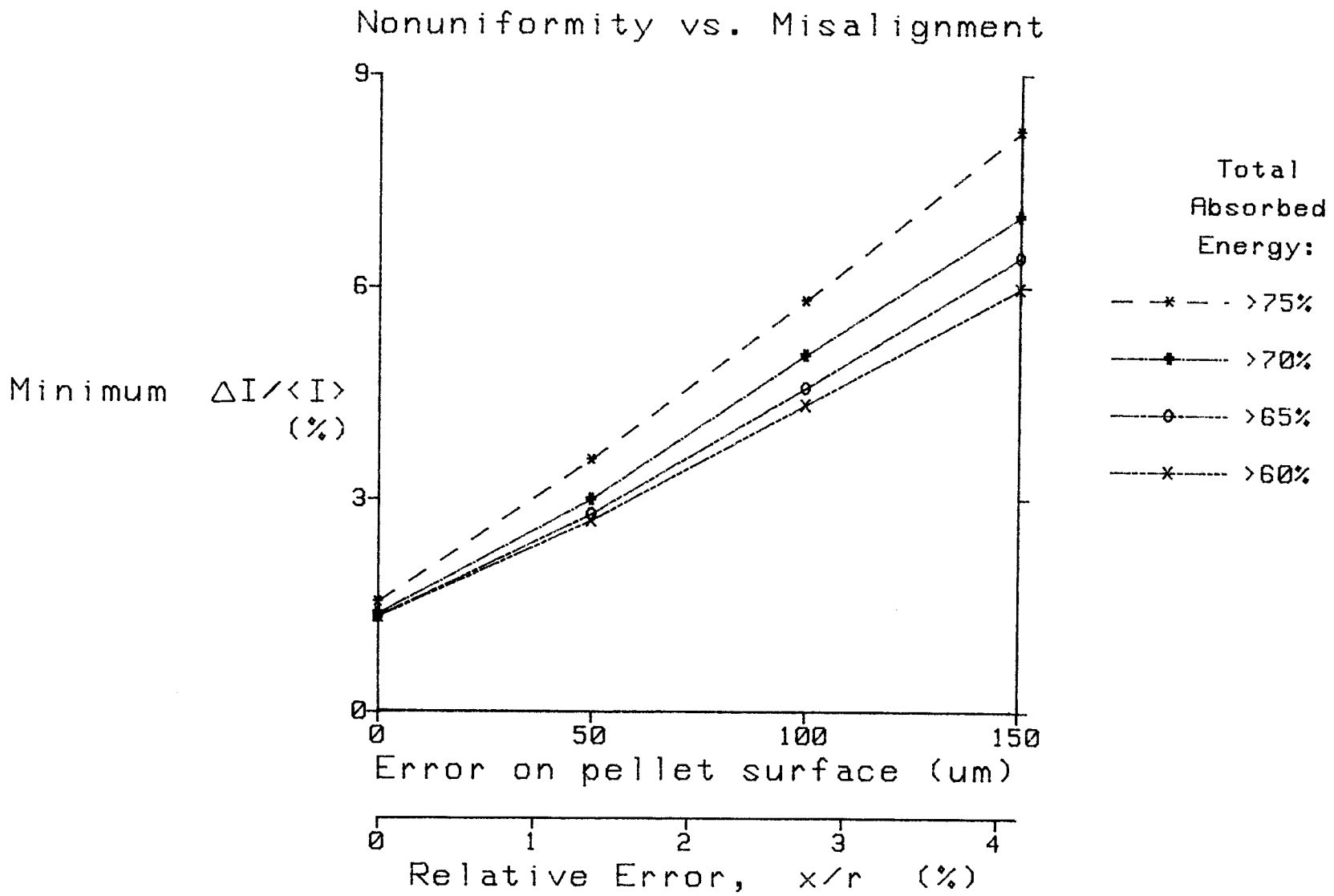

Fig. IV.2.4. Minimum nonuniformity versus misalignment error, under the constraint that the total laser energy absorbed is greater than a certain amount -- (*) 75%; (#) 70%; (0) 65%; and (X) 60%.

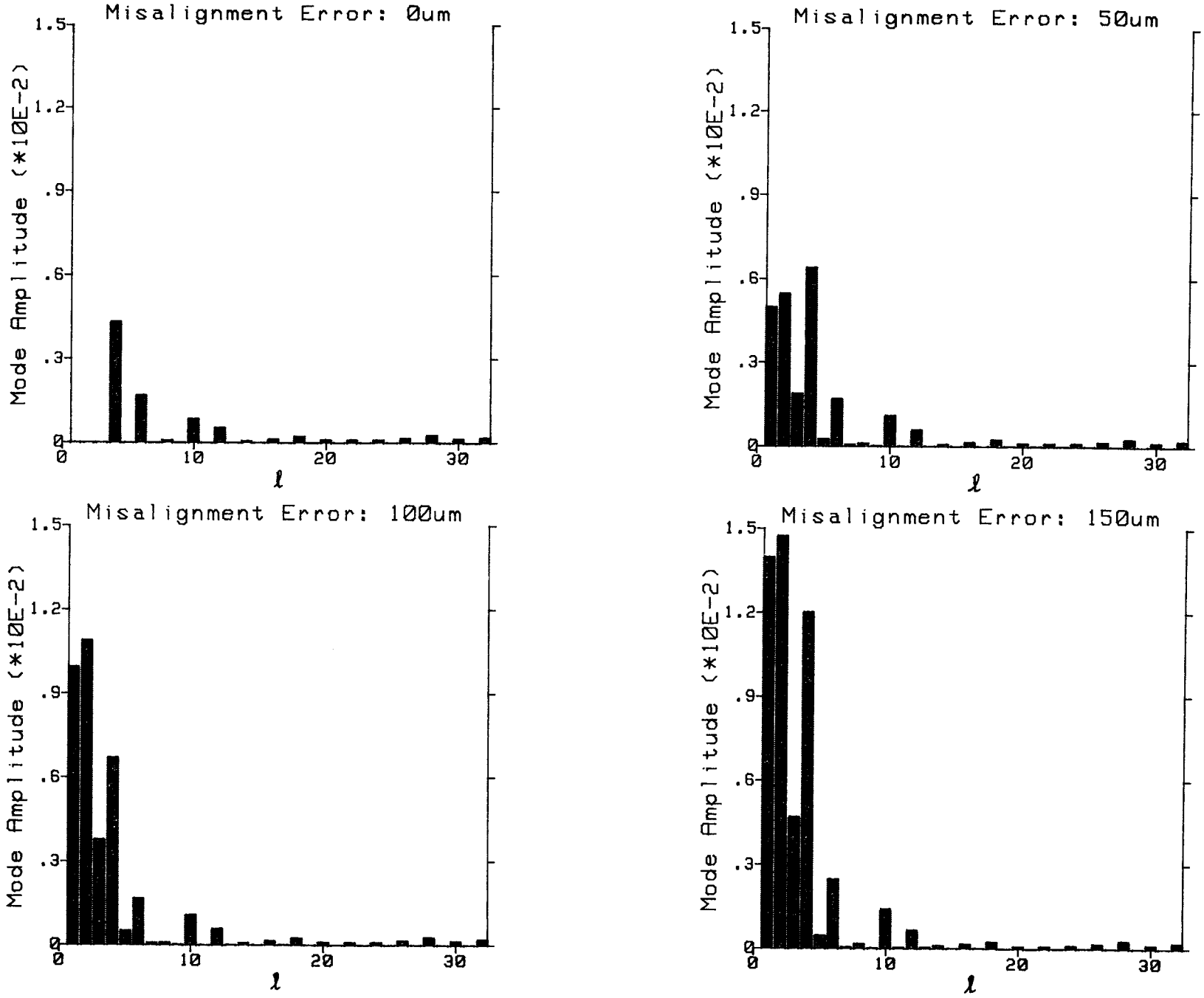

Fig. IV.2.5. Coefficients of the harmonic expansion of the illumination distribution versus mode number, ℓ. The largest coefficient (of all possible values) is plotted.

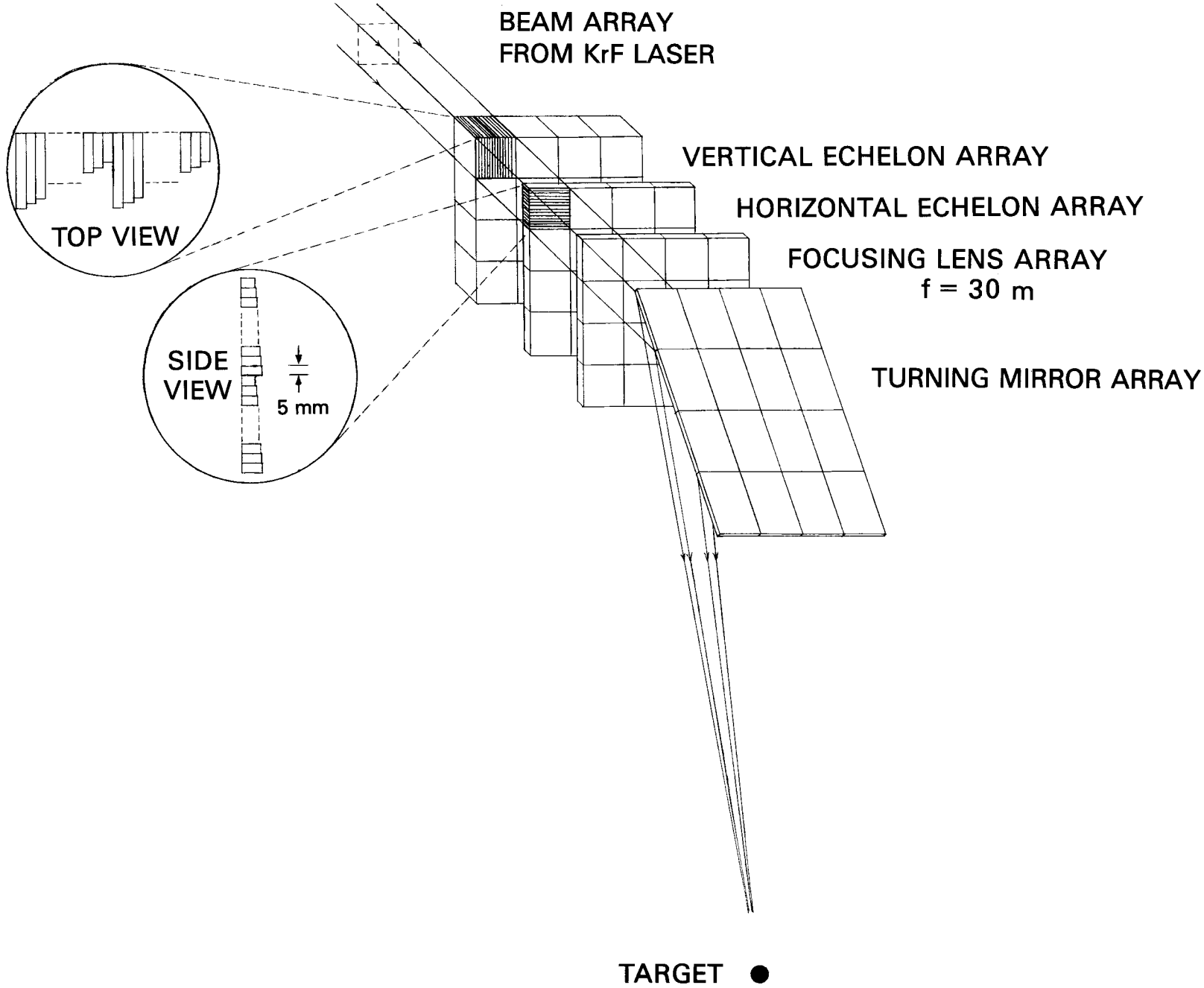

Fig. IV.2.6. Focusing system for incorporating induced spatial incoherence into the driver beams of the SIRIUS-M reactor.

I.S.I. WITH BROADBAND LIGHT

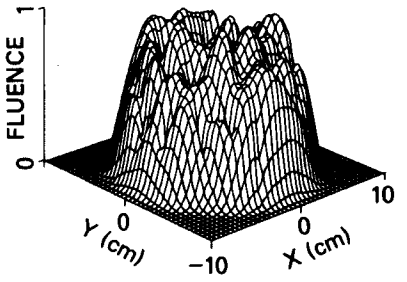

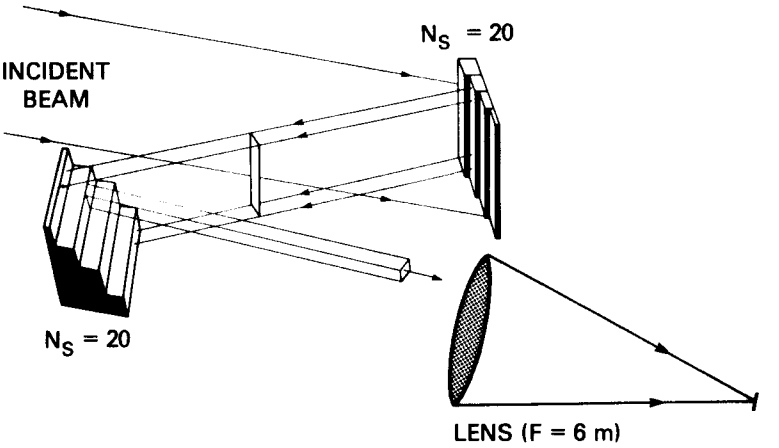

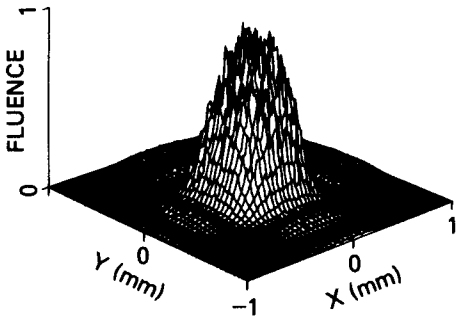

FOCAL POINT FLUENCE WITH THE ECHELONS IN PLACE, AND A BROADBAND LASER INTEGRATED OVER TIME INTERVAL $T = 100\ t_c$.

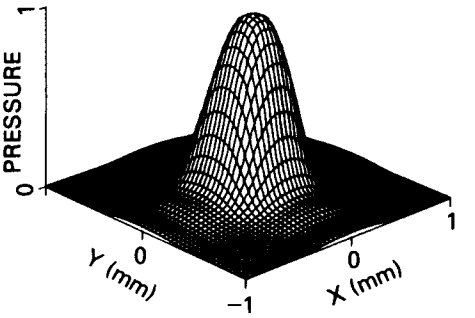

ABLATION PRESSURE, ASSUMING THERMAL SMOOTHING WITH $\Delta R = 50\ \mu m$. THE PEAK-TO-VALLEY DEVIATION FROM <P> IS 2.4%.

Fig. IV.2.7. Numerical simulations of ISI with broadband 1/2 μm light: (a) incident laser beam; aberrated to 5 × diffraction limit; (b) echelon/focusing configuration with 20 steps/echelon; (c) fluence at the focal plane (assumed to coincide with the plasma absorption region), integrated over 100 coherence times; (d) ablation pressure, assuming thermal smoothing with a 50 μm absorption-ablation distance. The statistical deviation from ensemble-averaged pressure is 2.4% peak-valley.

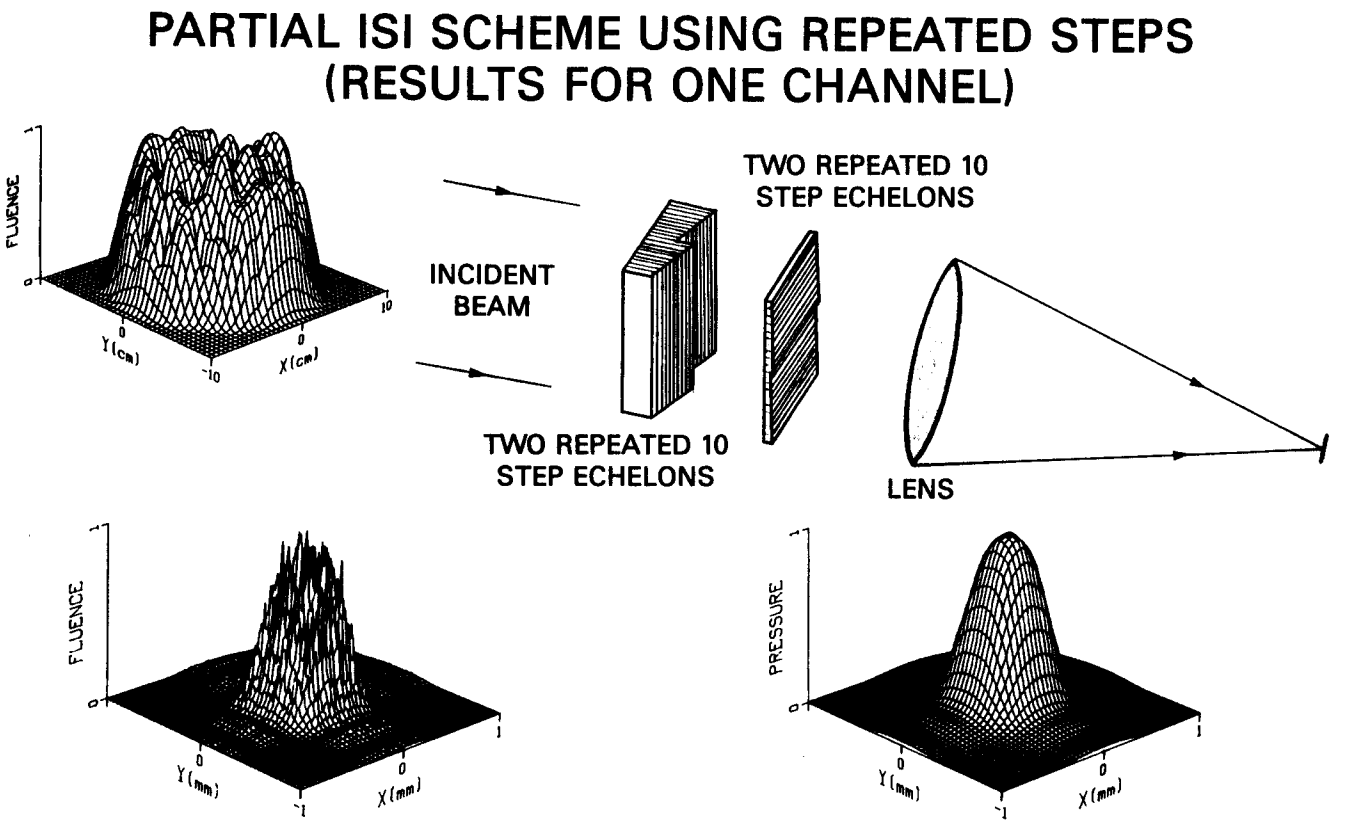

Fig. IV.2.8. Numerical simulations of the partial ISI concept with broadband 1/2 μm light: (a) incident laser beam, aberrated to a 5 × diffraction limit; (b) echelon/focusing configuration with 20 steps/echelon in two step segments; (c) fluence at the focal plane (plasma absorption region), integrated over 100 coherence times; (d) ablation pressure, assuming thermal smoothing with a 50 μm absorption-ablation distance. The statistical deviation from ensemble-averaged pressure is 3.9%.

IV.3 Support of the Final Mirrors

The beam transport system for SIRIUS-M has not yet been defined. It has been established that the final mirrors will be on the order of 1 m in diameter and located at a radius of 10 m from the center of the cavity. This is consistent with a laser power of 1 MJ, and a light intensity of 5 J/cm^2 on 32 mirrors. The direction from which each mirror will be receiving the laser beam has not yet established.

The support of the final mirrors has been thought of only in very general terms. It is generally agreed that isolating the cavity from the final mirror supports is desirable but not essential. If the vacuum boundary for the reactor cavity can be made behind the final mirrors, then it is possible to isolate the two structures. As shown in Fig. IV.3.1 the mirrors will then simply focus the laser light through the holes in the cavity and there would be no need for beam tubes connecting the cavity to the final mirrors. If on the other hand, the location of the vacuum boundary has to be at the reflector as shown in Fig. IV.3.2, then the problem becomes more difficult. One can imagine flexible vacuum tight joints in the beam tubes which could provide some, but not complete, isolation. The degree of isolation would then determine the acceptability of such a scheme.

The final mirrors will be located on a sphere of 10 m radius from the cavity center and will be separated about 6 m center to center from each other. It is possible to envisage a gridwork of trusses and beams assembled in a spherical configuration for supporting the final mirrors rigidly enough for this purpose. Tension cables may be needed for providing more rigidity while minimizing structure. Fortunately, there are no extraneous forces such as varying magnetic fields, eddy currents or MHD effects which could create

disturbances. However, until a layout of the beam transport system from the laser is available, the exact configuration of the support structure for the final mirrors will remain unresolved.

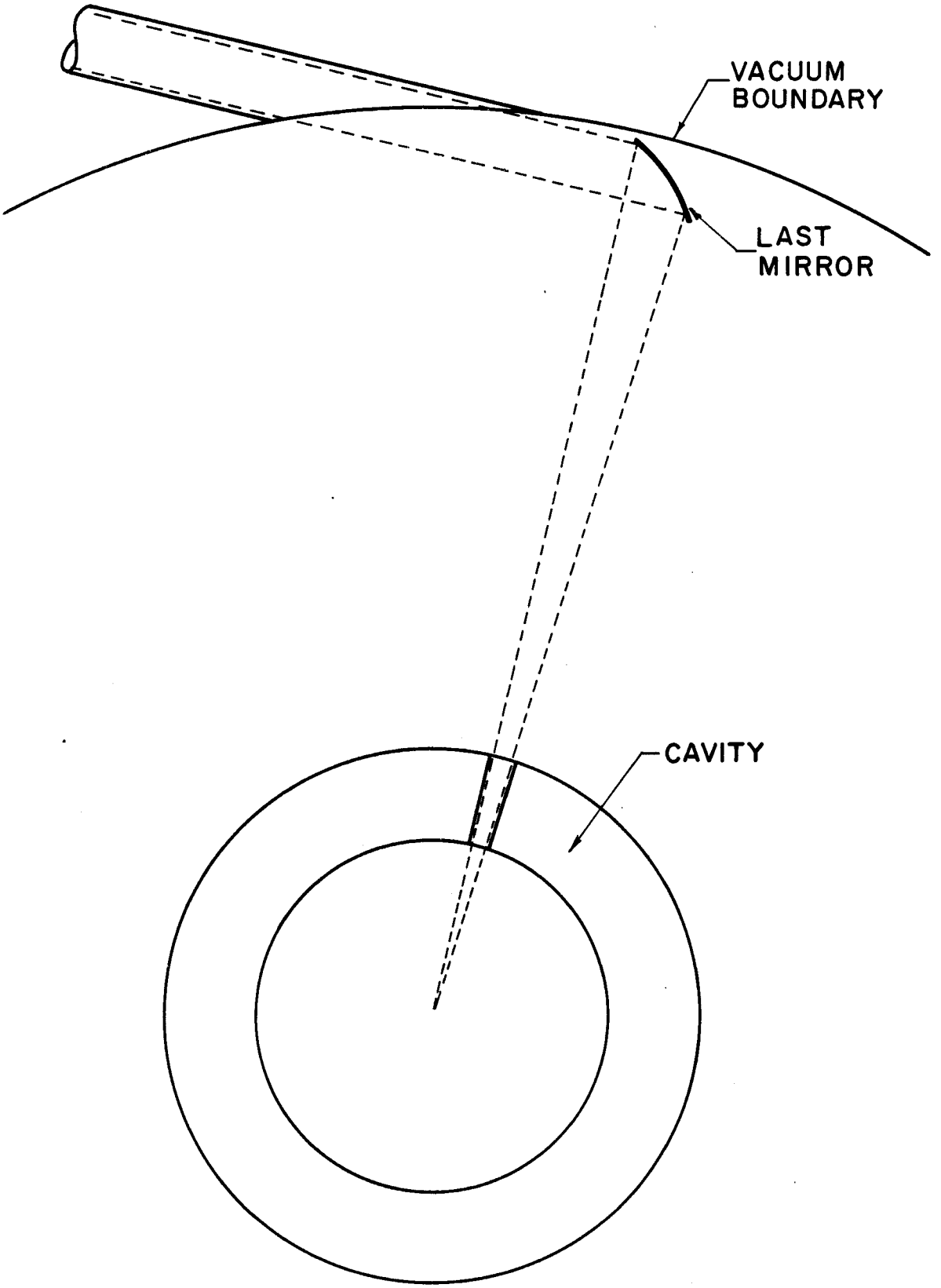

Fig. IV.3.1. Vacuum boundary behind last mirrors. Cavity decoupled from last mirrors' support.

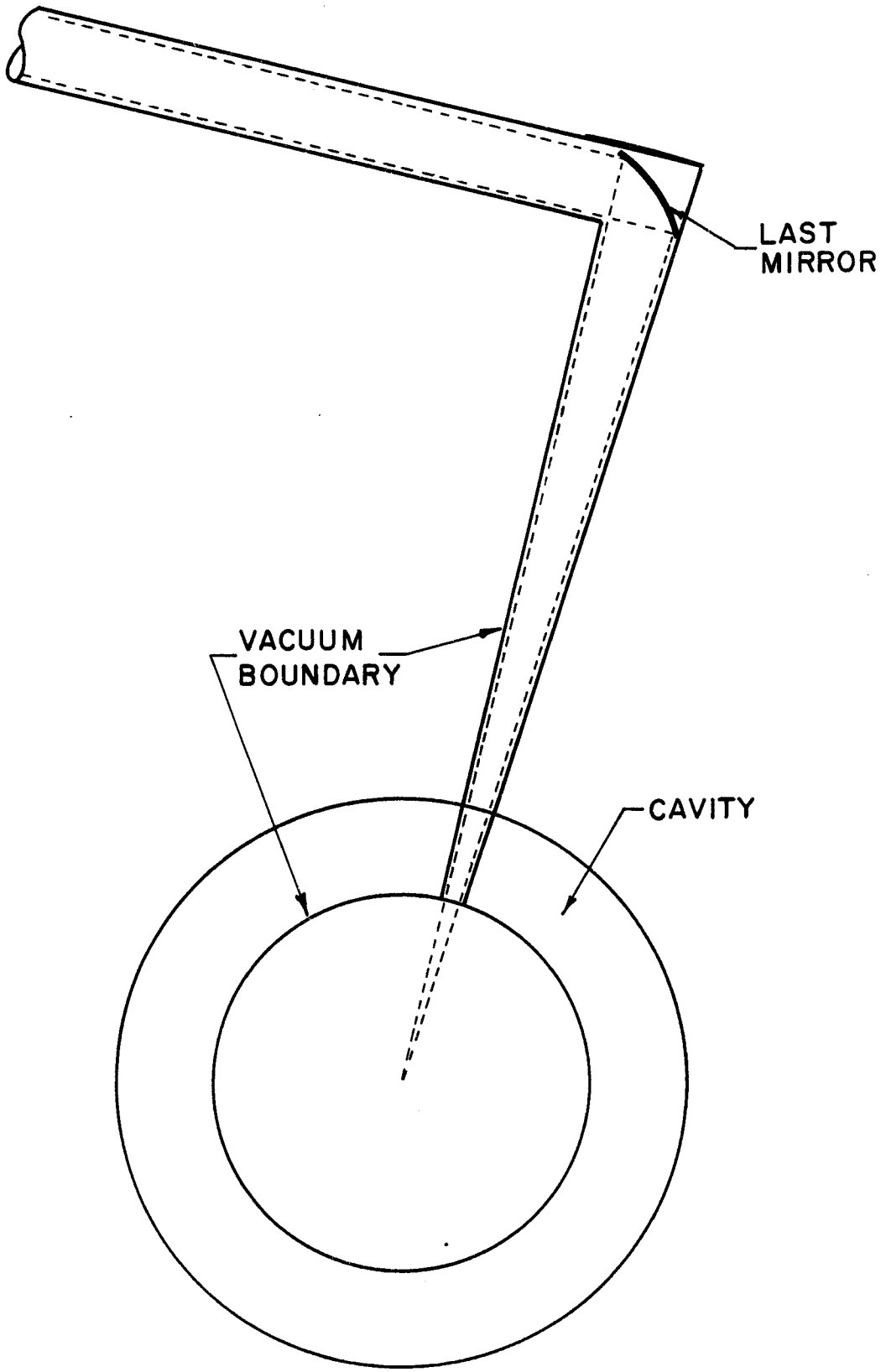

Fig. IV.3.2. Vacuum boundary at reflector and beam tubes. Cavity not decoupled from last mirrors' support.

References for Chapter IV

1. J.E. Howard, Appl. Opt. 16, 2764 (1977).

2. S. Skupsky and K. Lee, J. Appl. Phys. 54, 3662 (1983).

3. A.J. Schmitt, Appl. Phys. Lett. 44, 399 (1984).

4. University of Rochester Laboratory for Laser Energetics Annual Report (1 October 1983 - 30 September 1984), ed. by R.L. McCrory, M.C. Richardson, et al.; Digest of the 1985 Conference on Lasers and Electro-Optics (Baltimore, MD, 21-24 May 1985) paper THS1.

5. R.H. Lehmberg and S.P. Obenschain, Opt. Commun. 46, 27 (1983).

6. J.H. Gardner and S.E. Bodner, Phys. Rev. Lett. 47, 1137 (1981).

7. A.J. Schmitt, J.H. Gardner, S.E. Bodner, Bull. Amer. Phys. Soc. 30, 1363 (1985).

8. D. Milam, W.H. Lowdermilk, F. Rainer, J.E. Swain, and R.W. Hopper, Lawrence Livermore National Laboratory, 1982 Laser Program Annual Report UCRL-50021-82 (August 1983), pp. 7-30.

9. R.H. Lehmberg, S.P. Obenschain and A.J. Schmitt, Bull. Amer. Phys. Soc. 29, 1184 (1984).

10. S.E. Bodner, J. Fusion Energy 1, 221 (1981).

11. Y. Kato, K. Mima, N. Miyanaga, S. Arinaga, Y. Kitagawa, N. Nakatsuka and C. Yamanaka, Phys. Rev. Lett. 53, 1057 (1984).

V. CONCLUSIONS AND RECOMMENDATIONS

The conclusions and recommendations of the SIRIUS-M study are the following:

1. Inertial confinement fusion offers the opportunity to build a low power, non-tritium breeding, high performance materials test facility. This might include a 1 MJ short wavelength laser, low gain targets (~ 10), large materials test volume, low damage gradient within the test volume, a small fusion reaction cavity, and efficient geometry for neutron multiplication.
2. The crucial issues that must be faced for the materials test facility are a rep rateable short wavelength laser, survivable optics consistent with uniform illumination, uniformity of target irradiance, laser beam focusing through 1 torr of gas, optics positioning, stability, and layout, and reflected laser light heating of the first wall.
3. It is recommended that those issues amenable to experimental investigation, such as optics damage and laser focusing in the presence of a gas, be supported. This will greatly improve the level of understanding of supporting technology for inertial confinement fusion.